UNIVERSITY OF THE
WITWATERSRAND,
JOHANNESBURG

The synthesis, characterisation and photocatalytic activity of TiO_2/cellulose nanocomposites

Name: Muhammed As'ad Ballim

Student no: 0708602k

School: Chemistry

Degree: MSc

Supervisor: Dr Zikhona Tetana

Co-supervisor: Dr Cebisa Linganiso

Co-supervisor: Prof Nosipho Moloto

2019

DECLARATION

I declare that "The synthesis, characterisation and photocatalytic activity of TiO_2/cellulose nanocomposites" is my own, unaided work under the supervision of Dr Zikhona Tetana, Dr Cebisa Linganiso and Prof Nosipho Moloto. It is being submitted for the degree of Master of Science in the University of the Witwatersrand, Johannesburg. It has not been submitted for any degree or examination in any other university, and all sources I have used or quoted have been indicated and acknowledged by means of complete references.

Name: Muhammed As'ad Ballim

Signature of candidate

25 of June 2020

DEDICATION

BISMILLAHIRRAHMANIRRAHEEM

TO MY PARENTS AND BROTHER

ACKNOWLEDGEMENTS

- I would like to thank my supervisors for their patience, understanding and guidance throughout this project.
- I am grateful to the team at the microscopy and microanalysis unit for their help and words of encouragement and guidance.
- I am grateful to the school of chemistry for being helpful, friendly and available for assistance.
- I would have not been able to achieve my goal if not for the love and support of my family, friends and colleagues. My parents' prayers and words of encouragement helped me through a great deal.
- I thank the CATMAT group for providing a fun environment, specifically, the LAB330B for always bringing hope to the hopeful.
- The financial support of DST/NRF is greatly appreciated and acknowledged.

ABSTRACT

In this dissertation, the extraction and characterisation of cellulose fibres from a low-cost maize tassel agricultural waste material was carried out. This was achieved by base treatment of maize tassel using an alkaline treatment approach to produce cellulose I or II, depending on the treatment time, concentration and pre-treatment conditions. The polymer was characterised using XRD, TEM, SEM, Raman spectroscopy, FTIR and EDX. The results obtained showed that cellulose II was the main product and that cellulose fibres could be extracted from the waste maize tassel. Titania was synthesised by a sol-gel method using an alcohol solvent. The nanomaterial produced was then characterised using XRD, Raman spectroscopy, EDX, FTIR, TEM and SEM. It was found that the phase of the titania was anatase and the morphology was spherical. The product formed highly agglomerated structures that also took the form of spherical shapes. These also confirmed the chemical properties of titania. The size of the particles was confirmed by the Scherrer equation and analysis of SEM and TEM images by image J software and was found to be between 8 and 12 nm. The formation of TiO_2/cellulose nanocomposites was achieved by a method similar to urea deposition. The two products were meshed together and analysed by SEM, TEM, EDX, FTIR, XRD and Raman spectroscopy. It was found that the titania nanoparticles were attached to the cellulose polymer surface and the cellulose surface coverage increased with an increase in the amount of TiO_2 used. The composite was then used to treat water contaminated with the organic dye methyl orange. The results obtained from this study indicated that the TiO_2/cellulose composite could degrade the MO dye with a lesser concentration of titania attached to the cellulose when compared to bare TiO_2. Increasing the concentration of titania on cellulose proved better at degrading the methyl orange dye.

LIST OF PRESENTATIONS

1. PowerPoint paper presentation entitled, “Extraction of cellulose from rice husks.” CATMAT group presentation, 2016.
2. PowerPoint presentation entitled, “Extraction of cellulose for use in biosensors.” CATMAT group presentation, 2016.
3. PowerPoint paper presentation entitled, “Extraction of cellulose from rice husks for use in biosensors.” CATMAT group presentation, 2017.
4. PowerPoint presentation entitled, “Cellulose-TiO_2 composite in the degradation of organic dye.” CATMAT group presentation, 2017.
5. Poster presentation entitled, “Cellulose extraction from maize tassel,” at the Microscopy Society of Southern Africa conference held at Aventura resorts, Bela-Bela, December 2017.

Contents

LIST OF FIGURES

LIST OF TABLES

LIST OF ABBREVIATIONS

Ce	:	Cellulose
CT	:	TiO_2/Cellulose composite
dH_2O	:	Distilled water
FTIR	:	Fourier transform infrared spectroscopy
MT	:	Maize tassel
MO	:	Methyl Orange
SEM	:	Scanning electron microscope
T	:	TiO_2
TEM	:	Transmission electron microscope
TGA	:	Thermogravimetric analysis
UV-Vis:		UV-Visible spectroscopy
XRD	:	X-ray diffraction spectroscopy

OUTLINE OF THE DISSERTATION

CHAPTER 1: Introduction and rationale behind the study

CHAPTER 2: Literature review

CHAPTER 3: Methodology

CHAPTER 4: Synthesis and characterisation of cellulose from maize tassel

CHAPTER 5: The synthesis of anatase TiO_2 by sol-gel

CHAPTER 6: Titania/cellulose composites: preparation and characterisation

CHAPTER 7: The photocatalytic investigation into the degradation of methyl orange organic dye in wastewater

CHAPTER 8: Conclusions and recommendations

CHAPTER 1

General Background

1.1. Introduction

South Africa is currently overexploiting its water resources [1]. The water infrastructure is damaged, and the dam levels are extremely low [1]. This makes South Africa a water scarce country with more than 60% of its rivers being over exploited. There is also a decline in precipitation levels in most part of the country whilst the temperatures are rising thereby increasing the risk of drought. Environmental pollution exacerbates the availability of clean water. Environmental pollution is always increasing, and the preservation of water sources is becoming more difficult. Waste emanating from manufacturing is one of the key contributors to water pollution. Pollution from textile industries in wastewater adds to almost 400 tons of dyes and chemicals that are released to the environment [2]. Most synthetic dyes are difficult to treat by the current conventional methods due to non-biodegradable compounds that are present in them. Textile dyes and other industrial dyes are the largest group of organic compounds that are a cause for concern. Approximately 20% of the dye is lost during the dyeing process and is released in the effluent [3]. Almost all textile dyes are photocatalytically stable as well as refractory toward chemical oxidation making the dyes resistant to decolorization by conventional biochemical and physiochemical methods [1-5]. Untreated colored wastewater released from these industries creates non-aesthetic pollution and eutrophication and create byproducts through oxidation, hydrolysis or other chemical reactions in the water [6]. The dyes may also have toxic effects and increase turbidity in the water, thereby reducing light penetration in these water bodies thereby annihilating aquatic life [5].

Several techniques have been employed for the reduction of toxic dye effluents from wastewater. These methods include photocatalysis [7], coagulation [8], flocculation [9], and reverse osmosis [10], adsorption on activated carbon [11], ion exchange ultra-filtration [12], as well as chemical methods such as photosensitized oxidation [13]. These methods have proven effective in water treatment; however, the main drawback is the formation of secondary waste products that cannot again be treated [14, 15]. Photocatalysis is an oxidation process used in the photodegradation of compounds and the purification of water [14, 15]. Photocatalysis is

divided into Heterogeneous catalysis and Homogeneous catalysis and has many advantages over traditional wastewater treatment techniques [14]. For example, chemical oxidation cannot remove all organic substances however it is suitable for high concentration pollutants. On the other hand, activated carbon adsorption involves the phase transfer of pollutants without decomposition [14], while biological treatments are slow and require strict parameters. Hence photocatalysis is advantageous due to these constraints from other methods and can remove pollutants even at low concentrations. Photo-oxidation by photocatalysis oxidizes organic pollutants completely within hours and does not form secondary pollutants [14, 15].

1.2. Problem statement

Titanium dioxide (TiO_2) is widely used because of its high oxidation efficiency, non-toxic nature, high photo-stability, chemical inertness and is safe for the environment [14, 15]. TiO_2 has a wide bandgap of ~3.2 eV and mineralizes a wide range of organic pollutants, e.g. pesticides, phenolic compounds, tetracycline, etc., under UV radiation. The factors that influence the photocatalytic degradation include dye concentration, catalyst concentration, pH, the size and structure of the photocatalyst, the surface area and reaction temperature [14, 15]. A problem with the use of TiO_2 as a photocatalyst is its low photo-quantum efficiency caused by the fast recombination of electron and hole [14, 15]. TiO_2 is also inactive in visible light due to the wide bandgap (~3.18 eV for anatase). In addition, in a powder form, recovery of the catalyst is difficult. The dispersed powder may also increase solution's turbidity, increasing the difficulty for UV radiation penetration. These challenges therefore render the use of powdered TiO_2 less efficient in photocatalysis.

1.3. Rationale for the study

Herein we sort to remedy the challenges. The in-situ synthesis of TiO_2 nanoparticles on a support material such as cellulose to form a composite will be explored. Anatase TiO_2 is the preferred polymorph of TiO_2 due to a higher electron mobility, low dielectric constant and low density [16]. The superfine structure of cellulose makes it an ideal support for photocatalysts. The cellulose membrane allows for the collection and removal of nanoparticle photocatalyst suspension in water after photocatalytic treatment. The optical properties of cellulose enhance the electron distribution and transfer to TiO_2 on the surface, thereby increasing the photocatalytic activity of TiO_2 by minimizing recombination [17]. On the other hand, the use

of anatase TiO_2 improves the stability, hydrophilicity and anti-fouling as well as permeability properties of the cellulose membrane [18, 19].

1.4. Aims and objectives

The aims of this project were therefore the following

- To synthesize anatase TiO_2 nanocrystals
- To extract and purify cellulose from maize tassels
- To prepare TiO_2/cellulose composites
- To evaluate the photocatalytic degradation of methyl orange using the TiO_2/cellulose composites

The objectives of the project were:

- To characterize the cellulose
- To characterize the anatase TiO_2 nanocrystals
- To prepare and characterize TiO_2/cellulose composites
- To characterize TiO_2/cellulose composites
- To determine the best TiO_2/cellulose composite for methyl orange dye degradation

1.5. References

1. Donnenfeld Z., Crookes C., Hedden S., Southern Africa Report, 2018, 13, 2-6.
2. Kumar A., Pandey G., Material Sci. & Eng. Int. J., 2017, 1, 106-14.
3. Zollinger H., VCH-Wiley, New York, 1991, 2, 92-102.
4. United Nations (UN), The United Nations World Water Development Report 3: Water in a changing world, 2009, http://unesdoc.unesco.org/images/0018/001819/181993e.pdf
5. Ibid. C Vörösmarty., Nature, 467, 7315, 2010. Microbials refer to ‘a unicellular or small multicellular organism including bacteria, protozoa, some algae, fungi, viruses and some worms, especially those that are injurious to other organisms, Microbial, http://medical-dictionary. thefreedictionary.com/microbial.
6. Prado A. G. S., Bolzon L. B., Pedroso C. P., Moura A. O., Costa L. L., Appl. Catal. B.: Environ. 2008, 82, 219-224.
7. Tang W. Z., An H., Chemosphere, 1995, 31, 4158-70.
8. Yeheyes K., Zewge F., Chandravanshi B. S., Ethiop. J. Sci., 2006, 29, 133-40.
9. Wang S., kong F., Fatehi P., Hou Q., Molecules, 2018, 23, 1-15.
10. Abid M. F., Zablouk M. A., Abid-Alameer A. M., Iran. J. Environ. Healt., 2012, 9, 1-9.

11. Malik P. K., J. Haz. Mat., 2004, 113, 81-8.
12. Lafi R., Gzara L., Lajimi R. H., Hafiane A., Chem Eng. Process., 2018, 132, 105-13.
13. Wu T., Liu G., Zhao J., Hidaka H., Serpone N., J. Phys. Chem. B., 1998, 102, 5845-51.
14. Akpan U. G., Hameed B. H., Journal of hazardous materials, 2009, 170, 520-29.
15. Khatae A.R., Kasiri M. B., Journal of molecular catalysis A: chemical, 2010, 328, 8-26.
16. Trabelsi H., Khadhraoui M., Hentati O., Ksibi M., Toxicological and environmental chemistry, 2013, 543-58.
17. Bai J., Zhou B., Chem. Rev. 2014, 114, 10131-76.
18. Park S., O Baker J., Himmel E. M., Parilla P. A., Johnson D. K., Biotechnology for Fuels, 2010, 3, 2-10.
19. Mohamed M. A., Mutalib M. A., Hir Z. A. M., Zain M. F. M., Mohamad A. B., Minggu L. J., Awang N. A., Salleh W. N. W., Int. J. Bio. Mol., 2017, 103, 1232-56.

CHAPTER 2

Literature review

2.1. Introduction

Synthetic dyes are used in many applications which results in polluted wastewaters escaping to natural water environments. These wastewaters are difficult to treat due to the non-biodegradable compounds found in the dyes. There are various methods that have been developed to treat the wastewater, but each involves a high cost or creates toxic secondary pollutants. Recently however, the use of hybrid materials is of interest, particularly the most popularly studied TiO_2 and now cellulose as a substrate. The cellulose fibres allow the TiO_2 to have an increased surface area for catalysis and reduce the effort involved in recovering the catalyst. In this particular study, the cellulose obtained from maize tassel has been used in the formation of hybrid nanomaterial and photocatalytic degradation of methyl orange, an azo dye that is commonly used.

2.2. Background of cellulose

It is estimated that 10^{11}-10^{12} tons of cellulose is produced every year [1]. The cellulose polymer is used as a construction material or as a versatile starting material for chemical conversions, e.g. in creating artificial, cellulose based threads and films and other cellulose based derivatives. Cellulose nitrates have been used by the military as cellulose nitrate, which combined with camphor, creates “plastic” or celluloid [2]. According to polymer-analogue reactions, functional groups of macromolecules, hydroxyl groups with cellulose can undergo similar reactions to the corresponding low-molecular compounds [1]. Cellulose naturally occurs in the lignocellulosic material of forests, wood being the most abundant source. Other cellulosic containing material includes agricultural residues, water plants, grasses and other plant material. Aside from cellulose, these lignocellulosic materials also contain hemicellulose, pectin, lignin and a small number of extractives [3]. Since cellulose is naturally occurring, it may contain by-products that may lead to difficulty in chemical modification reaction, however high purity material has been previously produced [1]. The degree of polymerisation of cellulose (DP) (molecular weight = DP * 162 $g.mol^{-1}$) show the difference in molecular weight available [1].

Cellulose is a polydisperse linear homopolymer that consists of regio- and enantioselective β-1,4-glycosidic linked to D-glucopyranose units, also called anhydroglucose units (Figure 2.1). The β-D-glucopyranose has been shown by nuclear magnetic resonance (NMR) to adopt a $^4C_1$ chain conformation which is the lowest free energy conformation of the cellulose molecule [4]. The hydroxyl groups are positioned in the ring plane (equatorial) while the hydrogen atoms are positioned in the vertical axis (axial) [5]. The cellulose polymer contains free hydroxyl groups at the C-2, C-3 and C-6 atoms. Many types of supramolecular semi-crystalline structures are formed due to the hydroxyl group and oxygen atoms of the pyranose ring and the glycosidic bond [5]. Cellobiose is the repeating unit of cellulose [6].

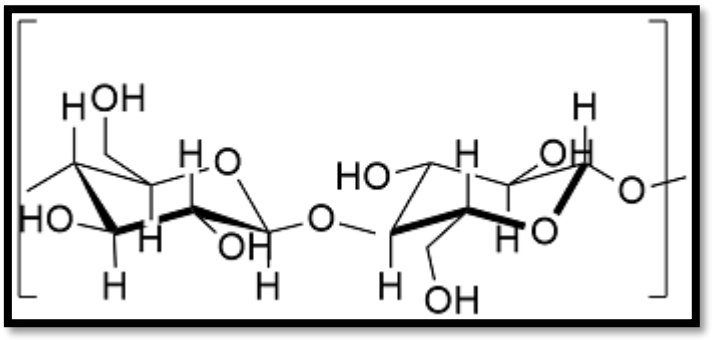

Figure 2.1: Chemical structure of cellulose [7].

Biomass refers to the organic material such as wood, grass, algae and other residues including some animal waste [8]. Materials that are rich in cellulose, hemicellulose and lignin are referred to as lignocellulosic biomass. This biomass has gained interest for its many uses in renewable energy and material. Agricultural waste contains high amounts of oxygen and easily releases volatile materials in a combustor [9]. Because these agricultural wastes are a source of pollution, methods of eradication are constantly being sought. Cellulose is a renewable raw material, with the linear polymer, β-D-glucose as the main component. The use of maize tassel as a source of biomaterial to produce cellulose bio composites has not been thoroughly explored, giving the advantage of early discovery [10].

Maize is a staple food in many countries and an important resource for waste material. This is an ideal material because of low cost and availability. The maize tassel is the male flower of the maize plant (Figure 2.2). The tassels have different colours. The tassel which grows at the apex of the maize stalk is discarded after the maize crop has been harvested. Because it is fibrous in nature, and high in carbohydrates, it is assumed to contain large quantities of

polysaccharides with the cellulosic surface containing hydroxyl groups and residual aromatic compounds which give the scent during the vegetative period. The hydroxyl, carbonyl, conjugated bonds, and amine functional groups on the surface may provide a possible binding site for metal cations and oxo anions [10].

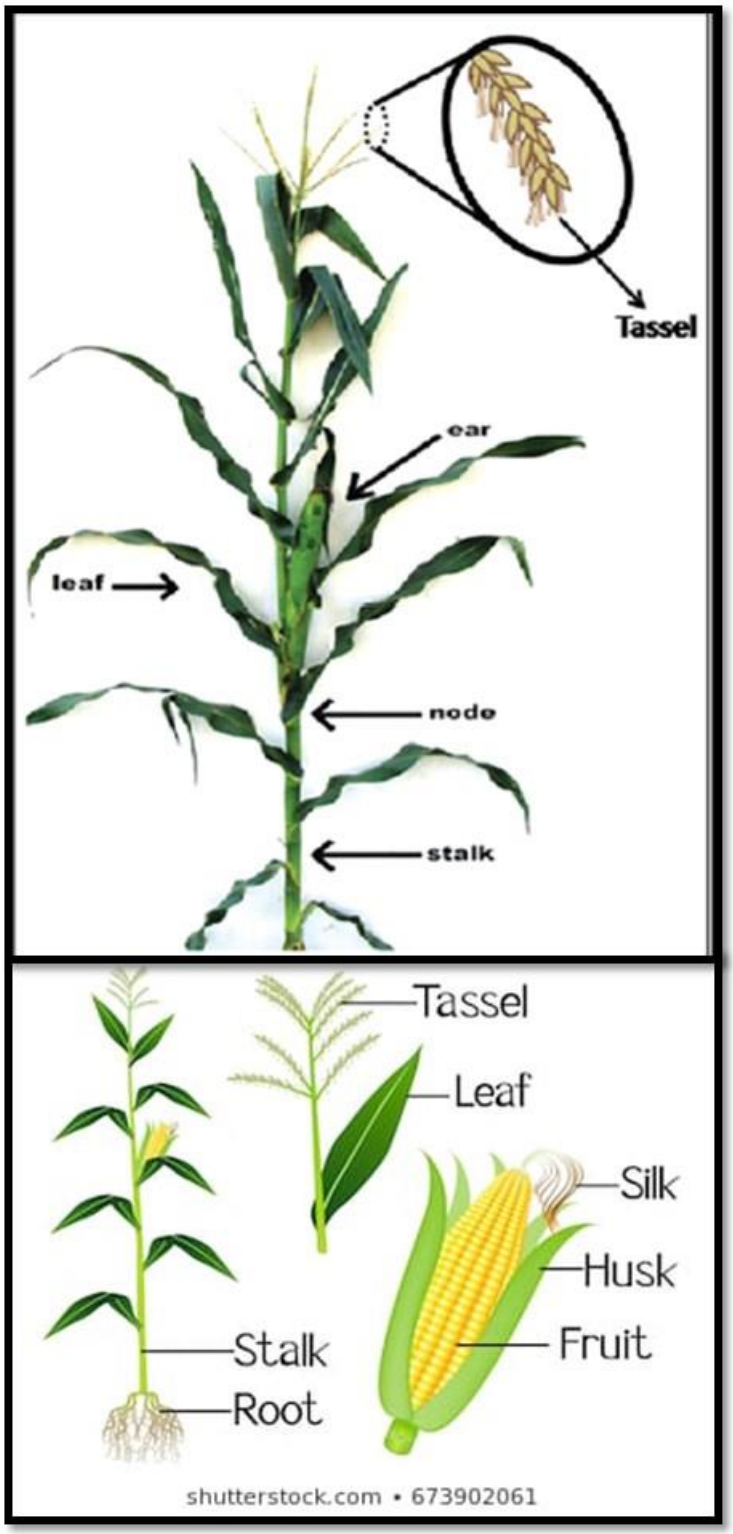

Figure 2.2: Depiction of maize plant with tassel at the top [10, 11].

Cellulose is composed of glucose molecules and is the primary structural material of plant cell walls [12]. Figure 2.3 is a representation of each component in the cell wall of plants. Cellulose microfibrils are embedded in a carbohydrate matrix. The primary and secondary cell walls that contain cellulose microfibrils are bound together to create macrofibrils. These macrofibrils are made of a core of glucose residues that are made of cellulose molecules enclosed in hemicelluloses and pectin [12]. These microfibrils are oval to circular and vary from 5-35 nm in diameter [12]. Most plant microfibrils average around 10 nm diameter [1,12]. The microfibrils comprise groups of cellulose molecules that are arranged in a crystalline lattice called a micelle. These together form what is called a crystallite. The basic plant cell wall is made up of the microfibril, the central crystalline cellulose core which contain micellar strands [12]. These cellulose microfibrils are separated by interfibrillar capillaries containing a matrix comprising a variety of compounds, including: hemicelluloses: a polysaccharide more soluble and less ordered than cellulose, lignin: a polymer of high carbon content, pectin, suberin, cutin, simple sugars, proteins containing amino acids, proline, hydroxyproline and water [1,13]. The molecules of hemicelluloses and pectin residues are linked to the cellulose molecules. The relationship between the cellulose microfibrils, hemicelluloses and other compounds was assumed to be covalent and hydrogen bonding is assumed between the polymers and the cellulose [14]. A more recent model suggests that microfibrils are held together by xyloglucan chains with the pectin and structural proteins filling the space between them [15]. The strength of this wall is due to noncovalent bonding of the xyloglucan chains to the microfibril surfaces, and some xyloglucan chains are embedded within the microfibrils [15, 16 ,17]. Yet another model suggests that the microfibrils are enclosed by a layer of tightly bound hemicelluloses such as xyloglucan enclosed by a sheath of loosely bound hemicelluloses [17]. These hemicelluloses and microfibrils are embedded in a matrix of pectin. The xyloglucan chains may be embedded in the microfibrils, which are not linked to each other, however the strength comes from non-covalent bonding between the polymers [17 ,18]. A hydrophobic domain is created between the crystalline cellulose and hemicellulose network where bonding between the molecules of cellulose and hemicellulose exclude water molecules from between the microfibrils [12].

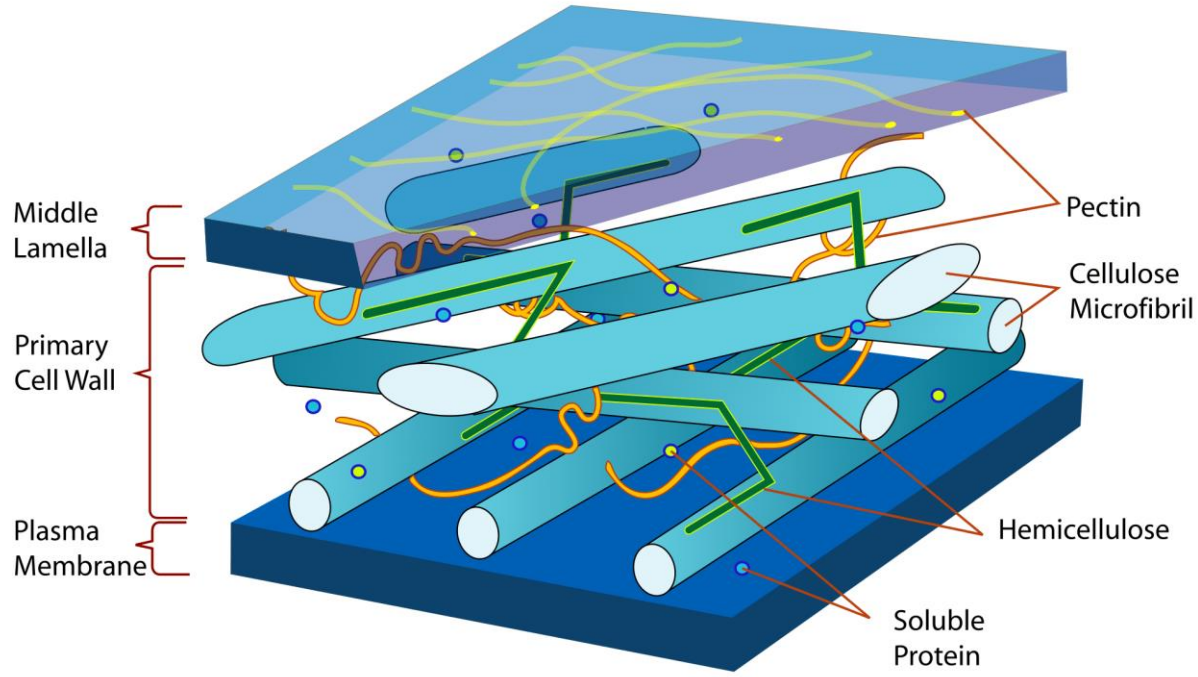

Figure 2.3: Model of cell wall structure [19].

Microfibrils are generated by terminal cellulose synthase complexes in the plasma membrane of plant cells. There are two types of microfibril generating complexes, linear complexes and rosette shaped complexes comprising a cluster of six particles and sometimes contains a centrally located globular component. [20] Since these complexes are found at the end of microfibrils, it was hypothesised that the particles they are made of are enzymes responsible for the synthesis of β-1,4-glucan from which cellulose is made [20]. These glucan chains self-associate through intra and inter chain hydrogen bonding forming insoluble, crystalline microfibrils [21]. Cellulose fibres can be used as a source of cellulose nanofibers, nanocrystalline cellulose and cellulose acetate [22]. Cellulose is fibrous and tough and forms a water insoluble polymer because of complex inter and intra molecular hydrogen bonds, it's also important in the plant structure [23]. The chemical formula of cellulose is $(C_6H_{10}O_5)n$, consisting linear polysaccharide of D-glucopyranose units connected to each other with β (1-4)-glycosidic links. A dimer of glucose known as cellobiose is the repeated unit. Each monomer of cellulose has three hydroxyl groups in positions C2, C3 and C6. These form hydrogen bonds that are either inter or intramolecular [24]. The intramolecular hydrogen bonds are between D-glucopyranose rings with the polymer chains, and intermolecular hydrogen bonds is with other polymer chains. This hydrogen bonding allows the formation dense molecular arrangements that create a 3D crystal and web like structure. Single elementary cellulose fibril accumulates on each other and aggregate microfibril cellulose chain fibres due to strong affinity of hydrogen

bonds. Cellulose chain fibres are created by the aggregation of cellulose molecules to microfibrils which form either highly ordered (crystalline) or less ordered (amorphous) regions. Individual cellulose fibres are called microfibrils, that are packed together to form cellulose fibres. These micro fibrils form bundles which then form cellulose fibres [13].

Cellulose nanofibers are usually less than 100 nm in diameter and have a length of few hundred nanometres. They are also called micro fibrillated, nanofibrils, microfibrils and nano fibrillated cellulose [13]. These cellulose nanofibers can be obtained in many ways including alkaline solution treatment, pulping, mechanical separation, acid hydrolysis and steam explosion [13]. Nanocrystalline cellulose (NCC) or cellulose nanocrystals are highly crystalline with at least one dimension that is less than 100 nm and are shaped into broad needles or rods [25]. NCC is created by acid hydrolysis of cellulose microfibrils with sulfuric acid at certain concentrations, time and temperature or from the destruction of cotton cellulose by phosphotungstic acid in acetic acid medium [26]. Hydronium ions cleave the glycosidic bonds of the amorphous regions of cellulose microfibrils to free the crystalline cellulose units. Acid hydrolysis isolates the crystal part of the cellulose chain and promotes the attachment of sulphate groups on the surface of the NCC, contributing to the stability of the cellulose suspension due to electrostatic repulsive forces between negatively charged sulphate groups on the surface. These forces prevent precipitation [27].

2.3. Different types of cellulose

i. Cellulose acetate is made using heterogeneous/homogeneous functionalisation. Heterogeneous functionalisation is acetylisation of the hydroxyl group in acetic anhydride and acetic acid with cellulose. To catalyse the reaction, either sulphuric acid or pyridine is used [28]. Transformation is not homogenised due to slow mass transfer in the cellulose slurry, leaving the cellulose in a dispersed state. Random substitution patterns, time, corrosion, cellulose degradation and side reactions may limit the reaction [29]. Synthesis of partially substituted cellulose esters is impossible [29].

ii. Bacterial cellulose is derived from bacteria and has higher purity, hydrophilicity, biocompatibility, mechanical properties and has an ultra-fine structure [30, 31]. The only downside is the high cost of the carbon source essential for bacterial growth. It does not contain hemicellulose or lignin and has a highly hydrophobic, fibrous and 3D

non-woven network. Because of this high content of cellulose, it can have a high degree of polymerisation [32].

iii. Regenerated cellulose is used in membrane production due to good chemical and solvent resistance and high hydrophilicity [33]. This type of cellulose is thermally as well as chemically stable, biocompatible and easy to make. Physical dissolution, shaping and regeneration processes produce this cellulose. Non-derivatising solvent dissolves the cellulose without using a previous chemical modification. The solvent is recyclable making this a green process. There are various solvents to carry this process out such as NaOH/urea, NaOH/thiourea, N-methyl morpholine-N-oxide (NMMO) [34].

iv. Cellulose hydrogel is a cross-linked 3D hydrophilic polymeric network, able to absorb large volumes of water and biological fluid. They are classified as physical hydrogels, chemical hydrogels and composite hydrogels [35]. Cellulose aerogel is a super critically or freeze-dried form of hydrogel. Preparation of hydrogel is a two-step process involving dissolution and gelation [36]. Solvent exchange from an ionic liquid and then methanol vapour creates biodegradable cellulose hydrogel. The surface of the hydrogel is smooth and contains no pores or fibrous structures. Cellulose hydrogel maintains shape due to rod-like stiff polymer chains that protect against changes in solvent, pH and temperature [37]. The porous aerogel is synthesised from Nano fibrillated cellulose using freeze drying method where the solvent is frozen in the gel and then sublimated to avoid forming the liquid phase [35].

Cellulose, being a chain of glucose residues, and the main component of plant cell walls, is an abundant biopolymer. The abundance, biodegradability, biocompatibility and renewability have other unique properties such as a high Youngs modulus, transparency, dimensional stability and a low thermal expansion coefficient [38]. Most of the reactions involving cellulose are heterogeneous [39]. Cellulose in a solid form is difficult to directly photodegrade because of the rigid long chains and strongly inter and intra-molecular hydrogen bonded structure of the cellulose [40]. Highly crystalline cellulose nanostructures are more stable than cellulose fibres. Thin film cellulose is reported as having a high photostability with or without a photocatalyst embedded in the cellulose matrix [41]. The photodegradation of cellulose is complicated and mineralises the cellulose compound into water and carbon dioxide. Photostability could be improved by cross-linking the cellulose with a polymer such as polyvinyl alcohol (PVA) [42].

2.3.1. Hydrogen bonding

The macromolecular order in a cellulose fibre is not uniform throughout the structure. A region of low order (amorphous) exists along with a region of high crystalline order. The fringed fibril model assumes low order (amorphous) and high order (crystalline) regions and neglects the matter with an immediate state of order [1]. The degree of crystallinity of cellulose which is commonly in the range of 40-60% depends on the origin and history (pre-treatment) of the sample [1].

2.3.2. Crystal structure of cellulose

The macromolecular order in a cellulose fibre is not uniform in the entire structure. a region of low order (Amorphous) exists as well as a region of high crystalline order. The fringed fibril model assumes low order (amorphous) and high order (crystalline) regions and neglects the matter with an immediate state of order [1]. The degree of crystallinity of cellulose which is commonly in the range of 40-60% depends on the origin and history (pre-treatment) of the sample [1].

2.3.3. Cellulose I

There are many polymorphs of cellulose that differ only in unit cell dimensions and possibly in their chain polarity. The native cellulose, cellulose I polymorph, Meyer et. al [43] proposed that the unit cell of cellulose I is monoclinic with a space group P2 and two anti-parallel cellobiose chain segments that run in opposite directions along the fibre axis [1]. Again, the unit cell of native cellulose depends on the source and method of preparation. Gardner and Blackwell [44] proposed a monoclinic lattice with two parallel chains and assumed this to be the general cellulose I structure. Sarko and Mugli [5] proposed a triclinic lattice cell with two cellulose chains running parallel along the fibre axis. Atalla and Vandehart [45] showed by high resolution NMR that native cellulose is made of two different crystal structures, Cellulose I_α and I_β. There are differences in the resonance of the C_1 atom [5]. The I_α modification is described as a triclinic P-1 structure with one cellulose chain per unit cell. The cellulose I_β is assumed to be a monoclinic cell with space group P-2 and two chains per unit cell. The Cellulose I_α phase is metastable and can be converted to the more stable I_β by annealing [1, 5].

2.3.4. Cellulose II

Cellulose II is the most important crystalline form of cellulose due to its commercial application [1]. Cellulose II is prepared via two different methods: mercerisation (alkali treatment) and regeneration (solubilisation and subsequent recrystallisation) [6]. During mercerisation, cellulose is soaked in NaOH, which is followed by washing out the NaOH. Mercerisation activates the polymer before the production of technical cellulose ether. During the regeneration process, precipitating dissolved cellulose into an aqueous medium is used to prepare cellulose II [1]. The conversion of cellulose II to cellulose III is generally thought of as being irreversible.

2.3.5. Cellulose III and IV

The crystalline modification of cellulose into cellulose III is by treatment of native cellulose with liquid ammonia or inorganic amine such as ethylene diamine followed by an alcohol wash. There exists a small difference in the lattice dimensions of the two sub modifications, cellulose III_I and cellulose III_{II} [1]. A fourth modification, cellulose IV is prepared by treatment of other modifications of cellulose under pressure, at high temperature and in a suitable liquid [1]. Most cellulosic material consists of crystalline and amorphous domains in varying proportions that depend on the source and history of the material. The physical and chemical reactivity and behaviour of the cellulose is influenced by the arrangement of cellulose molecules with each other and the fibre axis [46]. The fibres of conventional amorphous cellulose are unstable in the presence of water and moisture and usually, they form partially crystalline cellulose II. Hence, they may have a different structure from that of native cellulose fibres [46].

2.4. Chemical pre-treatment methods

Lignocellulosic biomass produces cellulosic/second-generation bioethanol in three main steps, pre-treatment, hydrolysis and fermentation [47]. The pre-treatment process involves physical processes (size reduction, boiling/steaming, ultrasonication and popping), chemical methods (acids, bases, salts, solvents) physicochemical methods (liquid hot water and ammonium fibre explosion or AFEX), biological methods (white-rot/brown-rot fungi and bacteria), and other combinations of treatment to fractionate lignocellulose into its components [48]. Pre-treatment disrupts the lignin seal and increases enzyme access to holocellulose, reduces cellulose crystallinity, increases surface area and porosity of pre-treated substrates and increases the hydrolysis rate [48]. With hydrolysis, cellulose and hemicellulose are reduced into its

component sugars by adding acids or enzymes such as cellulases. This gives the advantage of low energy consumption by the mild process, high sugar yield and no unwanted waste. Pre-treatment should avoid size reduction and costly chemicals. It should maximise formation/ recovery of sugars, preserve cellulose and hemicellulose fractions that are easy to digest using hydrolytic enzymes and produce high value lignin coproduct. Pretreatment should minimise energy consumption, yield high sugar with large biomass loads as well as avoid carbohydrate loss and formation of enzyme-inhibiting products [49]. There is no perfect pre-treatment method because of the variation in suitability of one method for various materials, which are compounded by the mode of harvest, the extent of drying, the maturity and storage conditions [49].

The alkaline treatment with NaOH is a common method and increases the digestibility of hardwood and agricultural residues with low lignin content. Sodium hydroxide ruptures the link between lignin and other carbohydrates, saponifies the intermolecular ester bond between hemicellulose and other components and causes lignocellulose to swell to remove lignin effectively. The pretreatment increases porosity and internal specific surface area of fibrous material as well as changes the structure of lignocellulose and improves the digestibility of polysaccharides by increasing the cellulose conversion rate [50]. In a previous study, Wang *et al.* used 2% NaOH at 80 °C for 2 hours which reduced the specific surface area of corn stover biomass [50].

Maepa *et al*. [12] studied the extraction of cellulose from maize tassel and found that 5 % NaOH was able to extract cellulose and remove lignin and hemicellulose within a 45-minute treatment to some extent. They found that the fiber morphology had changed, the fibers decreased in size and had improved crystallinity and the thermal stability was improved. Hasan and Saoudi [11] studied the extraction of cellulose form agricultural waste using the acid pretreatment and NaOH treatment to remove the cellulose from other components. They found that due to the large lignocellulosic content, cellulose could be extracted from the biomass waste material, i.e. rice husk, sugar can and waste office paper. The results obtained from the study indicate that cellulose may be extracted from these waste products.

“Mercerisation refers to the treatment of cotton yarn or fabrics with caustic soda solution” [51]. Mercerisation swells the cotton fibers, increasing lustre, tensile strength, dimensional stability and dye ability. It affects the fine structure, morphology, mechanical properties and reactivity.

The crystallinity and crystallite sizes decrease, while the orientation of the cellulose chain with respect to the fiber axis increases. Depending on treatment temperature, concentration as well as tension applied, the native cellulose (cellulose I) is almost completely converted to cellulose II [51]. The swelling of cellulose structure is impaired, and conversion is incomplete if tension is applied. Mercerisation may increase dye uptake and wettability in cotton [51]. The theory behind mercerization is that the hydroxyl groups on long cellulose chains attract the water molecules on the uptake of water by cellulose, the structure then expands transversely, and some mutual secondary valency links are replaced by water hydroxyl links [51]. In an alkali solution, some hydroxyl hydrogen atoms are replaced with sodium atoms, creating a high ion concentration system. By osmosis, water then enters the system and more secondary links are broken and replaced by alkali water links. Washing the alkali cellulose diffuses the sodium and hydroxyl ions away. This decreases the osmotic pressure contracting the cellulose due to elasticity. During this contraction, OH-OH links are reformed slightly, and the micelle orientation is much more random. The increase in absorptive capacity and reactivity is due to the free hydroxyl groups. A decrease in the absorptive capacity after drying is due to formation of new secondary links because of the greater amplitude of thermal vibration due to the hydroxyl groups [51].

The swelling of fibers due to mercerisation is caused by a molecular attraction with associated dehydration. Because the alkali cellulose is more hydrated than native cellulose, a maximum swelling concentration is due to the attraction of alkali cellulose and a free alkali in solution. The hydration of the cellulose increases with an increased fixation of alkali in a solution of rising concentration up to a certain limit, after which, the free alkali exerts a dehydrating effect on the alkali cellulose to a greater degree [51]. The dissociation of alkali ions from the alkali cellulose compound corresponds to absorption of OH^- ions, this creates a negative charge. The cellulose molecules then repel each other and absorb water, greater absorption implies greater charge. If the dissociation of alkali cellulose salt is forced back, a charge reduction occurs. If the concentration of electrolytes is high in the swelling liquor, then the cellulose particles charge is shielded by free ions and the repulsion force is diminished. Swelling is also due to osmotic phenomenon. The hardened cuticle around the fiber acts as a dialyzing membrane to induce osmotic action.

Mercerisation removes part of the cuticle and wax layer to change the fiber surface. This high affinity, caustic soda penetrates both the amorphous and crystalline regions. The intermolecular

forces weaken, reducing the strength of the fiber until strength is regained by deswelling and drying. The mercerization process is irreversible because of distortion of the polymer network as well as a change in the crystalline structure. These changes by mercerisation may be summarized by the following:

- increased swelling and shrinkage
- change in cellulose structure (cellulose I to II)
- decreased crystallinity
- change in orientation
- increased reactivity
- enhanced enzymatic hydrolysis
- removal of immature fibers

The change in crystal structure is explained by a change in the unit cell, the planes carrying the long chains of β-glucose residues separate. These structural changes do not occur at a particular alkali concentration, but over a range of concentrations, called a "transition range" which allows the hydrogen bonds to become disordered. An increase in alkali concentration changes the crystal lattice from cellulose I to cellulose II, which decreases the levelling off degree of polymerization. There are various intermediates that form during mercerization, these complexes form between cellulose, sodium hydroxide and water [51]. The presence of lignin in biomass reduces accessibility to cellulose microfibrils and can also hinder details in spectroscopic techniques. Biomass delignification may be achieved in many ways. The most popular lab technique for lignin removal is acid-chlorite delignification. This method uses a solution of acetic acid and sodium chlorite. Acid hydrolysis is an effective method for molecular weight reduction even under mildly acidic conditions [52, 10].

During acid hydrolysis, dried biomass is pre-soaked in water and then immersed in an acid solution for a specified period and under specific temperature. This is then filtered into liquor and unhydrolyzed solid substrate that is washed to remove sugar and acid or neutralised before saccharification [53]. In general, the hydrogen ion concentration is directly correlated with the hydrolysis reaction constant; a more negative acid pKa, makes for a more effective hydrolysis process [48]. Sulphuric and phosphoric acid are commonly used because they are cheap and efficient at hydrolysing lignocellulose [53]. Phosphoric acid has a milder effect and is more benign to the environment. HCl is more volatile, easier to recover and it attacks the biomass

better than sulphuric acid. Nitric acid has good cellulose to sugar conversion rate but both HCl and HNO_3 are more expensive than H_2SO_4 [53]. In acid, the amorphous hemicellulose in lignocellulosic biomass hydrolyse faster than cellulose to soluble sugar and some oligomer. In mild conditions this disrupts xylosidic bonds and cleaves acetyl ester groups. The lignin seal is also degraded by substitution reactions and broken links accompanied by condensation reactions prevent dissolution [54, 55]. Cellulose preferentially degrades amorphous regions which creates enlarged cellulose fibrils and fibril aggregates as well as an increase in the pre-treated materials crystallinity index. This process is affected by particle size, temperature, concentration, reaction time and liquid to solid ratio. The combined severity factor (R'o) is an index used to assess the effect of pre-treatment temperature, time and pH on the efficiency of the process [56]:

$$logR'o = \log\left(t.e^{\left(\frac{T-100}{14.75}\right)}\right) - pH \qquad \text{Equation 2.1}$$

Where t is the reaction time in minutes and T is the hydrolysis temperature in degrees Celsius. Dilute acid pre-treatment. (0.2-2.5% w/w), high temperature and pressure are used to achieve reaction times of within seconds or minutes, making it ideal for continuous operation. Low acid consumption is an advantage to cost and process severity. A variation involves two stage pre-treatments. The first stage, most hemicelluloses in the biomass are solubilised with a dilute acid, in the second stage, a stronger acid is used to hydrolyse cellulose and remaining hemicelluloses [57]. The by-products of nitric acid are difficult to remove by washing of the pre-treated substrate [58]. Mineral acids have also been found to be useful. Oxalic and malic acid have higher solution potential and degrade hemicelluloses better than sulphuric acid. They also have two pKa values that favour efficient hydrolysis over various temperature and pH values [59-61].

The main disadvantages of dilute acid treatment are the requirement of corrosion resistant reactors that are expensive [62]. The energy consumption, cost of the acids and performance limitations based on particle size and solids concentration add to the cost. Alkaline treatment is more effective at removing lignin when compared to dilute acids [63]. High acid concentrations, temperatures and treatment time increase degradation products and pseudo lignin, reducing lignin recovery in hydroxylate [64]. Concentrated acid treatment: variation of concentrated sulphuric acid (65-86% w/v) hydrochloric (41%) or phosphoric acid (85% w/w). Concentrated phosphoric acid is effective at low temperatures, dissolves cellulose in the

presence of water, has no inhibitory effects on hydrolysis and gives high sugars compared to dilute acid pre-treatment. Pre-treated biomass substrates have rough, uneven molecular surfaces [65, 66].

Alkali pre-treatment: lignocellulosic materials are mixed with bases such as sodium, potassium, calcium and ammonia at specific temperature and pressure to degrade ester and glycosidic side chains of the material causing lignin structure disruption, cellulose swelling and decrystallisation. Alkali treatment extracts hemicelluloses from polysaccharides and the organic acids that are produced lowers the pH of the solution [67, 68]. There are two main streams that are formed, a wet solid fraction comprising mainly cellulose and a liquid fraction comprising dissolved hemicellulose, lignin and unreacted inorganic chemicals [67, 68]. The process is influenced by NaOH loading, liquid to solid ratio, temperature and time. This pre-treatment is less harsh since it is carried out at atmospheric conditions at the cost of longer retention times [67, 68]. Low alkali concentrations (< 4% w/w) are used at high temperatures and pressures [50].
Widely used bases include hydroxides of potassium, sodium, calcium and sodium carbonate. KOH selectively removes xylan [69]. Sodium hydroxide pre-treatment, is commonly used due to high alkalinity for fractionation of various material, including agricultural residue and wood [70]. Dilute NaOH loosens the biomass structure, it separates the bonds between lignin and carbohydrates, increases internal surface area, decreases the degree of polymerisation and crystallinity and disrupts the lignin structure [49]. Homogenisation of the pre-treated biomass enhances the glucose yields by increasing surface area and porosity of the biomass [71]. High alkaline concentration increases biomass delignification, however, large concentrations (6-20% w/w) cause cellulose dissolution and reduced lignin removal [49]. Pederson *et. al* [72] observed that an increase in pH from 10-13 increased removal of lignin from 40-80 % w/w in dry wheat at 140 °C. Also, varying NaOH loading rate from 3-9% based on dry bagasse [73] increased delignification from 52-75 %.

Compared to acid hydrolysis pre-treatment, NaOH improves biodegradability because alkali has a better delignification ability. Ioelovich and Morag [74] applied both acid and base pre-treatment to four materials and found alkali to be more efficient in sugar yield, delignification and biomass use. Combining NaOH with other agents such as peracetic acid, polyelectrolyte and hydrogen peroxide gives good results [49]. The environmental impact is low and requires no special reactors. Lime pre-treatment: lime in the form of quick lime < CaO, and slaked lime,

$Ca(OH)_2$ has low cost, allows safe handling, is easy to recover and common [75-77]. In pre-treatment, lime and water are added to feedstock from room - 130 °C, oxygen enhances delignification. Lime improves biomass yield by removing acetyl groups and a large lignin fraction [73] reducing counter-productive cellulose adsorption [78] and formation of degradation by products [79] and promoting cellulose accessibility. The drawbacks of lime are long reaction periods (influenced by reaction temperature) when compared to NaOH under same conditions. Lime dissolves in water slower than NaOH, requiring higher volumes of water for pre-treatment. Sometimes lime may produce products with less favourable characteristics [49].

General drawback of alkaline methods: (i) not suitable for woody biomass due to severe conditions required to fractionate recalcitrant wood, (ii) lignin removal can be improved by using oxygenated methods [80] and addition of chemicals such as urea, (iii) loss of hemicellulose and formation of inhibitors at harsh conditions is another drawback, (iv) formation of slats on neutralisation presents disposal challenges and (v) the salts hamper the purification of pre-treated hydroxylates [81] and posttreatment washing results in loss of sugar. Wet oxidation, biomass undergoes oxidation in an aqueous (acidic, neutral and alkaline condition) solution via reaction with oxygen (air) at elevated temperature and pressure. The pre-treated suspension is filtered to separate the cellulose rich solid from the hemicellulose rich filtrate and the solid component is washed with deionised water [82]. Wet oxidation oxidises the hemicellulose fractions of material into intermediates such as carboxylic acids, by peeling reactions and cleavage, and from phenolic structures of lignin, [83] acetaldehydes and alcohols and finally to CO_2 and H_2O. The following method has become common practice regarding cell wall fractionation. This method was developed by Jermyn and Isherwood in 1959 [84]. Slight variations may exist with regards to the cell wall concerned [85]. The powdered cell wall material, dried either in an oven at 105 °C or using acetone. This is then treated with boiling water for 12 h followed by centrifugation and washing. The supernatant contains mostly pectic compounds with some soluble proteins. The residue is then sometimes treated with ammonium or potassium oxalate to completely remove pectic compounds. The residue is then subjected to mild chlorination, originated by Cross and Bevan [86]. This has two effects; it removes lignin and breaks any linkages between cellulose and the rest of the wall polysaccharides, collectively called hemicelluloses. The residue is called holocellulose. Treatment with 4N KOH at room temperature for a few hours then removes the alkali-soluble hemicelluloses leaving a residue called α-cellulose. The various extracts and the final residue may then be hydrolysed in mineral

acid (after reducing to smaller volume for extracts) and the constituent sugars separated by chromatographic methods [86]. The hemicelluloses yield a range of sugars including glucose, galactose, arabinose, xylose and mannose as well as some methylated sugars [86].

2.5. The chemical interaction between cellulose and photocatalyst

Because of the superfine structure of cellulose, it can support photocatalyst nanoparticles. This network provides chemical support and disperses the inorganic nanoparticles by providing a surface for nucleation [87]. The TiO_2/cellulose nanocomposites are forerunners in this composite field. The cellulose membrane allows the collection and removal of nanoparticle photocatalyst suspension in water after photocatalytic treatment which minimises contamination of the photocatalyst after wastewater treatment [88]. The optical properties of cellulose material enhance the electron distribution and transfer to the TiO_2 on the surface which increases photocatalytic activity of the TiO_2 [6 5]. In the cellulose membrane modification, anatase TiO_2 improves stability, hydrophilicity and anti-fouling properties [8]. This improves the cellulose membranes hydrophilic properties and permeability, also minimising fouling properties. Addition of TiO_2 is reported to increase the thermal stability of the resulting membrane. This increase in thermal stability will aid in withstanding high temperature and avoid degradation by UV radiation [89]. The covalent bond interaction between TiO_2 and cellulose increases rigidity in the polymer chain and enhances the energy to break down the polymer chain [89]. With the incorporation of TiO_2, more heat is adsorbed by the TiO_2 in the membrane, thereby increasing the delay in decomposition of cellulose. This arrangement of inorganic composite improves the membranes porosity, stability and performance [90]. The TiO_2 limits the molecular motion in the polymer chain [90].

In nature, cellulose has high hydrophilic properties because of the hydroxyl group that aid interaction with photocatalyst through hydrogen and electrostatic interaction. The functionality of cellulose based material can control condensation/polycondensation and nucleation growth processes, called in-situ precipitation [90]. This controls the growth of catalyst. Incorporation of TiO_2 nanoparticles could be adsorbed to the cellulose macromolecules by electrostatic interaction due to electron rich oxygen atoms of the polar hydroxyl groups that interact with the electropositive transition metal cations [91]. Unmodified cellulose shows lower adsorption capability which lowers the interaction between cellulose and metal ion. Chemical functionalisation techniques are applied to aid the immobilisation of photocatalyst

nanoparticles onto cellulose, these include halogenation, esterification, etherification, silylation, oxidation and grafting that is based on the hydroxyl group of the cellulose [92, 93]. TiO_2-cellulose composites have also been used to detect harmful gases in sensors. TiO_2-cellulose hybrid nanocomposite can be prepared by blending TiO_2 nanoparticles into a cellulose solution.

2.5.1. Techniques for fabricating cellulose hybrid nanostructured photocatalysts

Various methods are available for attachment of nanoparticles to cellulose base.

2.5.1.1. Sol-gel method

Sol-gel method is the controlled hydrolysis and condensation of suitable precursors, nitrates, metal alkoxides or chlorides due to good morphological control of the product properties including specific surface area, degree of aggregation and nanoparticle size [94-96]. The precipitates/gels from sol-gel method are amorphous with high specific surface area, sometimes mesoporous [94-96]. The cellulose is a good substrate because it can control nanoparticle size, enhance stability and keep the specific morphology [94-96]. The electrical [94], magnetic [95] and optical [96] properties of the inorganic nanoparticles can be maintained in the cellulose polymer matrix. Metal oxides from solution adsorb onto the hydroxylated surface and subsequent hydrolysis yields the nanoparticles [94-96]. Because this is all done at low temperature, it is considered a green pathway and a preferred method of synthesis [6]. Immobilisation of titania has been done before according to [9] via sol-gel. The anchoring process involves forming chemical bonds and esterification of surface hydroxyl groups with titanols. The homogenous titania sticks to and protects the cellulose fibres from aggregation of O^{2-} and ·OH species that are produced during light exposure and does not induce simultaneous fibre degradation. A larger surface area due to smaller particle size makes for better photocatalytic performance [9].

2.5.1.2. Hydrothermal method

Hydrothermal method prepares micro and nano-sized crystalline metal oxides with good shape control. Synthesis is carried out in an autoclave with high temperature. This process dissolves and recrystallizes materials not normally soluble under normal conditions [97, 98].

2.5.1.3. Electrospinning method

Electrospinning is a simple, multipurpose, cost effective method synthesises 1D fibres from different material, including composite, polymer and ceramic using polymer solutions. It is a non-mechanical and electrostatic technique that uses an electric field or high voltage to charge the surface of a polymer droplet and later induce the ejection of a liquid jet through a spinneret [99]. An electrical potential is applied between a polymer droplet and a grounded target. When the electric field overcomes the surface tension of the droplet, a charged jet of polymer solution is ejected [99]. Parameters that need to be considered, especially of the polymer solution are, surface tension, dielectric constant, viscosity, conductivity and weight of the polymer to form ultrafine fibres [99-101]. The polymer concentration must be able to overcome viscosity which prevents motion from the electric field and promote polymer entanglement [103-105 81-83]. The spun nanofibers have high porosity, high surface to volume ratio, malleability to conform to various shapes and sizes, and ability to control composition [99-101].

2.5.1.4. Atomic layer deposition method

Atomic layer deposition (ALD) creates a film by surface reaction of gaseous precursors. The precursor vapours are fed into the reactor and the precursor pulses are separated by inert gas purges [102]. After which, the substrate surface is saturated by a monolayer of that precursor. Since the gas phase does not have precursor, the subsequent precursor only reacts with the adsorbed surface layer. Surface growth occurs in layers and film thickness can be controlled by deposition cycles. Metal alkoxides or halides are common precursors in the preparation of metal oxides and water is the oxygen precursor. Crystallinity of the metal oxide nanoparticle depends on deposition temperature [102, 103].

2.5.1.5. Hot press method

Hot press is a high temperature, high pressure method on powder to create sintered components. Pressure increases the driving force for dispersion and reduces the processing temperature for further sintering. This method can retain a homogenous functional composite film without sacrificing the morphology of the nanofiber photocatalyst. Powder coating deposits a powder material onto the target surface and a curing phase to create a steady intact film. Low temperature melting additives are employed to promote film formation. Because cellulose forms hydrogen bonds with other composites, there is some strain in re-dispersing them if dried. This characteristic also gives high mechanical reinforcement and thermos-mechanical stable films that may be used in laminate composites [104, 105].

2.5.2. Metal oxide cellulose nanocomposites

Natural cellulose, nanocrystalline or nano fibrillated has unique properties including a high Youngs modulus, dimensional stability, low thermal expansion coefficient, reinforcing potential and transparency [106]. Hybrid cellulose nanocomposites have been studied for application in biosensors, disposable chemical sensors, energy conversion, photocatalysis and many others [106]. The addition of metal oxides to cellulose increases the chemical stability, mechanical properties, conductivity and photosensitivity, which promotes the use of cellulose [106].

2.6. Nanotechnology

Nanotechnology is the use of nanomaterial in useable devices and forms. There has been great focus on the synthesis, structure, control of size and characteristic properties [107-109]. Nanostructures are now in use in most products on the market, with various uses as well. These uses are related to the properties of the nanomaterials such as good mechanical, thermal, catalytic, electronic and chemical properties.

2.6.1. Nanostructures and nanomaterials

Nanomaterials and nanostructures are materials that have dimensions less than 100 nm [109, 110]. Their properties distinguish them from bulk, single atom or molecular counterparts. Interest in these materials has grown over the past few decades due to their application in many fields, because of the properties they exhibit. Nanomaterials can be classified according to their size and shape, both of which affect their properties, and they can vary from zero dimensional (0-D) to three dimensional structures (3D) [109, 111]. In the Figure 2.4 below is the different structures shown. Zero dimensional nanostructures include nanoparticles, nanoclusters and nanocrystals. They also include quantum dots (1-10 nm) that display quantum confinement effects, which, at certain dimensions, make them useable at different energy levels [109, 112, 113]. One-dimensional nanostructures include nanorods, nanowires and nanotubes. Two-dimensional nanostructures include thin films and nanoplatelets. Three dimensional nanostructures include nanocubes [109].

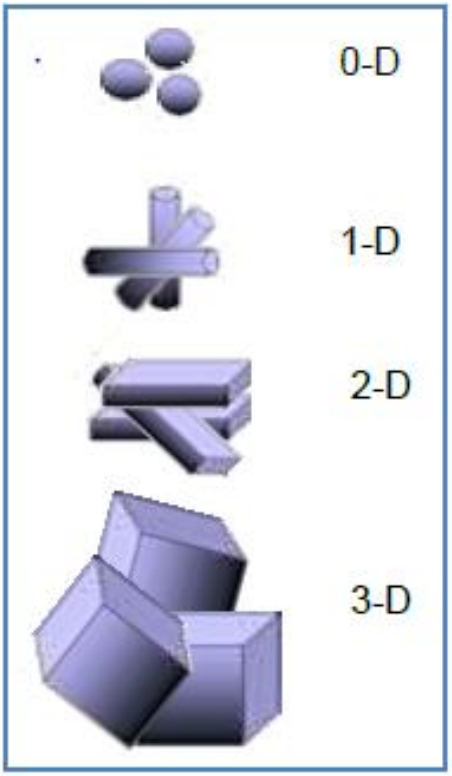

Figure 2.4: Classification of nanomaterials [109, 111].

2.6.2. The solution phase chemical synthesis of nanomaterials

There are two general approaches to fabricating nanomaterials, a top-down or bottom-up approach. The top-down approach involves breaking the bulk material down until the desired nanomaterials are obtained. This method is not widely used due the number of imperfections imposed on the material surface [109, 114]. The bottom-up method grows nanomaterials from single atoms into clusters. This method generates less defects and better homogeneity compared to the top-down method.

2.6.3. Nucleation and growth of nanoparticles in solution

Nanomaterials are readily obtained in solution by precipitation, which forms by nucleation, a result of supersaturation after the solute concentration has exceeded the equilibrium solubility of the solution [109,114]. The high Gibbs energy of the solution because of super saturation decreases the overall energy to preserve an equilibrium concentration in the solution [109, 114-116]. This nucleation process is thermodynamically driven and is referred to as homogenous nucleation. The solute molecules combine to produce nuclei without a solid interface [109, 116]. The overall free energy, ΔG (equation 2.2) of the reaction, is the sum of

the free energy due to formation of a new volume and the free energy due to the new surface that has been created [109, 116].

$$\Delta G = -\frac{4}{3}\pi r^3 k_B T ln(S) + 4\pi\pi^2\gamma \qquad \text{Equation 2.2}$$

For spherical particles, v is the molecular volume of the precipitated species, r is the radius of the nuclei, k_B is the Boltzmann constant, S is the saturation ratio and γ is the surface free energy per unit surface area. When S > 1, ΔG has a positive maximum value at a critical size r* as shown in the figure below.

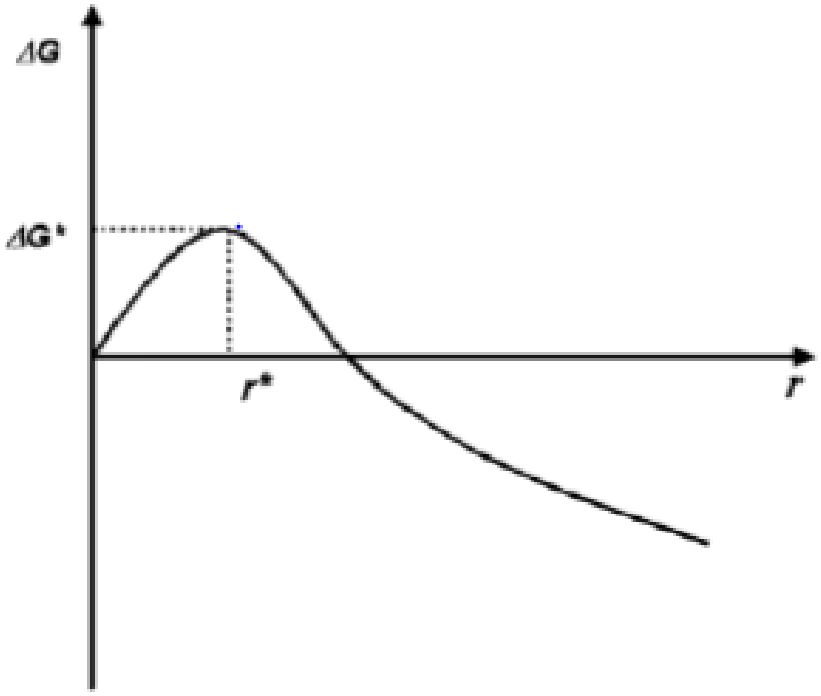

Figure 2.5: Illustration of the overall energy ΔG as a function of the growth particle size [109, 117].

When the nuclei sizer is larger than the critical size, the growth free energy decreases and the stable nuclei grow to form particles. When r = r*, dΔG/dr = 0 and the critical size r are given by:

$$r* = \frac{2Vr}{3k_B T ln(S)} \qquad \text{Equation 2.3}$$

For a given S value, all particles with r, r* will grow and all particles with r < r* will dissolve [109, 116]. This is due to the critical size r* being the minimum particle size achieved to begin

nucleation. From the equation, the critical nuclei size r* is inversely proportional to the saturation ratio S. After nuclei formation from solution, molecular addition growth occurs. When the concentration dips below the critical level, nucleation stops, and particle growth continues by molecular addition until the precipitated species equilibrium concentration is reached [109, 116]. Uniform size distribution can be achieved by a short nucleation period, which will generate the particles at the end of the reaction, and this will be followed by a self-sharpening growth process. At this stage, the free energy driving force is larger for small particles making them grow faster than the larger particles. At this point, size focusing occurs. An almost monodispersed size distribution can be gained by stopping the reaction quickly or by supplying a reactant source to keep a saturated condition during the course of the reaction [109].

When the reactants deplete due to particle growth, Ostwald ripening, defocusing occurs, the larger particles will continue growth and the smaller particles shrink until completely dissolved [117]. Any particles smaller than the new critical size will dissolve because the saturation (S) decreases and the corresponding nuclei size (r*) increases [117]. If the reaction is quickly stopped here, the particles will have a broad size distribution, shown by distributing two size regimes, a larger and smaller one. When there are no reactants left in a reaction, the saturation ratio will decrease while the critical nuclei size increases. To achieve a short burst of nucleation will require a high saturation ratio(S) [58 49]. Molecular addition is the deposition of soluble species on the solid surface [58]. Particles grown by aggregation with other particles is called secondary growth and has a particle growth rate larger than that of molecular addition. After the particles grow to a stable size, growth continues by combining with smaller, unstable nuclei and not through collisions with other stable particles. A method is required that allows nanoparticles to settle during a reaction because they are small and not thermodynamically stable. This may be achieved by adding surfactant protecting agents, such as organic ligands and inorganic capping materials [118, 119], or place them in an inert environment such as an inorganic matrix or polymer [116]. The stability of nanocrystal dispersion is promoted by favourable interactions between the capping groups and the solvent, which provides an energy barrier to counteract the van de Waals forces, and for magnetic material, the magnetic attraction between the nanoparticles [116]. Different solvents may be used to change the solubility or reaction rate to help arrest the nanoparticles [116, 120].

2.7. Background of TiO_2

Since discovery, TiO_2 has been used as a pigment, in sunscreen, paint, ointments, toothpaste, etc. After the discovery of photocatalytic splitting of water on a TiO_2 electrode under UV light, TiO_2 has been used in photovoltaics, catalysis and sensors [125]. The movement of electrons and holes in semiconductor nanostructures is governed by quantum confinement and the transport properties are related to phonons and photons, governed by size and geometry of the material. The specific surface area and surface-to-volume ratio increases as the material size decreases. The smaller particle size increases surface area, which is beneficial when using TiO_2 -based devices [126]. TiO_2 is a useful photocatalyst and is being thought of as a solution to many environmental challenges. The Removal of labile oxygen atoms causes oxygen vacancies and reduces Ti to Ti^{3+}, hence it can be used as a heterogeneous catalyst and photocatalyst [127]. As the size, shape and crystal structure of titania nanomaterials vary, the surface stability changes and transitions between different phases under pressure or heat become size dependent [128]. Most applications of titania are in the visible region.

2.7.1. Properties of TiO_2

2.7.1.1. Structural properties of TiO_2 nanomaterials

The structures of anatase and rutile titania are described in terms of chains of TiO_6 octahedra, where each Ti^{4+} ion is surrounded by an octahedron of six O^{2-} ions. Each octahedron in the two crystal structures differ in orientation [128]. Rutile has a slight orthorhombic distortion. The anatase octahedron has symmetry lower than orthorhombic. The Ti-Ti distance is larger in anatase, while the Ti-O distance is shorter compared to rutile. In rutile, each octahedron is in contact with ten neighbour octahedrons (two sharing edge oxygen pairs and eight sharing corner oxygen atoms). In anatase, each octahedron is in contact with eight neighbours (four sharing an edge and four sharing a corner). The difference in lattice structure creates differences in mass densities and electronic band structures [128]. The density of the surface states of nanoparticles was dependent on the synthesis method [128, 129]. The titania prepared from basic sol and more surface states than those prepared by acidic sol based on the surface voltage spectroscopy study [128]. TiO_2 is a transition metal oxide with three kinds of phase structures, anatase (tetragonal), Rutile (tetragonal) and brookite (orthorhombic), with a band

gap of 3.2, 2.96 and 3.02 eV respectively [129-132]. Anatase and rutile are more stable than brookite and have more applications. Rutile TiO_6 has a tetragonal structure and contains 6 atoms per unit cell, where the TiO_6 octahedron is slightly distorted [130,133, 134]. Anatase has a tetragonal structure with the distortion of the TiO_6 octahedron being larger than rutile. Rutile, however, is more stable at higher temperature and pressure. Amorphous titania can be prepared, but with heat treatment, a phase transformation can occur, increasing the annealing temperature to between 300-500 °C, amorphous structures can be changed into anatase, and when the temperature increases, 600-700 °C, anatase can be further transformed into rutile [130, 135]. This crystal is an n-type semiconductor that is electron rich [130].

There are three different crystalline allotropes known: anatase, rutile and brookite (Table 2.1 and Figure 2.6), all of which can be synthesised via sol-gel method. Rutile is highly thermodynamically stable, anatase is kinetically stable using sol-gel at neutral pH. Brookite is the uncommon allotrope. All of these allotropes have oxygen bound to three titanium atoms, the bulk titanium atoms are hexacoordinated. The titanium centres in rutile have a D_{2h} symmetry whereas oxygen has a C_{2v} symmetry. The titanium centres in anatase show D_{2d} symmetry and oxygen has C_{2v} symmetry. In brookite, which is less symmetrical, the Ti-O bonds have different lengths around the same Ti atom, giving it C_5 symmetry. Two different types of oxygen are present in brookite and both show Cs symmetry [127].

Table 2.1: Crystal structures of titanium dioxide allotropes [59]

	Rutile	Anatase	Brookite
Crystalline system:	Tetragonal	Tetragonal	Orthorhombic
Unit cell:	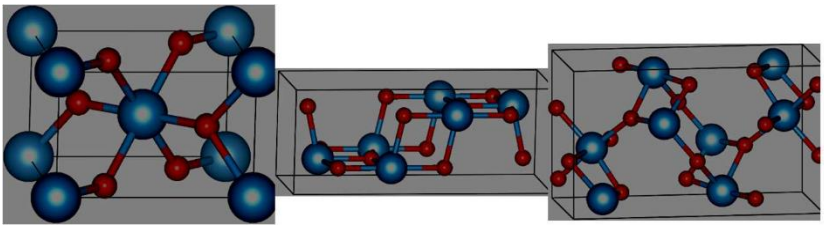		

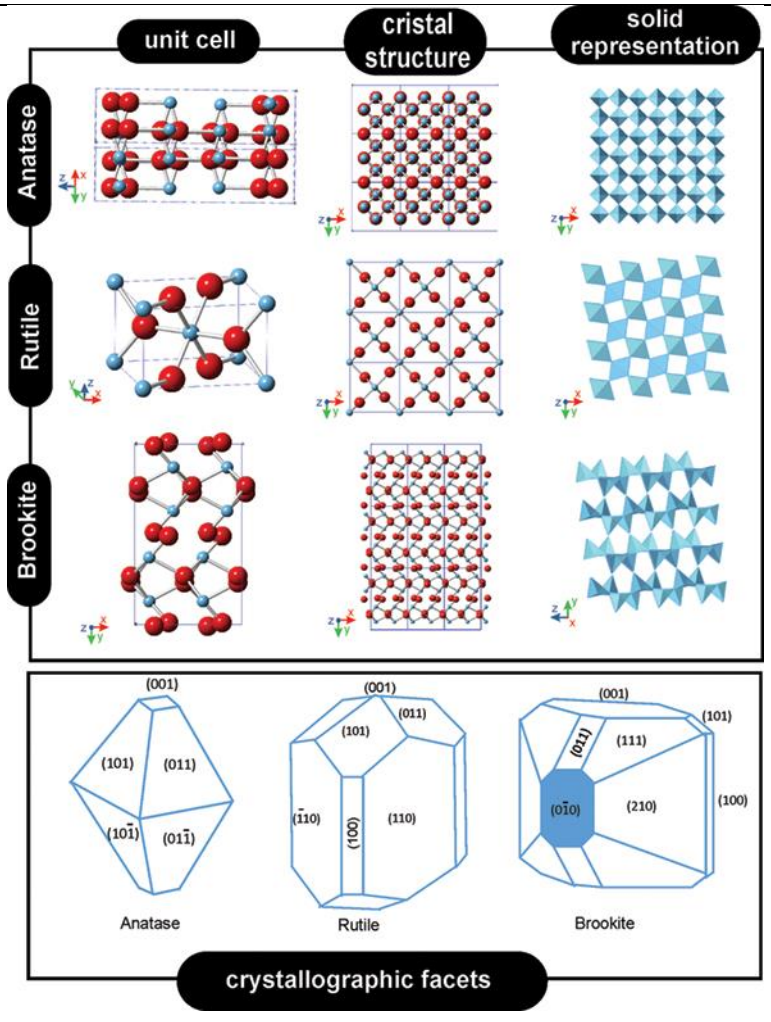

Figure 2.6: crystal structure of titania allotropes [136].

There are three different facets of anatase that are common {101}, {100} and {001} facets. There are four exposed facets of anatase that are obtained by hydrothermal synthesis, {101}, {001}, {100} and {110}.

2.7.1.2. Surface chemistry of the {101} facet

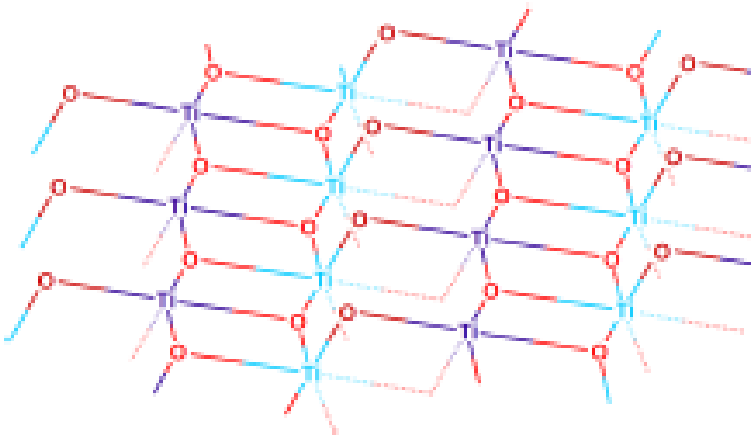

Figure 2.7: Clean anatase {101} surface. Ti_{VI} and Ti_{V} are respectively light and dark blue, μ_3O and μ_2O are respectively light and dark red. Dashed lines are bonds towards the bulk [127].

The {101} facet is the most common of anatase and makes approximately 90% of the thermodynamic surface. It has both T_{IV} and Ti_{VI} (5 atoms. nm^{-2} for each) as well as μ_2 O (5 atoms. nm^{-2}) and μ_3 O (10 atoms. nm^{-2}). It has the smallest density of uncoordinated atoms and the lowest surface energy [127].

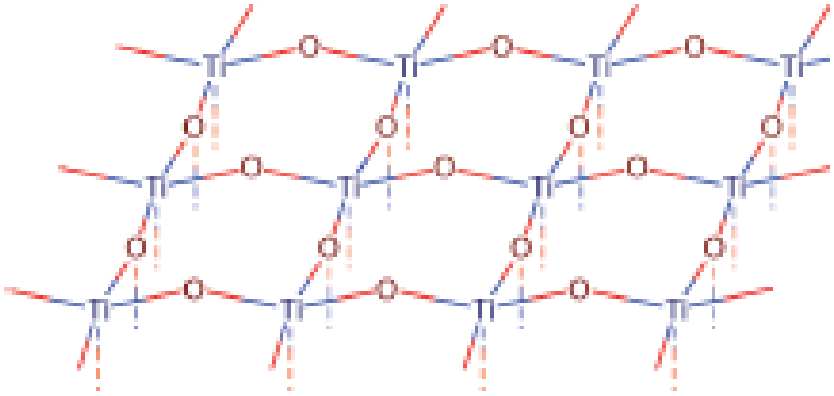

Figure 2.8: Clean anatase {001} surface. Dashed lines are bonds towards bulk atoms [127]. The {001} facet has a high density of T_{IV} sites (6.74 atoms. nm^{-2}) along with μ_2-O and μ_3-O sites (9.74 atoms. nm^{-2}). It has the highest surface energy at 0.88-0.98 $J.m^{-2}$ [127, 137-139].

The metastability of anatase as a function of pressure has been reported to be size dependent with smaller crystallites preserving the structure to higher pressures [140].

2.7.2. Thermodynamic properties of TiO_2 Nanomaterials

Rutile is stable at high temperature, but anatase and brookite are found in fine grained natural and synthetic samples. The crystal structure depends on the method of preparation [128, 141, 142]. The phase also changes with varying temperature and size of the particles. Equally sized nanoparticles, anatase is thermodynamically stable for sizes < 11 nm, brookite is stable for sizes between 11-35 nm and rutile is stable for sizes > 35 nm [143]. At high temperature, rutile is the preferred stable phase, whereas anatase and brookite are common in fine grained (nanoscale) natural and synthetic samples [128]. On heating concomitant with coarsening, the following changes can be seen, anatase to brookite to rutile, brookite to anatase to rutile, anatase to rutile, brookite to rutile [128]. The transformation sequence implies that the energetics as a function of particle size is balanced [128]. Under conditions that preclude coarsening, the surface enthalpies of the three polymorphs crossover in thermodynamic stability, with anatase and brookite being stable at small particle sizes [128, 144, 145]. The initial particle size of anatase and brookite determines the transformation sequence and thermodynamic phase stability [128, 145].

2.7.3. Photon-induced electron and hole properties of titania nanoparticles

When titania nanoparticles absorb, impinging photons with energies that are equal to or higher than its band gap (> 3.0 eV), electrons are excited from the valence band to the unoccupied conduction band. This causes a positive hole in the valence band and excited electrons in the conduction band. The charge carriers can recombine, non-radiatively, radiatively, or are trapped, and react with electron donors/acceptors on the surface of photocatalysts. The rate of these processes determines the efficacy of the titania [146]. The process is expressed below [147]:

$$TiO_2 + hv \rightarrow e^- + h^+ \quad \text{Equation 2.4}$$

$$e^- + Ti(IV)O - H \rightarrow Ti(III)O - H^-(X) \quad \text{Equation 2.5}$$

$$h^+ + Ti(IV)O - H \rightarrow Ti(IV)O^{\cdot} - H^+(Y) \quad \text{Equation 2.6}$$

$$h^+ + \frac{1}{2}O^{2-}_{lattice} \leftrightarrow \frac{1}{4}O_2(g) + vacancy \quad \text{Equation 2.7}$$

$$e^- + O_{2,s} \rightarrow O^-_{2,s} \quad \text{Equation 2.8}$$

$$O^-_{2,s} + H^+ \rightarrow HO_{2,s} \quad \text{Equation 2.9}$$

$$h^+ + Ti(III)O - H^- \rightarrow Ti(IV)O - H \quad \text{Equation 2.10}$$

$$e^- + Ti(IV)O^{\cdot} - H^+ \rightarrow Ti(IV)O - H \quad \text{Equation 2.11}$$

$$O_{2,s} + Ti(IV)O^{\cdot} - H^{+} \rightarrow Ti(IV)O - H + O_{2,s} \qquad \text{Equation 2.12}$$

Equation 2.4 is the photon absorption process. Equation 2.6-10 is the photocatalytic degradation pathway. Equation 2.11-12 is the recombination pathway [148]. Equations 7 and 8 are the hole pathways competition, causing bound OH radicals and O vacancies. The reverse of Equation 8 creates O adatom intermediates upon exposure of O^{2-}(g) to defective sites [128, 147]. Electrons and holes generated in titania nanoparticles are localised at different defective sites on the surface and in the bulk [128]. Electron paramagnetic resonance (EPR) studies found that electrons are trapped as two Ti (III) centres, with holes being trapped as oxygen-centred radicals that are covalently bonded to surface titania atoms [128, 148-151]. With band gap illumination, holes appear at the surface and preferentially recombine with electrons trapped in the surface for mixed phase titania such as Degussa P25, also, surface reactions following charge migrations dominate recombination reactions [128, 151].

O_2 is an efficient scavenger of conduction band electrons at the gas/solid as well as the build-up of trapped carriers eventually result in extended surface reconstruction involving Ti-OH functionality [128, 147]. Photo-generated free conduction band electrons pair with acoustic phonons in the lattice, also, their lifetime increased when dehydrated [128, 149]. Photoexcited charge carriers in titania nanoparticles produce Stark effect intensity and wavelength shifts for surface TiO-H stretching vibration [152]. For UV-light induced electron hole pair excitations in anatase titania nanoparticles, the localised states such as holes trapped at oxygen anions (O^{-}) and electrons trapped at coordinatively unsaturated cations (Ti^{3+}) were accessible to EPR spectroscopy. Delocalised and EPR silent electrons in the conduction band can be traced by their infrared (IR) absorption which is a result of their electron excitation from within the conduction band in the IR region as seen in Figure 11 [152]. Under continuous UV radiation, photogenerated electrons are either trapped at localised sites, creating paramagnetic Ti^{3+} centres, or they remain in the conduction band as EPR silent species which can be observed by IR spectroscopy [153].

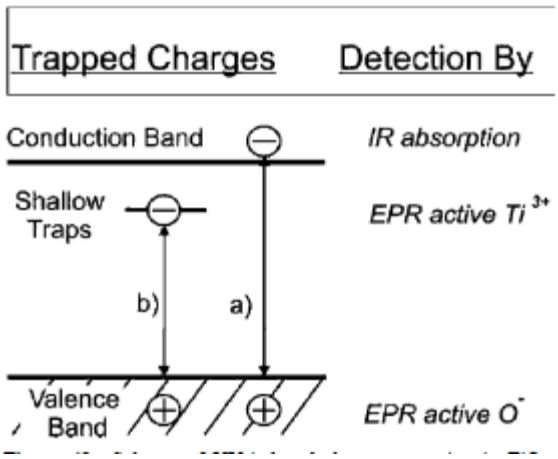

Figure 2.9: Scheme of UV-induced charge separation in TiO_2. Electrons from the valence band can either be trapped by (a) defect states, located close to the conduction band (shallow traps), or (b) in the conduction band, where they produce absorption in the IR region. Electron paramagnetic resonance spectroscopy detects both electrons in shallow traps, Ti^{3+}, and hole centres, O^- [152].

2.8. Synthesis methods of TiO_2

The synthesis of TiO_2 into nanoparticles, nanorods, nanowires and nanotubes can be done by many processes, including sol-gel method, micelle and inverse micelle, thermal, solvothermal, direct oxidation, chemical vapour deposition, physical vapour deposition, electrodeposition, sonochemical and microwave-assisted methods [143]. As the size, shape and crystal structure of TiO_2 nanomaterials vary, the surface stability and the transition between different phases under pressure or heat changes and become size dependent [143]. The crystal structure produced by these methods is usually rutile or anatase and are somehow amorphous [130]. Specific temperatures and pressure is required to create specific crystal phase structures. The geometry of the TiO_2 nanomaterial can vary from nanosphere to one dimensional (1D) up to 3D. Nanotube arrays (NTs) have been produced by electrochemical oxidation reaction of a metallic titanium substrate and are the most popular nanostructure [130, 154-158]. Tubular nanostructures have been synthesised from template such as ZnO nanowires (NWs). Various strategies shave been developed for the conversion of ZnO to TiO_2 nanowires [130, 159-161]. Nanowires/nanorods (NWs/NRs) are other 1D structures that are prepared using methods such as chemical vapour deposition (CVD), direct oxidation and hydrothermal method [130].

2.8.1. Microwave synthesis

Microwave irradiation is becoming popular in synthesising biological, organic, inorganic and polymer nanostructured materials. It is a green method involving reduced amounts of solvent and less energy, as well as cost efficient. It is fast and requires no further heat treatment for product formation [130]. The titanium butoxide precursor has more reactivity compared to others due to variable oxidation capability. Titanium (IV) butoxide reacts with deionised water, which causes hydrolysis and condensation. With the titanium ion precursor, a vacant d orbital can increase the coordination number from 4 to 6. The reaction kinetics [163]:

$$Ti(OCH_4H_9)_4 + 4H_2O = Ti(OH)_4 + 4C_4H_9OH \quad \text{Equation 2.13}$$

$$Ti(OH)_4 = TiO_2 \downarrow + 2H_2O \quad \text{Equation 2.14}$$

During the precipitation, the primary particles nucleate initially and aggregate to form secondary particles that results in a spherical aggregate of nano sized crystalline titania.

2.8.2. General principles of hydrothermal synthesis

In a sol-gel process, a colloidal suspension (sol) is formed from the hydrolysis and polymerisation reaction of the starting material, usually an inorganic metal salt or metal organic compound (metal alkoxides). The complete polymerisation and loss of the solvent transitions from the liquid sol into a solid gel phase [128]. Nano-titania has been synthesised using the sol-gel process by the hydrolysis of titanium precursors [152, 153, 164-167 90-95]. This process usually occurs by an acid-catalysed hydrolysis step of titanium (IV) butoxide followed by condensation [152, 168-169]. The production of Ti-O-Ti chains is favoured with low water content, low hydrolysis rates and excess titanium alkoxide in the reaction mixture. The Ti-O-Ti chains produce a 3D polymeric skeleton with close packing. The formation of Ti-$(OH)_4$ is favoured with a high hydrolysis rate from a medium amount of water [112 43]. Large amounts of Ti-OH and not enough 3D polymeric chain development lead to loosely packed first order particles [112]. When there is an excess of water, polymeric Ti-O-Ti chains develop. Closely packed first order particles are generated by the 3d developed gel skeleton [170-172]. A study on the growth kinetics of titania using titanium tetraisopropoxide precursor showed that the rate constant increased with temperature due to the dependence of viscosity and the equilibrium solubility of titania on temperature. Secondary particles were formed by epitaxial self-assembly of the primary particles with a longer time and higher

temperature, also, the number of primary particles per secondary O particle increased over time. Average titania nanoparticle radii increased linearly over time which agreed with the Lifshitz-Slyozov-Wagner model for coarsening [128, 173]. Highly crystalline anatase titania can be produced with different sizes and shapes by the polycondensation of titanium alkoxide in the presence of tetramethylammonium hydroxide [128, 174, 175]. Sugmoto *et al.* conducted a series of studies on the sol-gel method of formation of titania with different shapes and sizes by varying the reaction parameters [176-178]. Amines were used as shape controllers in these reactions, the shape of titania changed from cuboidal to ellipsoidal at higher pH. The shape control was attributed to the growth rate of different crystal planes by specific adsorption of shape controllers under different pH conditions [128, 179].

Prolonged heating time below 100 °C can be used to overcome agglomeration of titania nanoparticles [180]. In air, a large number of single-phase nanoparticles with an average size of between 7 and 50 nm can be obtained [181-185]. Nanorods have been synthesised using a combination of sol-gel and anodic alumina membrane (AAM) templates. The porous AAMs are dipped into a boiled titania sol and then dried and heated [186, 187]. Titania nanotubes can also be obtained by sol-gel by templating with an AAM and other organic compounds [188, 189]. The sol-gel method is one of the processes that efficiently control the morphology of anatase [147]. Hydrothermal precipitation proceeds from metal alkoxydes by hydrolysis, followed by condensation, nucleation and growth of the hydrolysis product to the desired oxides [127].

- Hydrolysis

When a metal oxide $M(OR)_x$ is placed in the presence of water, the nucleophilic character of water leads to substitutions between the alkoxide ligands that depend on the solutions acidity: At low pH, aquo ligands ($M\text{-}OH_2$) are present in the coordination sphere and are increasingly deprotonated into hydroxo (M-OH) ligands at higher pH. Aquo or hydroxo ligand addition can cause an increase in the metal coordinance when thermodynamically favoured.

$$Ti\text{-}OR + H_2O \longrightarrow Ti\text{-}OH + HO\text{-}R \qquad \text{Equation 2.15}$$

- Condensation

Complexes that have hydroxo ligands can condense via two different mechanisms:

Olation occurs when a hydroxo ligand of a metal centre forms a bridging OH group between two metals with the departure of a highly labile aquo group:

$$Ti\text{-}OH + H_3O^+ \longleftrightarrow [Ti\text{-}OH_2]^+ + H_2O \qquad \text{Equation 2.16}$$

$$Ti\text{-}OH + H_2O\text{-}Ti \rightarrow Ti - \overset{\overset{O}{|}}{O} - Ti + H_2O \qquad \text{Equation 2.17}$$

Oxolation occurs in the absence of aquo ligands that were initially present: a hydroxo ligand can still form a bridging OH group between two metal centres. The proton from the bridge is transferred to another non-bridging hydroxo ligand, which then ejects the metal as a water molecule.

$$Ti\text{-}OH + OH\text{-}Ti \rightarrow Ti\text{-}O\text{-}Ti\text{---}\overset{\overset{H}{|}}{Ti}\text{-}O\text{-}\overset{\overset{OH}{|}}{Ti} + H_2O \qquad \text{Equation 2.18}$$

- Nucleation

Once the hydroxyl group bearing metal for polymerisation is present in solution and whether growth of a crystallite from an oligomeric species is thermodynamically favoured depends on two factors [174]:

- The bulk energy: bulk species of a crystallite phase are more stabilised than in solution, hence more bulk species generated by condensation is more thermodynamically favoured.
- The interfacial energy: species in solution are more stable than undercoordinated species on the crystal surface. Condensation causes an increase in the particle surface which is thermodynamically less favourable. The condensation of dissolved species into smaller particles with a high surface/volume ratio is thermodynamically unfavoured, until the particle reaches a size where its bulk energy overcomes its surface energy to make growth favourable. The formation of the nuclei is called nucleation and occurs once the metal concentration in the solution is over and above saturation. From this point on, growth occurs by addition of a metal complex from the solution on the metal oxide surface [184].

2.8.3. Micelle and inverse micelle methods

Micelles are an aggregate of surfactant molecules that are dispersed in a liquid colloid when the surfactant concentration surpasses the critical micelle concentration (CMC) [128]. The CMC is the concentration of surfactants in free solution that is in equilibrium with surfactant aggregate forms. In the micelle, the hydrophobic hydrocarbon chain of the surfactant is oriented toward the interior of the micelle, whereas the hydrophilic groups are oriented on the exterior in the surrounding aqueous medium. The lipid concentration in the solution determines the molecular organisation of surfactants and lipids. Reverse micelles can also form in different solutions where the hydrophobic groups are on the interior of the micelle. Micelles are mostly globular and roughly spherical in shape; however, ellipsoids, cylinders and bilayers are possible. The micelle shape is a function of the molecular geometry of the surfactant molecule and the solution conditions such as temperature, concentration, pH and ionic strength [70]. This method is commonly employed in titania synthesis [190-192]. This method normally produces amorphous titania structure, but calcination is required for high crystallinity. This usually causes agglomeration of the titania particles [164].

2.8.4. Sol method

This is the nonhydrolytic sol-gel process involving the reaction of titanium chloride with different oxygen donor molecules (metal alkoxide or organic ether) [126, 144, 145].

$$TiX_4 + Ti(OR)_4 \rightarrow 2TiO_2 + 4RX \qquad \text{Equation 2.19}$$

$$TiX_4 + 2ROR \rightarrow TiO_2 + 4RX \qquad \text{Equation 2.20}$$

The condensation between Ti-Cl and Ti-OR forms Ti-O-Ti bridges. The alkoxide groups are provided by titanium alkoxides or can be formed in situ by reacting titanium chloride with alcohols or ethers [126].

2.8.5. Hydrothermal method

Usually carried out in an autoclave with or without Teflon liners under controlled temperature and pressure in aqueous solution. The pressure is determined by the temperature and amount of solution in the vessel. Widely used for small particle production in the ceramics industry, however, can be used to prepare TiO_2 [193-195].

2.8.6. Solvothermal method

Similar to the hydrothermal method, except that the solvent used is nonaqueous. In this method, the temperature chosen can be much higher as compared to hydrothermal method due to the nature of the solvent chosen. This method has better control of size, shape and crystallinity of the titania nanoparticles produced [165, 166].

2.8.7. Direct oxidation

The oxidation of titanium metal using oxygen or anodization. Crystalline titania nanorods have been produced by the direct oxidation of a titanium metal plate using hydrogen peroxide [196-198].

2.8.8. Chemical vapour deposition (CVD)

CVD is the process through which a material in the vapor state is condensed to form a solid material. It is usually used to form coatings that change the mechanical, electrical, thermal, optical, and corrosive and wear resistance properties. They are also used to from free-standing bodies, films and fibres that penetrate fabrics, forming composites. This process occurs in a vacuum chamber. In CVD, thermal energy is used to heat the gas in the coating chamber, which drives the deposition reaction.

2.8.9. Physical vapour deposition (PVD)

Physical vapour deposition (PVD) occurs without a chemical reaction [167, 199]. Materials are evaporated and then condensed to from a solid. Primary PVD methods include thermal deposition, ion plating, ion implantation, sputtering, laser vaporisation and laser surface alloying [167, 199].

2.8.10. Electrodeposition

Used to produce a coating on a surface by reduction at the cathode. The substrate to be coated is used as the cathode and immersed into a solution containing a salt of the metal to be deposited. The metallic ions are attracted to the cathode and reduced to the metal form [200].

2.8.11. Sonochemical method

Ultrasound has been used to produce many nanomaterials which include high-surface-area transition metals, alloys, carbides, oxides and colloids. The chemical effects of ultrasound are

not a direct effect of the interaction of molecular species. It is, acoustic activation, the formation, growth and implosive collapse of bubbles in a liquid. The cavitational collapse produces an intense heat (> 5000 K), high pressure (~1000 atm) and massive heating and cooling rates (> 10^9 K/s) [201, 202].

2.9. Modifications of titania nanomaterials

The optical properties of TiO_2 relate to many of its applications. The wide band gap however does limit its use somewhat. The band gap of bulk titania is in the UV range (3.0 eV for rutile and 3.2 eV for anatase), which is a fraction of the sun's potential [203]. Increasing the optical activity of TiO_2 nanomaterials by shifting the onset of the response from the UV to the visible region is one solution to improve performance [204-207]. Some ways to achieve this include doping with other elements to narrow the electronic properties, altering titania's optical properties. Sensitising titania with other colourful inorganic or organic compounds to improve optical activity in the visible range. Coupling collective oscillations of the electrons in the conduction band of titania with those of other metals in a metal-TiO_2 nanocomposite to improve performance. Also, modifying the TiO_2 nanomaterial surface with other semiconductors can change the charge transfer properties between TiO_2 and the environment to improve performance [204-207].

2.10. Applications of TiO_2 nanomaterials

Current applications of TiO_2 include paint, toothpaste, UV protection, photocatalysis, photovoltaics, sensing, electrochromics and photochromics. The titania nanomaterials have a band gap around 3.0 eV and have a high absorptivity in the UV range. The nanomaterials are stable, nontoxic and cheap. The nanoparticles can be used as an antifogging agent on glass [128, 208-211]. When sensitised with organic dyes or inorganic narrow band gap materials, TiO_2 can be used for solar applications by absorbing light in the visible region and converting solar energy into electrical energy [212-214].

2.11. TiO_2 photocatalysis

TiO_2 is one of the most effective and environmentally friendly photocatalyst. It has been used in the photodegradation of many pollutants [215-222]. The process of photocatalytic degradation by semiconductors is straight forward. When the TiO_2 absorbs photons with an energy that is larger than its band gap, electrons are excited from the valence band to the

conduction band, this creates electron-hole pairs. These charge carriers then migrate to the surface and react with the chemicals that are adsorbed on the surface by decomposing them. The photodecomposition process commonly involves one or more radicals or intermediate species. The semiconductors photocatalytic activity is controlled by light absorption properties, such as light absorption spectrum and coefficient, reduction and oxidation rate on the surface by the electron and the hole, and lastly, electron-hole recombination rate [112]. With this in mind, the larger the specific surface area, the higher the photocatalytic activity will be. However, the surface is considered a defective site, a larger surface area has a faster recombination rate. With a higher crystallinity, there are fewer bulk defects, which gives a higher photocatalytic activity. A high temperature treatment improves the crystallinity, but can cause aggregation of small nanoparticles, decreasing the surface area. With these conditions in mind, an optimal condition can be found [112, 128].

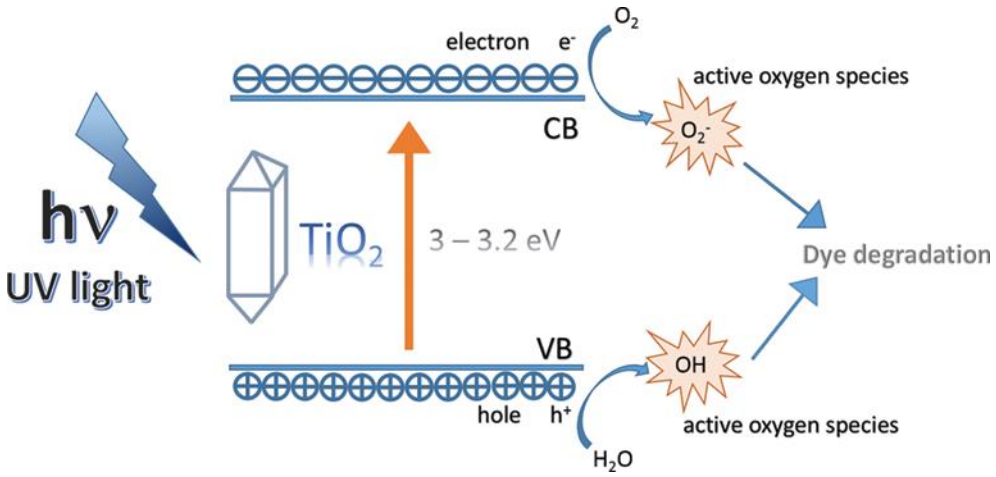

Figure 2.10: The photocatalytic degradation mechanism of TiO_2 on dye [136].

2.11.1. Pure TiO_2 nanomaterials: first generation

The catalytic activity can be enhanced by decreasing the particle size, increasing the number of particles located at the surface, giving a higher surface area to volume ratio [224]. An increase in band gap energy with decreasing particle size can enhance the redox potential of the valence band holes and the conduction band electrons to allow photo redox reactions, which do not proceed in the bulk material otherwise [224]. A disadvantage of titania nanoparticles is that they can only use a small percentage of sunlight for photocatalysis. There is an optimal size for specific photocatalytic reactions [225]. In hydrogenation reactions, the activity of TiO_2 nanoparticles increased with decreasing diameter [225]. In the decomposition of chloroform, it was found that there is an optimal size for maximum photocatalytic

efficiency [226]. In large titania particles, bulk recombination is dominant. This may be reduced by decreasing the particle size, which then allows surface recombination to become dominant and since most of the electrons and holes are generated along the surface, recombination is faster than interfacial charge carrier processes [227]. Mesoporous, nanorod, and nanotube TiO_2 particles have shown high photocatalytic performance [228-231].

2.11.2. Metal-doped TiO_2 nanomaterial: second generation

Metal ion dopants in titania influences the charge carrier recombination rates and interfacial electron-transfer rates [232]. The reactivity of titania was enhanced according to the energy level of the dopant within the TiO_2 lattice, concentration, d electron configuration, electron donor concentration, light intensity and dopant distribution [20]. Iron doped nanocrystalline TiO_2 displayed higher photocatalytic activity with lower iron content than TiO_2 in treating waste water from paper mills. The iron doped titania was also more effective in photo electrocatalytic disinfection of *E. coli* than pure TiO_2 [233]. Not all doping improves catalytic action, however. In certain cases, pure TiO_2 is still more effective, as in vanadium doped TiO_2 had reduced photocatalytic activity on 4-chlorophenol compared to pure TiO_2 [234].

2.11.3. Non-metal doped TiO_2 nanomaterials: third generation

Non-metal doped TiO_2 is considered third generation photocatalysts. Many non-metal doped TiO_2 nanomaterials have been studied for their visible light photocatalytic activities [235-240]. These non-metal doped TiO_2 nanomaterials have shown an improved catalytic activity compared to pure TiO_2, especially in the visible region [204-207, 241-244]. N-doped TiO_2 showed a higher photocatalytic activity than pure TiO_2 in the visible region, and also displayed lower activity in the UV-region in the decomposition of methylene blue [112]. The photocatalytic activity was dependent on the nitrogen concentration in the visible region [245]. This concentration dependent activity is due to the band structure being different at varying concentrations [244]. Due to its structural properties, the valence band of TiO_2 is deep, and the photon generated holes are located on the surface of materials, making them easier to be harvested by free electrons from outside, thereby acting as an oxidising agent and making TiO_2 an excellent photocatalyst. Anatase is the preferred polymorph for photocatalysis due to higher electron mobility, low dielectric constant and low density [130, 246]. The increased photo activity is facilitated by a slightly higher Fermi level, a lower capacity to adsorb oxygen as well as a higher degree of hydroxylation [130]. Anatase is considered photochemically active due

to its charge carrier dynamics, chemical properties and photocatalytic degradation of organic compounds. It has an inherent surface band bending that forms spontaneously in a deep region with a steep potential [110]. This enables the surface hole to dominate because the spatial charge separation from the hole transfer toward the surface of the particle by strong upward band bending. In the rutile phase, the bulk recombination of electrons and holes occur, and only holes that are close to the surface are trapped and transferred to the surface [130].

2.12. Uses in heterogeneous photocatalysis

Photooxidation of organic compounds by dioxygen to break them down into water, carbon dioxide and HCl if they contain chlorine [247]. This reaction may occur with aromatic compounds, alcohols, carboxylic acids, chloroalkanes and alkanes. They can be achieved using TiO_2 alone or with cocatalysts. Titania is also useful in the photocatalysis of water into hydrogen and oxygen [247]. Most efforts are based on the optical properties of titania, which in the visible light region is normally transparent. By doping or sensitization, the optical sensitivity and activity of titania nanomaterials in their visible light region could be improved. Doping also allows for more selective properties in sensory devices, as in the case of Birkefeld *et al*. [163] who found the resistance of anatase to vary in the presence of CO and H_2, but when doped with 10 % alumina, it became selective to H_2.

2.13. References

1. Klemm D., Schmauder H-P., Heinze T., Biopolymers, Wiley online Library, 2005, 6, 46-7.
2. Klemm D., Phillip B., Heinze T., Heinze U., Wagenknecht W., Wiley, 1998, 21-3.
3. Witczak Z. J., Marcel Dekker, New York, 1996, 794-97.
4. Krassig H.A., Yverdon: Gordon Breach Science Publishers, 1993, 342-48.
5. Sarko A., Muggli R., Macromolecules, 1974, 7, 486-94.
6. Park S., O Baker J., Himmel E. M., Parilla P. A., Johnson D. K., biotechnology for fuels, 2010, 3, 10-13.
7. http://www.softschools.com/formulas/chemistry/cellulose_formula/464/, 06-09-2019, 11:05.
8. Hasan H. R., Sauodi M. H., Indian J. Chem. Technol., 2014, 9, 148-53.
9. Nur F. D., Phd Thesis, University of South Wales, 2012, 6.

10. Maepa C. E., Jayaramudu J., Okonkwo J. O., Ray S. S. Sadiku E. R., Ramontja J., Int. J. Polym. Anal. Charact., 2015, 20, 99-109.
11. https://www.shutterstock.com/search/maize+plant, 09/01/2018, 11:48. maize plant tassel image.
12. Beck B. B., An introduction to plant structure and morphology, Cambridge University Press, 2005, 59-64.
13. Mohamed M. A., Mutalib M. A., Hir Z. A. M., Zain M. F. M., Mohamad A. B., Minggu L. J., Awang N. A., Salleh W. N. W., Int. J. Biol. Macrom., 2017, 103, 1232-56.
14. C. E. Wyman, B. E. Dale, R. T. Elander, M. Holtzapple, M. R. Ladisch, and Y. Y. Lee, Bioresour. Technol., 2005, 96, 18, 1959–66.
15. Keegstra K., Talmadge K. W., Bauer W. D., Albersheim P., Plant Physiol., 1973, 51, 188-96.
16. Fry S. C., Plant Physiol., 1989, 75, 532-36.
17. Hayashi T., Annu. Rev. Plant Physiol. Plant Mol. Biol., 1989, 40, 139-68.
18. Cosgrove D. J., Plant Physiol., 2001, 125, 131-34.
19. https://www.thoughtco.com/cell-wall-373613, 09/01/2019, 11:50.
20. Cosgrove D. J., Annu. Rev. Plant. Physiol. Plant. Mol. Biol., 1999, 50, 391-417.
21. Giddings T. H. Jr. and Staehelin L. A., Planta, 1988, 173, 22-30.
22. Zhang X., Yang W., Blasiak W., Energy Fuels, 2011, 25, 4786-95.
23. Abdul Khalil H. P. S., Bhat A. H., Yusra A. F. I., Carbohydr. Polym., 2012, 87, 963-79.
24. de Morais Teixeira E., Corrêa A. C., Manzoli A., de Lima Leite F., de Oliveira C. R., Mattoso L.H.C., Cellulose, 2010, 17, 595-606.
25. Torlopov M. A., Udoratina E. V., Martakov I. S., Sitnikov P. A., Cellulose, 2017, 5, 2153-62.
26. de Souza Lima M.M., Borsali R., Macromol. Rapid Commun. 2004, 25, 771-87.
27. Sassi J. F., Chanzy H., Cellulose, 1995, 2, 111-27.
28. Jogunola O., Eta V., Hedenström M., Sundman O., Salmi T., Mikkola J. P, Carbohydr. Polym., 2016, 135, 341-8.
29. Zhijiang C., Chengwei H., Guang Y., Carbohydr. Polym., 2012, 87, 1073-80.
30. Huang Y., Zhu C., Yang J., Nie Y., Chen C., Sun D., Cellulose, 2014, 21, 1-30.
31. Lin S. P., Loira C. I., Catchmark J. M., Liu J. R., Demirci A., Cheng K. C., Cellulose, 2013, 20, 2191-219.
32. Algarra M., Vázquez M. I., Alonso B., Casado C. M., Casado J., Benavente J., Chem. Eng. J., 2014, 253, 472-7.

33. Mohamed M. A., Salleh W. N. W., Jaafar J., Ismail A. F., Abd Mutalib M. A., Jamil S. M., J. Appl. Polym. Sci., 2015, 132, 42684-9.
34. Aulin C., Netrval J., Wågberg L., Lindström T., Soft Matter., 2010, 6, 3298-305.
35. Shen X., Shamshina J.L., Berton P., Gurau G., Rogers R. D., Green Chem., 2016, 18, 53-75.
36. Kimura M., Shinohara Y., Takizawa J., Ren S., Sagisaka K., Lin Y., Hattori Y., Hinestroza J. P., Sci. Rep., 2015, 5, 16266-73.
37. Yang Q., Saito T., Berglund L. A., Isogai A., Nanoscale, 2015, 7, 17957-63.
38. Shrotri A., Kobayashi H., Fukuoka A., Acc. Che. Res., 2018, 51, 761-8.
39. Bergenstråhle M., Wohlert J., Himmel M. E., Brady J. W., Carbohydrate Research, 2010, 345, 2060-6.
40. Jiang Y., lawan E., Zhou W., Zhang M., Fernando G. F., Wang L., Yuan Z., Cellulose, 2019, 27, 3-7.
41. Spagnol C., Fragal E. H., Witt M. A., Follmann H. D. M., Silva R., Rubira A. F., Carbohydrate Polymers, 2018, 191, 25-34.
42. Varganici C., Rosu L., Mocanu (Paduraru) O. M., Rosu D., J. Photochem. Photobiol. A Chem., 2015, 297, 20-30.
43. Meyer K. H., Misch L., Ber., 1937, 70B, 272-4.
44. Gardner K. H., Blackwell J., Biopolymers, 1974, 13, 10-2.
45. Atalla R. H., Vanderhart D. L., Science, 223, 283-5.
46. Lin K.-F., Cheng H.-M., Hsu H.-C., Lin L.-J., Hsieh W.-F., Chem. Phys., 2005, ,409, 208-15.
47. Yamamoto H., Horii F., Macrom., 1993, 26, 1313-17.
48. Tutt M., Kikas T., Olt J., Agron. Res. Biosyst. Eng., 2012, 1, 269-76.
49. Bensah E. C., Mensah M., Int. J. Chem. Eng., 2013, 21, 1-22.
50. Ciolacu D., Ciolacu F., Popa V. I., Cellulose Chem. Technol., 2011, 45, 13-21.
51. Bali G., Meng X., Deneff J. I., Sun Q., Ragauskas A. J., ChemSusChem, 2015, 5, 275-9.
52. Millett M. A., Moore W. E., Saeman J. F., Ind. Eng. Chem., 1954, 7, 1493-97.
53. Hubbel C. A., Ragauskas A. J., Bioresource Technol., 2010, 101, 7410-15.
54. Candido R. G., Godoy G. G., Goncalves A. R., Eng. Tech., 2012, 61, 1-6.
55. Pingali S. V., Urban V. S., Heller W. T., Biomacromol., 2010, 11, 2329-35.
56. Chum H. L., Johnson D. K., Black S. K., Overend R. P., Appl. Biochem. Biotechnol., 1990, 24,1-14.
57. Talebnia F., Karakashev D., Angelidaki I., Bioresour. Techn., 2010, 101, 4744-53.

58. Lee J. W., Houtman C. J., Kim H. Y., Choi I. G., Jeffries T. W., Bioresour. Technol., 2011 102, 451-6.
59. Grahn, H. T., Singapore World Scientific Publishing Co. Pte, Ltd., 1999.
60. Lee J. W., Rodrigues R. C. L. B., Kim H. J., Choi, I. G., Jeffries T. W., Bioresour. Technol., 2010, 101, 4379-85.
61. Li X., Cai Z., Horn E., Winandy J. E., Holzforschung, 2011, 65, 737-41.
62. Sharma M., Kumar A., British Biotech. J., 2013, 3, 1-28.
63. Yang B., Wyman C. E., Biofuel Bioprod. and Biorefin., 2008, 2, 26-40.
64. Ju X., Engelhard M., and Zhang X., Bioresour. Technol., 2013,132, 137-45.
65. Zhang Y. H. P., Zhu Z., Rollin R., Sathitsuksanoh N., Cellulose Solvents: For Analysis, Shaping and Chemical Modification, 2010, 1033, 365-79.
66. Zhang J., Zhang B., Zhang J., Lin L., Liu S., Ouyang P., Biotech. Advances, 2010, 28, 613-9.
67. Yoo H. Y., Kim S. B., Choi H. S., Kim K., Park C., Kim S. W., Proceedings of the International Conference on Future Environment and Energy (IPCBEE '12), 2012, 28, 10-11.
68. Menon V., Rao M., Prog. Energ. Combust. Sci., 2012, 38, 522-50.
69. Hendriks A. T. W. M., Zeeman G., Bioresour. Technol., 2009, 100, 10-8.
70. Zhao Y., Wang Y., Zhu J. Y., Ragauskas A., Deng Y., Biotech Bioeng, 2008, 99, 1320-28.
71. Li Y., Ruan R., Chen P. L., Transactions of the American Society, 2004, 3, 821-5.
72. Pederson L. S., Kihlgren P., Nissen A. M., Munk M., Holm H. C., Choma P. P., Enzymatic bleach boosting of Kraft pulp: laboratory and mill scale experience. In: proceedings of tappi pulping conference Boston, M. A., U.S.A., November 1-5, Book 1, tappi Press Atlanta, 31.
73. Kumar R., Mago G., Balan V., Wyman C. E., Bioresou. Tech., 2009, 17, 3948–62.
74. Ioelovich M., Morag E., BioResources, 2012, 1, 1040–52.
75. Tao L., Aden A., Elander R. T., Bioresour. Technol., 2011, 102, 11105-14.
76. Falls M., Holtzapple M. T., Appl. Biochem. Biotech., 2011, 165, 506-22.
77. Rovio S., Kallioinen A., Tamminen T., Hakola M., Leskela M., Siika-ahoa M., BioResources, 2012, 7, 756-76.
78. Yang B., Wyman C. E, Biofuels, Bioproducts and Biorefining, 2008, 1, 26–40.
79. Saha B. C., Cotta M. A., , Biomass and Bioenergy, 2008, 10, 971–77.

80. Wyman C. E., Dale B. E., Elander R. T., Holtzapple M., Ladisch M. R., Lee Y. Y., Bioresour. Technol., 2005, 18, 1959–66.
81. Prado R., Erdocia X., Serrano L., Labidi J., Cellulose Chemistry and Technology, 2012, 46, 221–25.
82. Jermyn M. A., Isherwood F. A., Biochemical Journal, 1956, 64, 123-32.
83. Agbor V. B., Cicek N., Sparling R., Berlin A., Levin D. B., Biotechnology Advances, 2011, 6, 675–85.
84. Moon R. J., Martini A., Nairn J., Simonsen J., Youngblood J., Chem.Soc. Rev., 2011, 40, 3941-94.
85. Seiyama T., Kato A., Kiyoshi F., Masanori N., Anal. Chem., 1962, 34, 1502-3.
86. Cross C. F., Bevan E. J., J. Chem. Soc. Trans., 55, 199-213.
87. Snyder A., Bo Z., Moon R., Rochet J. C., Stanciu L., J. Colloid Interface Sci., 2013, 399, 92-8.
88. Li J. F., Xu Z. L., Yang H., Yu L. Y., Liu M., Appl. Surf. Sci. 2009, 255, 4725-32.
89. Abedini R., Mousavi M., Aminzadeh R., Chem. Ind. Chem. Eng. Q. 2012, 18, 385-98.
90. Boury B., Plumejeau S., Green Chem., 2015, 17, 72-88.
91. Mohamed M. A., Salleh W. N. W., Jaafar J., Mohd Hir Z. A., Rosmi M. S., AbdMutalib M., Ismail A. F., Tanemura M., Carbohydr. Polym., 2016, 146, 166-73.
92. Tian H., He J., Langmuir, 2016, 32, 12269-82.
93. Brinker C.J., Scherer G.W., Gulf Professional Publishing, Academic Press Inc, UK,1990, 25-30.
94. Zeng J., Liu S., Cai J., Zhang L., J. Phys. Chem. C, 2010, 114, 7806-11.
95. Bagheri S., Mohd Hir Z. A., Yousefi A. T., Abdul Hamid S. B., Microporous Mesoporous Mat., 2015, 218, 206-22.
96. Byrappa K., Yoshimura M., NoyesPublications/William Andrew Publishing, LLC, USA, 2001, 62-75.
97. Yoshimura M., Byrappa K., J. Mater. Sci., 2008, 43, 2085-103.
98. Somiya S., Roy R., Bull. Mater. Sci., 2000, 23, 453-60.
99. Ghanbari D., Salavati-Niasari M., Beshkar F., Amiri O., J. Mater. Sci. Mater.Electron., 2015, 26, 8358-66.
100. Bai H., Zan X., Juay J., Sun D. D., J. Memb. Sci., 2015, 475, 245-51.
101. Zhou Z., Peng X., Zhong L., Wu L., Cao X., Sun R.C., Carbohydr. Polym. 2016, 136, 322-8.

102. Kemell M., Pore V., Ritala M., Leskelä M., Linden M., J. Am. Chem. Soc., 2005, 127 14178-9.
103. Pore V., Rahtu A., Leskelä M., Ritala M., Sajavaara T., Keinonen J., Chem. Vap. Depos., 2004, 10, 143-8.
104. Sarin V., Pal U., Gopalan S., U.S. Department of Energy, USA, 2003, 54-56.
105. Winandy J. E., Krzysik A. M., Wood Fiber Sci., 2007, 39, 450-61.
106. Åkerholm M, Hinterstoisser B, Salmén L: Carbohydr Res., 2004, 339, 569-78.
107. Saracino G. A. A., Coqoqnini D., Silva D., Caprini A., Gelain F., Chem. Soc.Rev., 2013 42, 225-8.
108. Shi H., Barnard A.S., Snook I.K., J. Mater. Chem., 2012, 22, 18119-27.
109. Linganiso E. C., University of the Witwatersrand, 2014, 25-45.
110. Rasmussen J.W., Martinez E., Louka P., Wingett D.G., Expert Opin. Drug Deliv., 2010, 7, 1063-71.
111. Pokropivny V. V., Skorokhod V. V., Phisica E, 2008, 40, 2521-30.
112. Lin K.-F., Cheng H.-M., Hsu H.-C., Lin L.-J., Hsieh W.-F., Chem. Phys., 2005, ,409, 208-15.
113. Alivisatos A. P., Science, 1996, 271, 993-8.
114. Wang Y., Herron N., J. Phys. Chem., 1991, 95, 525-32.
115. Cao G., Singapore World Scientific Publishing Co. Pte, Ltd., 2004.
116. Liqiang J., Yichun Q., Baiqi W., Shudan L., Baojiang J., Libin Y., Wei F., Honggang F., Jaizhong S., Solar Energy Materials & Solar Cells, 2006, 90, 1773-85.
117. Feldmann C., Nanoscale, 2011, 3, 1947-8.
118. Akhtar M. S., Khan M. A., Jeon M. S., Yang O.-B., Electrochimica Acta., 2008, 53, 7869-74.
119. Cozzoli P. D., Kornowski A., Weller H., J. Am. Chem. Soc., 2003, 125, 14539-48.
120. Peng Z.A., Peng X., J. Am. Chem. Soc., 2001, 123, 183-4.
121. Nguyen V. N., Nguyen N. K. T., Nguyen P. H., Adv. Nat. Sci.: Nanosci.Nanotechnol., 2011, 2, 1-4.
122. Baruah S., Dutta J., Sci. Technol. Adv. Mater., 2009, 10, 1-19.
123. Djurisic A. B., Xi Y. Y., Hsu Y. F., Chan W. K., Recent Pat. Nanotechnol., 2007, 2, 121-5.
124. Rao C. N. R., Muller A., Cheetham A. K., WILEY-VCH Verlag GmnH & Co.KGaA 2004, 20-35.

125. Saelee K., Yingkamhaeng N., Nimchua T., Sukyai P., Extraction and characterization of cellulose from sugarcane bagasse by using environmentally friendly method, The 26th annual meeting of the Thai Society for Biotechnology and International Conference, 2014.

126. Luzi F., Fortnati E., Puglia D., Lavorgna M., Santulli C., Kenny J. M., Torre L., Industrial crops and Products, 2014, 56, 175-86.

127. Jeantelot G., King Abdullah University of Science and technology, 2014, 22-32.

128. Chen X., Mao S. S., Chem. Rev., 2007, 107, 7, 2891-2959.

129. Qian X., Qin D., Song Q., Bai Y., Li T., Tang X., Wang E., Dong S., Thin Solid Films 2001, 385, 152-66.

130. Bai J., Zhou B., Chem. Rev. 2014, 114, 10131−76.

131. Linsebigler A. L., Lu G., Yates J. T., Jr. Chem. Rev., 1995, 95, 735-40.

132. Wunderlich W., Oekermann T., Miao L., J. Ceram. Process. Res., 2004, 5, 343-7.

133. Thompson T. L., Yates J. T., Chem. Rev., 2006, 106, 4428-34.

134. Diebold U., Surf. Sci. Rep., 2003, 48, 53-61.

135. Hu Y., Tsai H. L., Huang C. L., Mater. Sci. Eng., A, 2003, 344, 209-15.

136. Pimentel A., Nunes D., Pereira S., Martins R., Fortunato E., mechanisms and applications, 2016, 81-100.

137. Li C-Z., Chueh C-C., Yip H-L., O-Malley K. M., Chen W-C., Jen A. K-Y., J. Mater. Chem., 2012, 22, 23906-12.

138. Arrouvel C., Digne M., Breysse M., Toulhoat H., Raybaud P., J. Catal., 2004, 222, 152–66

139. Lazzeri M., Vittadini A., Selloni A., Phys. Rev., 2002, B 65, 119901-11.

140. Liu X., Cheng S., Liu H., Hu S., Zhang D., Ning H., Sensors, 2012, 12, 9635-65.

141. Hwu Y., Yao Y. D., Cheng N. F., Tung C. Y., Lin H. M., Nanostruct. Mater., 1997, 9, 355-72.

142. Serpone N., Lawless D., Khairutdinov R., Pelizzetti E., J. Phys.Chem., 1995, 99, 16655-80.

143. Luzi F., Fortnati E., Puglia D., Lavorgna M., Santulli C., Kenny J. M., Torre L., Industrial crops and Products, 2014, 56, 175-86.

144. Zhang H., Banfield J. F. J., Mater. Chem., 1998, 8, 2073-80.

145. Zhang H., Banfield J. F., J. Phys. Chem. B, 2000, 104, 3481-95.
146. Szczepankiewicz S. H., Moss J. A., Hoffmann M. R., J. Phys. Chem. B, 2002, 106, 7654-8.
147. Szczepankiewicz S. H., Colussi A. J., Hoffmann M. R., J. Phys.Chem. B, 2000, 104, 9842-65.
148. Howe R. F., Gra¨tzel M., J. Phys. Chem., 1985, 89, 4495-501.
149. Howe R. F., Gra¨tzel M., J. Phys. Chem., 1987, 91, 3906-11.
150. Hurum D. C., Agrios A. G., Crist S. E., Gray K. A., Rajh T., Thurnauer M. C., J. Electron. Spectrosc. Relat. Phenom., 2006, 150,155-62.
151. Hurum D. C., Gray K. A., Rajh T., Thurnauer M. C., J. Phys.Chem. B ,2005, 109, 977-85.
152. Berger T., Sterrer M., Diwald O., Knoezinger E., Panayotov D., Thompson T. L., Yates J. T. Jr., J. Phys. Chem. B, 2005, 109, 6061-74.
153. Li G. L., Wang G. H., Nanostruct. Mater., 1999, 11, 663-7.
154. Varghese O. K., Gong D., Paulose M., Ong K. G., Dickey E. C., Grimes C. A., Adv. Mater., 2003, 15, 624-35.
155. Mor G. K., Varghese O. K., Paulose M., Shankar K., Grimes C. A., Sol. Energy Mater. Sol. Cells, 2006, 90, 2011-75.
156. Grimes C. A., J. Mater. Chem. 2007, 17, 1451-7.
157. Mor G. K., Shankar K. Paulose M., Varghese O. K., Grimes C. A., Nano Lett., 2006, 6, 215-8.
158. Mor G. K., Shankar K., Paulose M., Varghese O. K., Grimes C. A., Nano Lett., 2005, 5, 191-5.
159. Xu C., Gao D., J. Phys. Chem. C, 2012, 116, 7236-41.
160. Qiu J. J., Yu W. D., Gao X. D., Li X. M., Nanotechnology, 2006,17, 4695-72.
161. Yu Y., Yin X., Kvit A., Wang X., Nano Lett. 2014, 14, 2528-35.
162. Li Z., Yao C., Yu Y., Cai Z., Wang, X., Adv. Mater. 2014, 26, 2262-7.
163. Birkefeld L. D., Azad A. M., Akbar S. A., J. Am. Ceram. Soc., 1992, 75, 2964-8.
164. Li X. L., Peng Q., Yi J. X., Wang X., Li Y. D., Chem.s Eur. J., 2006, 12, 2383-7.
165. Xu J., Ge J. P., Li Y. D., J. Phys. Chem. B, 2006, 110, 2497-501.
166. Wu J. M., Shih H. C., Wu W. T., Chem. Phys. Lett., 2005, 413, 490-5.
167. Wu J. M., Shih H. C., Wu W. T., Tseng Y. K., Chen I. C., J. Cryst. Growth, 2005, 281, 384-8.

168. Wyman C. E., Dale B. E., Elander R. T., Holtzapple M., Ladisch M. R., Lee Y. Y., Bioresour. Technol., 2005, 18, 1959–66.
169. Prado R., Erdocia X., Serrano L., Labidi J., Cellulose Chemistry and Technology, 2012, 46, 221–25.
170. Bessekhouad Y., Robert D., Weber J. V. J., Photochem. Photobiol. A, 2003, 157, 47-53.
171. Saracino G. A. A., Coqoqnini D., Silva D., Caprini A., Gelain F., Chem. Soc.Rev., 2013 42, 225-8.
172. Shi H., Barnard A.S., Snook I.K., J. Mater. Chem., 2012, 22, 18119-27.
173. Sugimoto T., Adv. Colloid Interface Sci., 1987, 28, 65-72.
174. Chemseddine A., Moritz T., Eur. J. Inorg. Chem., 1999, 235.
175. Moritz T., Reiss J., Diesner K., Su D., Chemseddine A., J. Phys.Chem. B, 1997, 101, 8052-6.
176. Sugimoto T., Okada K., Itoh, H., J. Colloid Interface Sci., 1997,193, 140-7.
177. Zhang H., Banfield J. F., Chem. Mater., 2002, 14, 4145-52.
178. Vorkapic D., Matsoukas T., J. Colloid Interface Sci., 1999, 214, 283.
179. Sugimoto T., Zhou X., Muramatsu A., J. Colloid Interface Sci., 2003,259, 53-60.
180. Rasmussen J.W., Martinez E., Louka P., Wingett D.G., Expert Opin. Drug Deliv., 2010, 7, 1063-71.
181. Zhang H., Banfield J. F., J. Mater. Chem., 1998, 8, 2073-77.
182. Zhang H., Banfield J. F., J. Phys. Chem. B, 2000, 104, 3481-5.
183. Zhang H., Finnegan M., Banfield J. F., Nano Lett. 2001, 1, 81-8.
184. Zhang H., Banfield J. F., Chem. Mater., 2002, 14, 4145-52.
185. Zhang H., Banfield J. F., Chem. Mater., 2005, 17, 3421-6.
186. Miao L., Tanemura S., Toh S., Kaneko K., Tanemura M., J. Cryst. Growth, 2004, 264, 246-50.
187. Miao L., Tanemura S., Toh S., Kaneko K., Tanemura M., Appl.Surf. Sci., 2004, 238, 175-82.
188. Jung J. H., Kobayashi H., van Bommel K. J. C., Shinkai S., Shimizu T., Chem. Mater., 2002, 14, 1445-50.
189. Jung J. H., Shimizu T., Shinkai S., J. Mater. Chem., 2005, 15, 3979-85.
190. Thompson T. L., Yates J. T., Chem. Rev., 2006, 106, 4428-34.
191. Diebold U., Surf. Sci. Rep., 2003, 48, 53-61.
192. Hu Y., Tsai H. L., Huang C. L., Mater. Sci. Eng., A, 2003, 344, 209-15.

193. Berger T., Sterre M., Diwald O., Knoezinger E., Panayotov D.,Thompson T. L., Yates J. T. Jr., J. Phys. Chem. B, 2005, 109, 6061-74.
194. Varghese O. K., Gong D., Paulose M., Ong K. G., Dickey E. C., Grimes C. A., Adv. Mater., 2003, 15, 624-35.
195. Mor G. K., Varghese O. K., Paulose M., Shankar K., Grimes C. A., Sol. Energy Mater. Sol. Cells, 2006, 90, 2011-75.
196. Yang J., Mei S., Ferreira J. M. F., J. Eur. Ceram. Soc., 2003, 24,335-40.
197. Yang J., Mei S., Ferreira J. M. F., Mater. Sci. Forum 2004, 455-456, 556-65.
198. Wu J. M., J. Cryst. Growth, 2004, 269, 347-51.
199. Lei Y., Zhang L. D., Fan J. C., Chem. Phys. Lett., 2001, 338, 231-5.
200. Blesic M. D., Saponjic Z. V., Nedeljkovic J. M., Uskokovic D. P., Mater. Lett., 2002, 54, 298-303.
201. Guo W., Lin Z., Wang X., Song G., Microelectron. Eng., 2003, 66, 95-99.
202. Linsebigler A. L., Lu G., Yates J. T. Jr., Chem. Rev., 1995, 95, 735-41.
203. Anpo M., Shima T., Kodama S., Kubokawa Y., J. Phys. Chem. 1987, 91, 4305-9.
204. Wu J. M., Hayakawa S., Tsuru K., Osaka A., Scripta Mater., 2002, 46, 705-9.
205. Wu J. M., Zhang T. W., J. Photochem. Photobiol., 2004, 162,171-8.
206. Chen X., Lou Y., Dayal S., Qiu X., Krolicki R., Burda C., Zhao C., Becker J., Nanosci. Nanotechnol., 2005, 5, 1408-18.
207. Burda C., Lou Y., Chen X., Samia A. C. S., Stout J., Gole, J. L., Nano Lett., 2003, 3, 1049-55.
208. Chen X., Burda C., J. Phys. Chem. B, 2004, 108, 15446-55.
209. Chen X., Lou Y., Samia, A. C. S., Burda C., Gole J. L., Adv. Funct. Mater., 2005, 15, 41-8.
210. Gu Z. Z., Fujishima A., Sato O., Angew. Chem. Int. Ed., 2002, 41, 2067-73.
211. Sirghi L., Aoki T., Hatanaka Y., Surf. Rev. Lett., 2003, 10, 345-9.
212. Takata Y., Hidaka S., Cao J. M., Tanaka K., Masuda M., Ito T., Watanabe T., Shimohigoshi M., Therm. Sci. Eng., 2000, 8, 33-8.
213. Takata Y., Hidaka S., Masuda M., Ito T., Int. J. Energy Res., 2003, 27, 111-7.
214. Gra¨tzel M., Prog. PhotoVolt., 2000, 8, 171-80.
215. Zhang H., Banfield J. F., Chem. Mater., 2002, 14, 4145-53.
216. Zhang H., Banfield J. F., Chem. Mater. 2005, 17, 342130.
217. Znaidi L., Seraphimova R., Bocquet J. F., Colbeau-Justin C., Pommier C., Mater. Res. Bull., 2001, 36, 811-7.

218. Oskam G., Nellore A., Penn R. L., Searson P. C., J. Phys. Chem.B, 2003, 107, 1734-8.
219. Sugimoto T., Adv. Colloid Interface Sci., 1987, 28, 65-72.
220. Sugimoto T., Okada K., Itoh, H., J. Colloid Interface Sci., 1997,193, 140-7.
221. Sugimoto T., Zhou X., J. Colloid Interface Sci., 2002, 252, 347-55.
222. Sugimoto T., Zhou X., Muramatsu A., J. Colloid Interface Sci., 2002,252-339.
223. Boujday S., Wunsch F., Portes P., Bocquet J. F., Colbeau-Justin C., Sol. Energy Mater. Sol. Cells, 2004, 83, 421-30.
224. Choi W., Termin A., Hoffmann M. R., J. Phys. Chem., 1994, 98, 13669-74.
225. Choi W., Termin A., Hoffmann M. R., Angew. Chem., 1994, 106, 1148-55.
226. Thevenet F., Guaitella O., Herrmann J. M., Rousseau A., Guillard C., Appl. Catal. B, 2005, 61, 58-64.
227. Zhu J., Zhang J., Chen F., Iino K., Anpo M., Top. Catal., 2005, 35, 261-6.
228. Kim K. D., Kim H. T., Powder Technol., 2001, 119, 164-9.
229. Niederberger M., Bartl M. H., Stucky G. D., Chem. Mater., 2002,14, 4364-9.
230. Parala H., Devi A., Bhakta R., Fischer R. A., J. Mater. Chem., 2002, 12, 1625-31.
231. Tang J., Redl F., Zhu Y., Siegrist T., Brus L. E., Steigerwald M. L., Nano Lett., 2005, 5, 543-7.
232. Choi W., Termin A., Hoffmann M. R., Angew. Chem., 1994, 106, 1148-55.
233. Joo J., Kwon S. G., Yu T., Cho M., Lee J., Yoon J., Hyeon T., J. Phys. Chem. B, 2005, 109, 15297-301.
234. Zhang Z. Wang C. C. Zakaria R. Ying J. Y. J. Phys. Chem. B1998, 102, 10871-6.
235. Beyers E., Cool P., Vansant E. F., J. Phys. Chem. B, 2005, 109, 10081-7.
236. Yu J. C., Zhang L., Yu J., New J. Chem., 2002, 26, 416-9.
237. Wu J. M., Zhang T. W., Zeng Y. W., Hayakawa S., Tsuru K., Osaka A., Langmuir, 2005, 21, 6995-7011.
238. Gandhe A. R., Naik S. P., Fernandes J. B., Microporous Mesoporous Mater., 2005, 87, 103-8.
239. Irie H., Washizuka S., Watanabe Y., Kako T., Hashimoto K., J. Electrochem. Soc., 2005, 152, 351-6.
240. Morawski A., Janus W. M., Pol. J. Chem. Technol., 2005, 7, 81-9.
241. Yang M. C., Yang, T. S., Wong, M. S., Thin Solid Films, 2004, 469-470, 1-5.
242. Yang S., Gao L., J. Am. Ceram. Soc., 2004, 87, 1803-11.
243. Wei, H., Wu Y., Lun N., Zhao F., J. Mater. Sci., 2004, 39, 1305-15.

244. Sano, T., Negishi N., Koike K., Takeuchi K., Matsuzawa S., J. Mater. Chem., 2004, 14, 380-6.
245. Hidaka H., Koike T., Kurihara T., Serpone N., New J. Chem., 2004, 28, 1100-9.
246. Asahi R., Morikawa T., Ohwaki T., Aoki K., Taga Y., Science, 2001, 293, 269-75.
247. Irie H., Watanabe Y., Hashimoto K., J. Phys. Chem. B, 2003, 107, 5483-9.

CHAPTER 3

Methodology

3.1. Chemicals

Titanium (IV) butoxide ($Ti(OBu)_4$ Sigma Aldrich), sodium hydroxide (NaOH, uniLAB), absolute ethanol (99%, MK chemicals), nitric acid (55%, ACE chemicals), sulphuric acid (98%, ACE chemicals), methyl orange in xylene cyanol ($C_{39}H_{41}N_5Na_2O_{10}S_3$, ACE chemicals) and maize tassels (MT, obtained from a garden in Kingsway, Benoni), distilled water (dH_2O).

3.2 Experimental procedure

3.2.1. Synthesis of anatase-TiO_2 nanoparticles

Synthesis of TiO_2 nanoparticles was achieved using a simple sol-gel procedure. A 10 mL volume of $Ti(OBu)_4$ was ultrasonically mixed with 10 mL anhydrous ethanol as solvent in atmospheric conditions to give a clear solution. A 5 mL volume of water was slowly added, dropwise into the mixture to initiate the hydrolysis reaction. The resulting mixture turned into a white transparent gel upon addition of water, which was stirred for 2 h at room temperature, followed by ageing for 24 h at ambient temperature. The product was filtered and washed several times with deionized water and ethanol followed by drying at 100 °C for 12 h to form a precursor. Calcination of the precursor at 450 °C for 2 h in air resulted in the formation of anatase TiO_2 nanoparticles [1].

3.2.2. Extraction of cellulose from maize tassel

Maize tassels (MT), Figure 3.1 A, that form at the top of the stems of male maize plants were used for extraction of cellulose [2]. They were soaked in water for one day to remove dirt. Next, the separated maize tassels were thoroughly washed with tap water, followed by distilled water, and then dried in the sun for one week. Thereafter, the maize tassels were kept in an oven for 24 h at a temperature of 110 °C to remove any residual moisture. The cleaned MT was stirred in 700 mL of nitric acid (1 M) at room temperature for 24 h and then washed several times with distilled water. The wet material was then dried in an oven at 100 °C for 24 h. To purify the cellulose by removing lignin, 500 mL of 1 M NaOH solution was added to the dried material, Figure 3.1 B. The resulting mixture was stirred for 24 h at room temperature and the residue was subsequently filtered under vacuum. Equal amounts of the residue, Figure 3.1 C, were separated and added to various concentrations of NaOH (2 M to 12 M) to determine which

was best for cellulose extraction. The product residue was then added to distilled water and titrated at room temperature using sulfuric acid (5.0 M) under continuous stirring until constant pH in the range of 5-6 was reached [2]. The resulting suspension material was then separated again by vacuum filtration and washed with distilled water, Figure 3.1 D. Figure 3.1 shows the starting material and the products after each step of synthesis.

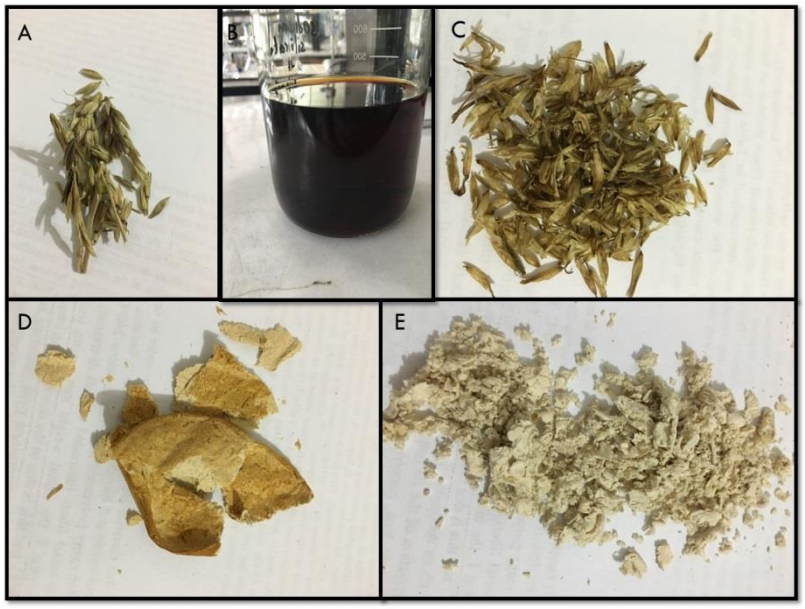

Figure 3.1: Shows maize tassel and the products thereof. In a clockwise direction, (A) maize tassel untreated, (B) lignocellulosic solution after pre-treatment and 6M NaOH treatment, (C) product of NaOH treatment, (D) product after filtration and drying, (E) product after grinding.

3.2.3. Methodology for the synthesis of TiO_2/cellulose nanocomposite

Various mass ratios of TiO_2/cellulose were used as shown in Table 3.1 for the preparation of the composites to give a total mass of 1 gram (100 %) per sample. Cellulose was vigorously stirred in 25 mL dH_2O under reflux at 80 °C for two hours in a round bottom flask. The TiO_2 was sonicated in 25 mL dH_2O and then added to the cellulose solution. Then the combined solution was then stirred vigorously under reflux for 24 h at 80 °C. The water was evaporated through heating the solution at 80 °C for 2 hours and the product was then left in open air until dry.

Table 3.1: TiO_2/cellulose nanocomposites, mass (g) and % yield

Name	Cellulose mass (g)	% cellulose	TiO_2 mass (g)	% TiO_2	% yield
CT(A)	0.9	90	0.1	10	97
CT(B)	0.8	80	0.2	20	98
CT(C)	0.6	60	0.4	40	99
CT(D)	0.4	40	0.6	60	96
CT(E)	0.2	20	0.8	80	97
CT(F)	0.05	5	0.95	95	98

$$\frac{composite\ mass\ (g)}{mass\ of\ cellulose\ (g)+mass\ of\ TiO_2(g)} * 100 = \%\ yield \qquad \text{Equation 3.1}$$

3.2.4. Photocatalytic degradation of methyl orange in water

For adsorption studies, a 50 mL, 5 ppm solution of methyl orange in xylene cyanol was stirred in the dark. To this solution, 10 mg of each sample of composite TiO_2/cellulose was added and stirred. 3 mL Aliquots of this solution were taken every 15 min from addition of catalyst. The aliquots were then filtered using 0.45 µm cellulose filters attached to a syringe. These aliquots were then analysed by UV-Vis spectroscopy. Once the adsorption time was determined, the same procedure as adsorption was then used for photocatalysis. The 50 mL of methyl orange dye and 10 mg composite were vigorously stirred in the dark for 5 min to ensure a homogenous solution and maximum adsorption of catalyst to dye. This was then placed under the solar simulator at 800 W. Then, 3 mL aliquots were taken every 15 min after initiation of reaction. These aliquots were filtered using 0.45 µm cellulose filters attached to a syringe. The concentration of the aliquots was measured using a UV-Vis spectrometer. The efficiency of the photodegradation was determined using Eq. 1:

$$\eta = \frac{C_o - C_t}{C_o} * 100\% \qquad \text{Equation 3.2}$$

Where η is the photocatalytic efficiency, C_t is the concentration after time t and C_o is the initial concentration. Figure 3.2 shows the experimental setup for photodegradation of methyl orange under a solar simulator.

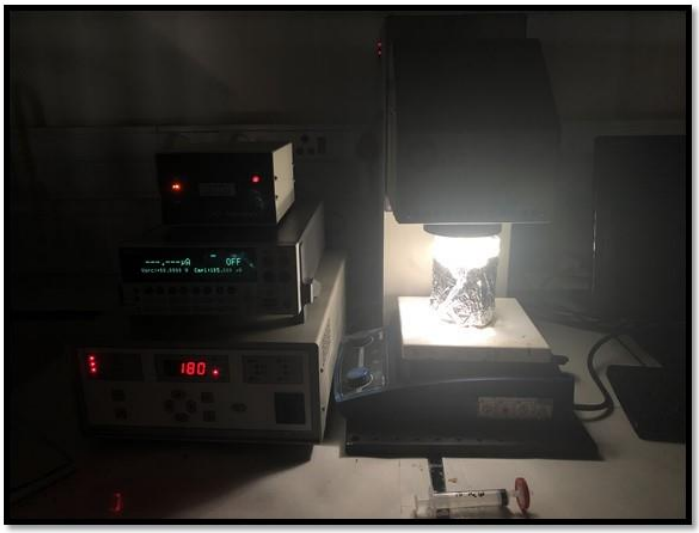

Figure 3.2: Image showing solar simulator and photocatalysis setup.

3.3. Characterization techniques

3.3.1. Raman spectrometry

Raman spectroscopy was done on the Bruker Infinity 1 spectrometer fitted with a 50x objective lens for imaging shown in Figure 3.3. The excitation wavelength used for all samples was 514 nm and the spectral data was evaluated using OPUS 7.1 software. Raman spectroscopy was used to probe the quality and phase of the synthesised TiO_2.

Figure 3.3: Image of the Raman spectrometer.

3.3.2. UV-Vis spectroscopy

The UV-Vis absorption characteristics were measured with the Varian Cary Eclipse (Cary 50) UV-Vis absorption spectrophotometer shown in Figure 3.4. UV-Vis spectrometry was used to determine the identity and concentration of TiO_2 and methyl orange [3]. The degradation of methyl orange was also investigated by monitoring the concentration of each aliquot taken. From the excitation wavelength, the band gap of TiO_2 was determined using the equation $E = hc/\lambda$, where h is planks constant, c is the speed of light and λ is the wavelength (nm). For TiO_2 analysis, 2 mg of TiO_2 was dispersed in 4 mL of ethanol under sonication for five minutes and then transferred to a 1 cm^2 UV quartz cuvette.

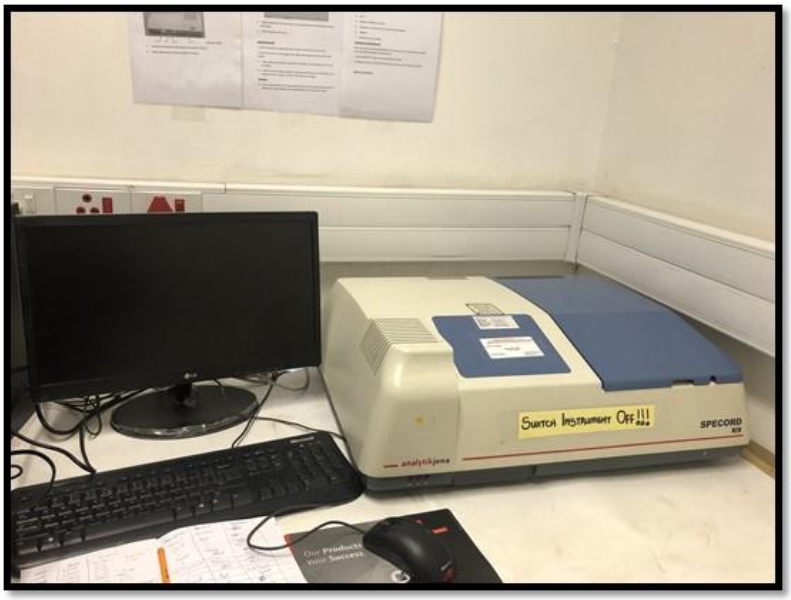

Figure 3.4: Image of the UV-Vis spectrophotometer.

3.3.3. Photoluminescence (PL) spectroscopy

The PL spectrometer was used to determine the electronic structure of TiO_2. The analysis was carried out on a Specord 30 using CARY software (Figure 3.5). For the analysis, 2 mg of sample was sonicated for 30 minutes in dH_2O to obtain a homogenous solution, which was then added to a quartz cuvette (1 cm^2) and analysed at an excitation wavelength of 320 nm. Background effects were minimised by running a blank before sample analysis. The slit angle for all analysis was 5 nm.

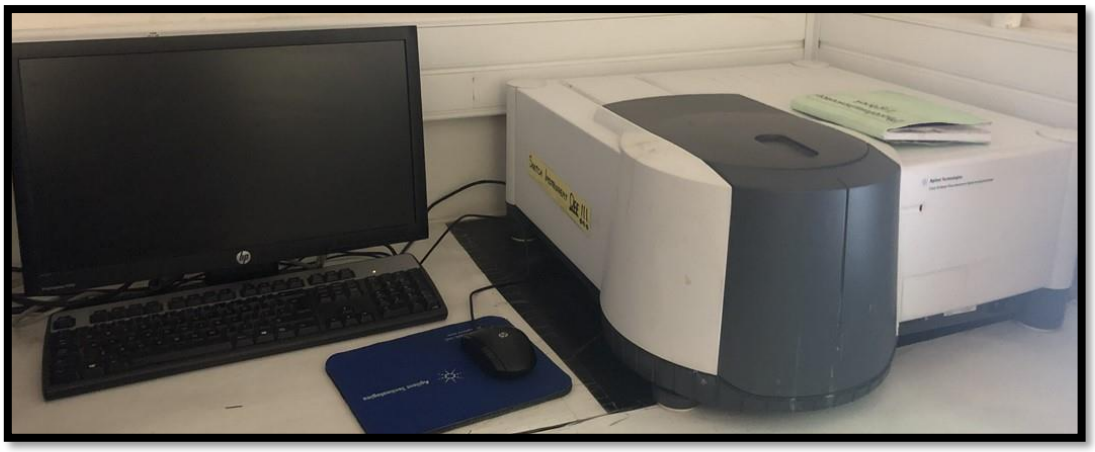

Figure 3.5: Image of PL spectrophotometer.

3.3.4. Solar simulation

Solar simulation was carried out under an Oriel Sol2A at 180 Watts/1 Sun where 1 Sun = 1 kW m^{-2} shown in Figure 3.6. 50 mL of methyl orange and 10 mg of catalyst were vigorously stirred under the solar simulator at 800 W for 90 minutes. The simulator is designed to imitate solar radiation, which consists of a high-powered lamp that radiates visible, UV and infrared wavelengths. The solar simulator was used to initiate the breakdown of methyl orange mixed with catalyst.

Figure 3.6: Image of the Oriel Solar simulator.

3.3.5. X-ray diffraction spectrometry

X-ray powder diffraction (XRD) was done on the Bruker MeasSrv (D2-205530)/D2205530 diffractometer using CuKα radiation (λ = 1.5406 Å) at 30 kV/10 mA shown in Figure 3.7. X-ray powder diffraction (XRD) is a rapid analytical technique primarily used for phase identification of a crystalline material (e.g. minerals, inorganic compounds) and can provide information on unit cell dimensions. The crystallinities of untreated and treated maize tassel fibres were examined by using the wide-angle X-ray diffraction (WAXD) technique, with CuKα radiation (k ¼ 1.54 A˚), with a computerized data acquisition facility and analytical tools. The X-ray source was operated at a voltage of 30 kV and a filament current of 10 mA. All samples were scanned in the 2θ range between 10° and 90°, at a rate of 5°/min in order to obtain an acceptable diffraction pattern.

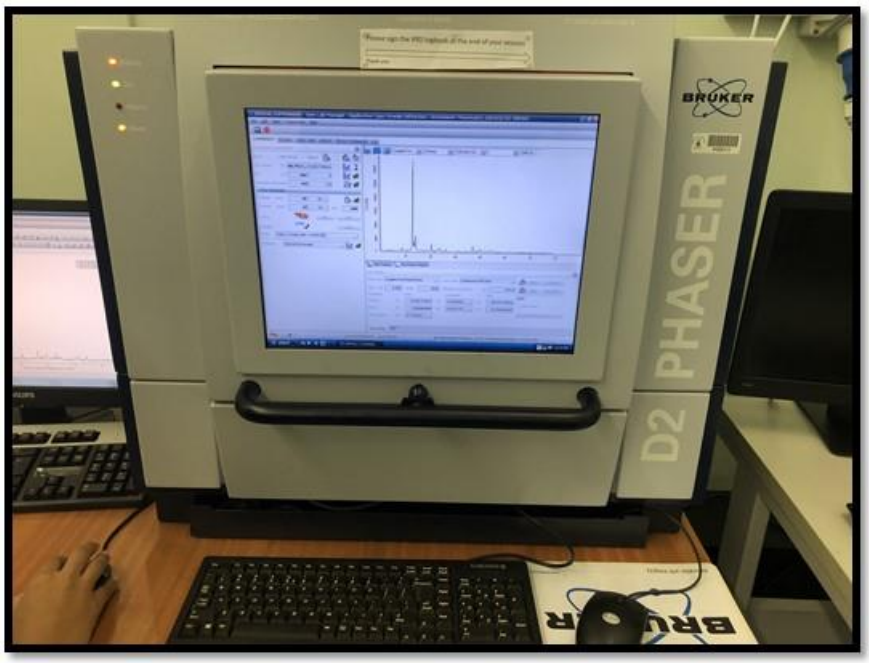

Figure 3.7: Image of the Bruker D2 XRD spectrometer.

3.3.6. Fourier Transform Infrared (FT-IR) spectroscopy

FTIR is a means of identifying unknown samples by the absorption of functional groups. Fourier Transform Infrared (FT-IR) spectroscopy was performed on a Bruker Tensor 27 spectrometer, Figure 3.8, which examines the structure of maize tassel fibre obtained after alkali treatment as well as TiO_2 and composite (CT). The FT-IR spectra of the samples were obtained in the wavelength range of 4500–400 cm^{-1}. A total of 32 scans were added to achieve an acceptable signal-to-noise ratio. In all cases, spectra resolution was maintained at 4 cm^{-1}.

This was done by adding a dry, crushed sample onto the KBr coated sample holder where the sample molecules selectively absorb radiation at specific wavelengths.

Figure 3.8: Image of the Bruker FTIR spectrophotometer.

3.3.7. Scanning electron microscopy (SEM)

Scanning electron microscopy and energy dispersive spectroscopy (EDS) was performed on the FEI Nova Nanolab 600 microscope, Figure 3.9. The only sample preparation required was that the material be crushed and coated with gold and palladium to inhibit charging, reduce thermal damage and enhance the secondary electron signal for topographic analysis. The sample was coated after being attached to carbon tape that was attached to the sample holder.

For the elemental composition analysis, Energy-Dispersive X-ray (EDX) spectroscopy connected to the FEI Nova Nano lab 600 SEM was used. The X-rays were captured using the INCA Microanalysis Suit version 4.08 package software. A spot size of approximately 40 µm was isolated to ensure the sample was free from dirt and debris for elemental analysis.

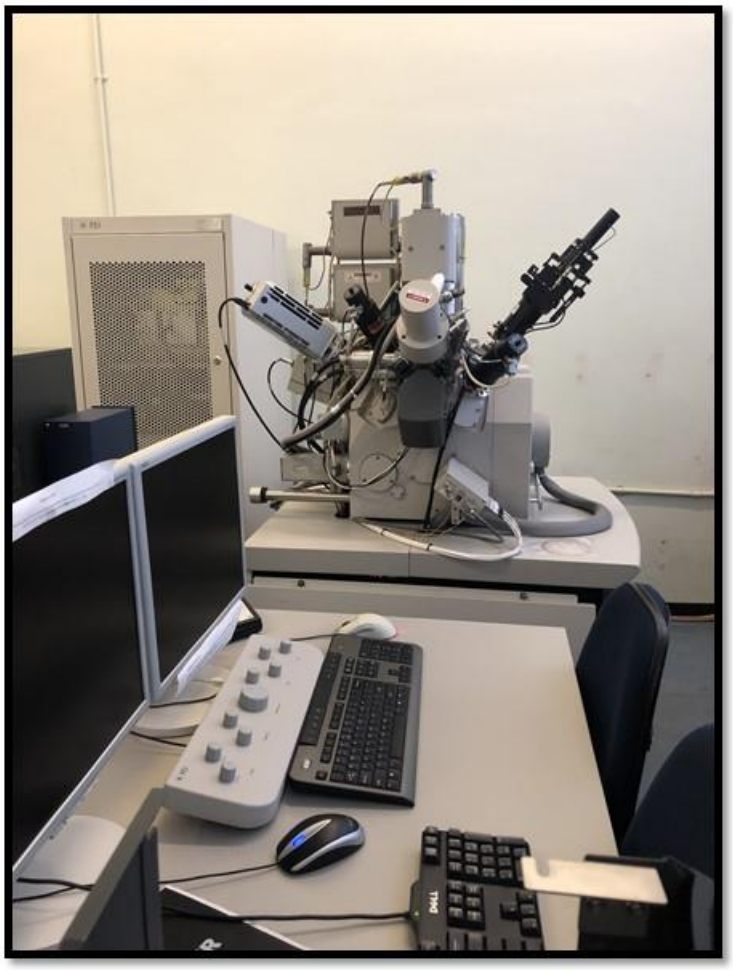

Figure 3.9: Image of the FEI Nova Nanolab 600 FEG-SEM/FIB scanning electron microscope.

3.3.8. Transmission electron microscopy (TEM)

Transmission electron microscopy (TEM) was done on the FEI Technai T12 microscope, Figure 3.10, with an accelerating voltage of 120 kV. Transmission Electron Microscopy (TEM) was used to determine morphological features such as size, diameter, length and arrangement of particles. TEM produces images using electron transmission, making beam alignment and sample preparation important. The samples were prepared by sonicating in ethanol to disperse the samples. A drop of the solution was then added on to an SPI-carbon coated copper grid and dried in air before inserting into the microscope. After insertion into the microscope, the beam was aligned, and sample images were taken. The average size of material was determined using image J software.

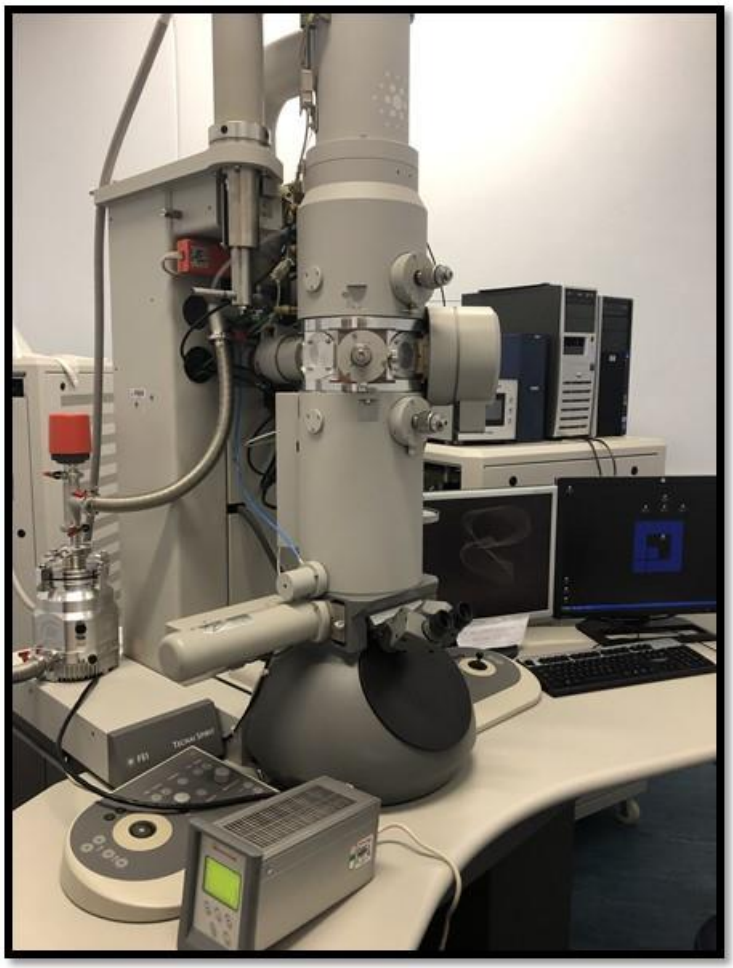

Figure 3.10: Image of the FEI TECNAI T12 transmission electron microscope.

3.3.9. Thermogravimetric analysis

Thermogravimetric analysis was done on a Perkin Elmer STA 4000 analyzer shown in Figure 3.11. This was used to determine the sample composition, thermal stability and purity of the samples. The sample mass (10 mg) and the flow rate (10 mL/min) were constant in all analyses to minimize the instrumental error. The sample was transferred to a ceramic pot supported on an analytical balance within the instruments furnace where the temperature was increased to 900 °C at a rate of 10 °C/min in a controlled environment. The TGA profile was accompanied with the derivative curve (DTG) to determine the oxidation temperature.

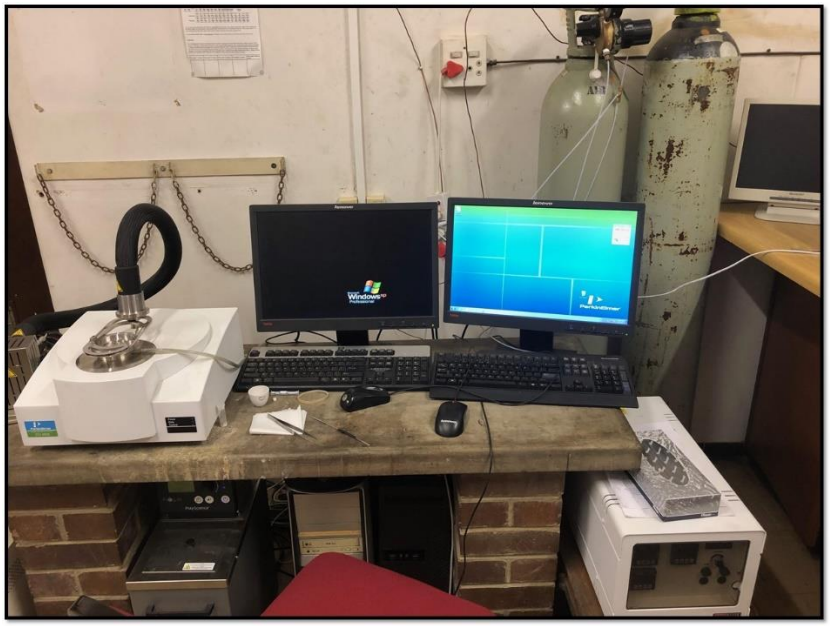

Figure 3.11: Image of the TGA-MS analyser.

3.4. References

1. Yang H., Zhang K., Shi R., Li X., Dong X., Yu Y., J. Alloy. Compd., 2006, 413, 302-6.
2. Hasan H. R., Sauodi M. H., CTAIJ, 2014, 9, 148-53.
3. Mathebula X., Photocatalytic degradation of methyl violet in water using TiO_2/cellulose-N-MWCNTs, Dissertation, The University of the Witwatersrand, 2018, 100-11.

CHAPTER 4

Extraction and characterization of cellulose from maize tassels: the effect of concentration and time

4.1. Introduction

Agricultural residue is a large segment of the global waste problem. The large volume of accumulated biomass waste threatens surface and ground water due to the storage conditions. Recycling this biomass may reduce waste disposed in landfills. The farming industry in South Africa is also at risk, after harvest; the remaining biomass is either left on the land or used for energy. Many countries use ~ 40% of maize stalk residue and the remaining crop residue is wasted [1]. There are many reports on using agricultural waste as a biofuel [2]; however, information on the use of maize as a cellulose source is limited [3]. Using crop biomass waste can also increase the business opportunities available to these countries [3]. There is a need to develop renewable material for industrial chemistry, especially in replacing oil. Plant biomass is a promising substitute and can be considered as a cheaper, less polluting raw material with economic value. The heterogeneity and chemical complexity of plant biomass provide raw materials for end products such as energy, food, chemical, pharmaceutical and materials. There are twelve principles of green chemistry [4]. The purpose is to consider reducing waste, atomic and energy conservation, as well as the use of renewable raw materials, which is of great importance to large biomass producing countries such as Brazil [4]. This biomass is an abundant and cheap feed stock for transformation processes in chemistry. This opens new possibilities to business and wealth generation, as well as to promote the impact on sustainability. With plant biomass, it is a means of using renewable raw materials as one of the principles of green chemistry. Markets that may benefit from biomass include fuels and energy, pharmaceuticals, cosmetics and hygiene [4]. These principles of green chemistry are not always easy to apply, however the appropriate choice on the basis of biomass type, process characteristics, and products need to be applied [4].

It is estimated that the yearly biomass production is 1.5 trillion tons, which makes this resource inexhaustible for environmentally friendly materials [5, 6]. These cellulose derivatives are used for coatings, laminates, optical films, pharmaceuticals, foods, and textiles [5, 6]. The advantages include biocompatibility and chirality for the immobilization of proteins and

antibodies as well as the separation of enantiomeric molecules and the formation of cellulose composites with synthetic polymers and biopolymers [6]. In this project, maize tassel has been utilized, which forms the top part of the male plant of maize. The tassel has a variety of colours and is considered as waste after the fertilization process has occurred. This tassel then forms part of the plant that remains after harvest and is considered waste. This waste is either burned, creating air pollution or piled to decay on farms.

Biomass requires a pretreatment step. The aim of the pretreatment is to disrupt the physical structure of the biomass by breaking the lignin barrier, disrupting the cellulose crystallinity and remove the non-cellulosic components to increase cellulose accessibility [7]. Alkali treatment with lime ($Ca(OH)_2$) or ammonia under high pressure is also effective in removing lignin [6, 7]. For the study on *Populus* [6, 7], it was found that alkali treatment changed the cellulose degree of polymerization, and crystallinity. The crystallinity was reduced, however at 60 minutes, there was no significant change in crystallinity. Bali *et al.* [7] also showed that NaOH was the most effective alkaline pretreatment method for accessing cellulose from biomass. The objective of this section was to extract cellulose from maize tassel using alkali treatment. The aim was to use the extracted cellulose in the formation of a nanocomposite for the degradation of methyl orange.

4.2. Cellulose preparation from maize tassel

Maize tassels (MT) that form at the top of the stems of male maize plants were used for extraction of cellulose. Cellulose extraction was carried out according to the method shown in Figure 4.1.

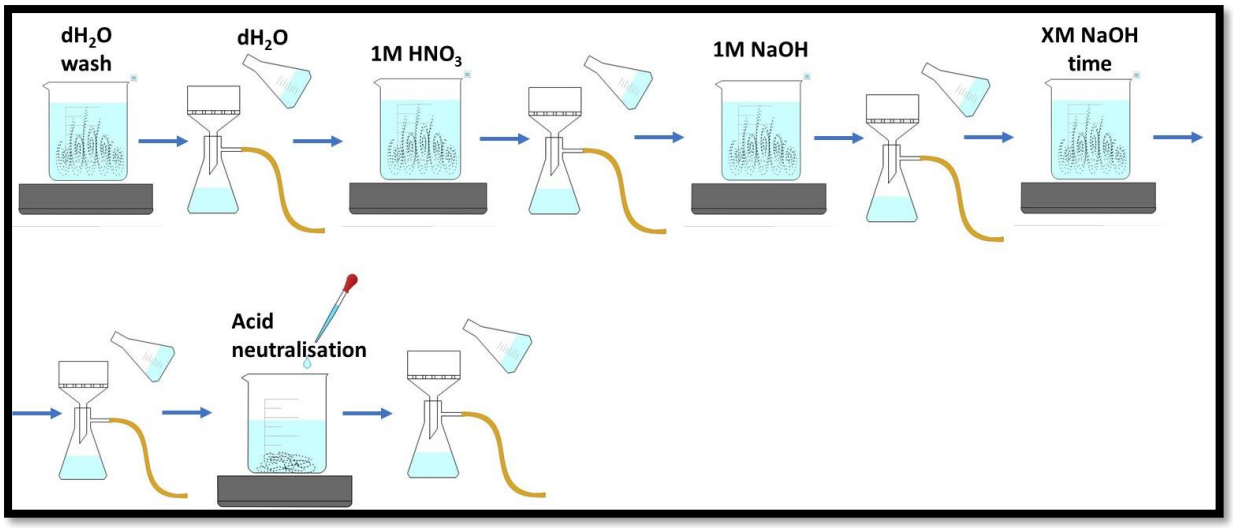

Figure 4.1: Diagram showing method of extraction of cellulose from maize tassel.

The methods of extraction and characterization are detailed in Chapter 3 however summarized in Table 4.1 are the parameters of the different experiments conducted. The NaOH concentration and NaOH treatment time were altered to see their effect on the resultant properties of cellulose. The Figure 4.1 is a visual representation of the experimental procedure. Figure 4.2 is a depiction of the maize tassel at each step of the procedure.

Table 4.1: Summary of maize tassel treatment conditions.

Sample	HNO_3 conc.	NaOH conc.	NaOH treatment time
CA		UNTREATED	
CB	1 M	2 M	24 h
CC	1 M	4 M	24 h
CD	1 M	6 M	24 h
CE	1 M	8 M	24 h
CF	1 M	10 M	24 h
CG	1 M	12 M	24 h
CH	1 M	14 M	24 h
CI	1 M	10 M	48 h
CJ	1 M	10 M	72 h
CK	1 M	10 M	96 h
CL	1 M	10 M	110 h

4.3. Results and discussion

4.3.1. The effect of NaOH concentration on the extraction of cellulose

FTIR is a means of identifying functional groups in unknown samples. Figure 4.3 show the FTIR of untreated maize tassel and treated maize tassel at different concentrations respectively. Table 4.2 is a summary of the corresponding wavenumbers and peak interpretations. The strong absorption around 3500-3250 cm^{-1} is attributed to OH stretching vibration (hydrogen bonding). The absorption band is composed of two vibrations (3285 cm^{-1}) for intermolecular hydrogen bonding and (3335 cm^{-1}) for intramolecular hydrogen bonding. The peaks around 3339 cm^{-1} and 2921 cm^{-1} are associated with α-cellulose (OH) stretching. Absorbance around 2918/2850 cm^{-1} are attributed to CH symmetric and asymmetric vibrations. The vibration at 983 cm^{-1} is attributed to the C-O-C [6]. The peak at 896 cm^{-1} is due to the β-glucosidic bond, attributed to C-O-C stretching during the C-H deformation of cellulose [8]. The hemicellulose peak occurs around 1730 cm^{-1} and 1240 cm^{-1} in the untreated maize tassel [8], both of which are not present in the alkali treated maize tassel (Figure 4.3). This indicated the removal of hemicellulose by alkali treatment [8]. The aromatic vibration around 1500 cm^{-1} is the C=C band from lignin's methoxyl group [9]. The C=C band appears weak in Maepa [9] as well. This was reduced in the alkali treated samples due to removal of hemicellulose. No other considerable changes were noted in other peaks. The dominant peak of CG at ~ 1350 cm^{-1} was due to water in the sample. The FTIR results indicated that lignin and hemicellulose were removed by alkali treatment from the maize tassel [9].

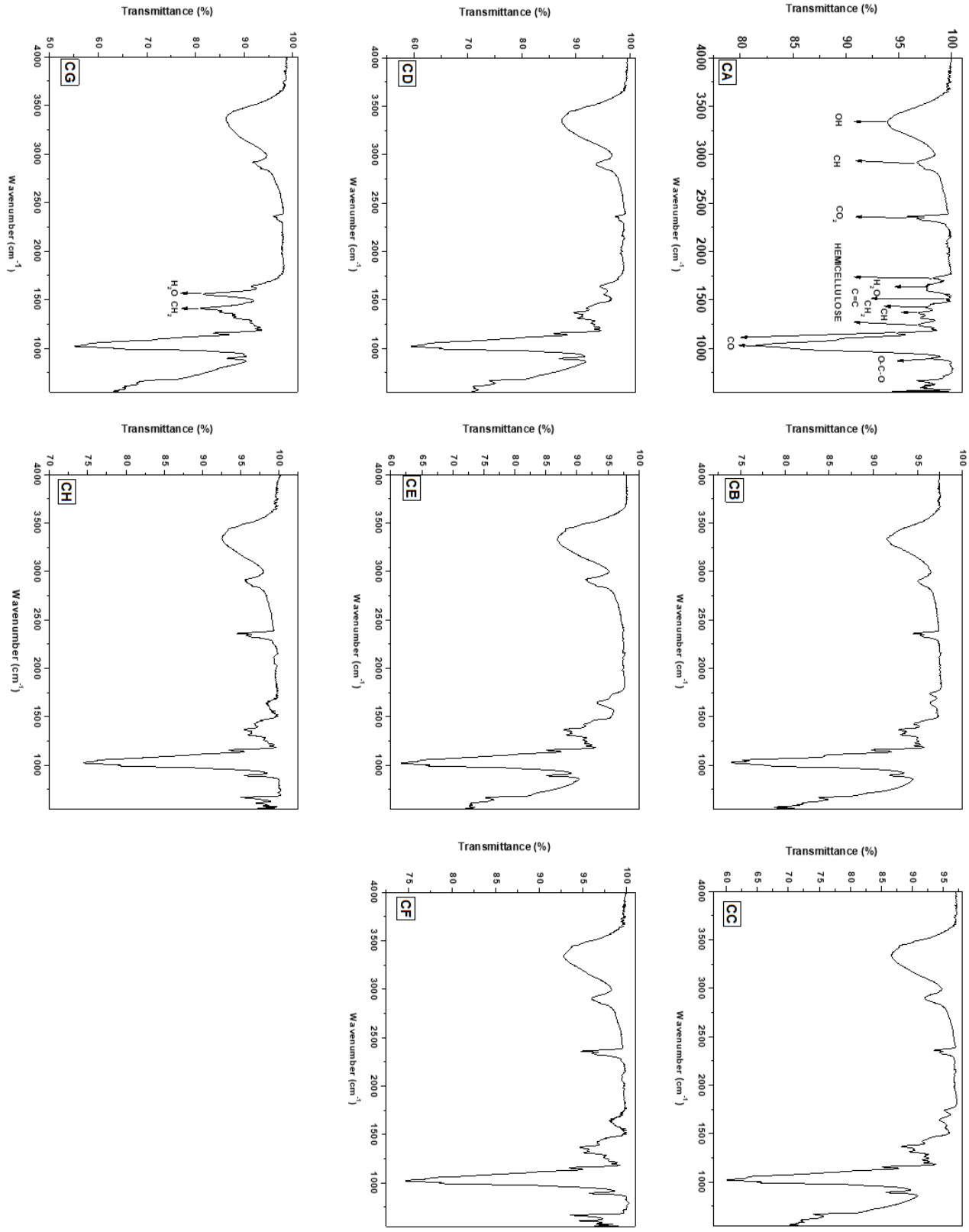

Figure 4.2: FTIR spectra of untreated cellulose (CA) and cellulose extracted at different NaOH concentrations (CB-CH).

Table 4.2: The wavenumber and associated peak interpretations of untreated cellulose and NaOH extracted cellulose [6, 9].

Wavenumber (cm^{-1})	Assignment
3450-3435	OH stretching
3285	Intermolecular H bonding
3235	Intramolecular H bonding
2918	C-H symmetric stretch
2850	C-H asymmetric stretch
1649	H_2O
983	β-link (glucosidic bond)
1161	Antisymmetric bridge C-O-C stretch
1730	Hemicellulose
1240	Hemicellulose

X-ray powder diffraction (XRD) is a rapid analytical technique that is used for phase identification of a crystalline material (e.g. minerals, inorganic compounds) and provides information on unit cell dimensions [10]. The X-ray diffractograms of the extracted cellulose in the present study are shown in Figure 4.4 and Table 4.3 is a summary of the crystallinity index for each NaOH concentration treatment. Different peaks are observed in all samples at 17° and 22.6°. These are characteristic of the crystal polymorphs of cellulose [5]. The peak at 2θ, 17° corresponds to the (110) crystallographic plane and at 2θ 22.6° corresponds to the (002) plane.

The crystallinity indices were derived using the following equation [11]:

$$CI\ (\%) = \frac{I_{002} - I_{am}}{I_{002}}\ X\ 100 \qquad \text{Equation 4.1}$$

Where I_{002} is the intensity of diffraction maximum of crystalline region close to 22˚, while I_{am} is the intensity value for the amorphous cellulose region close to 17.3˚ [11].

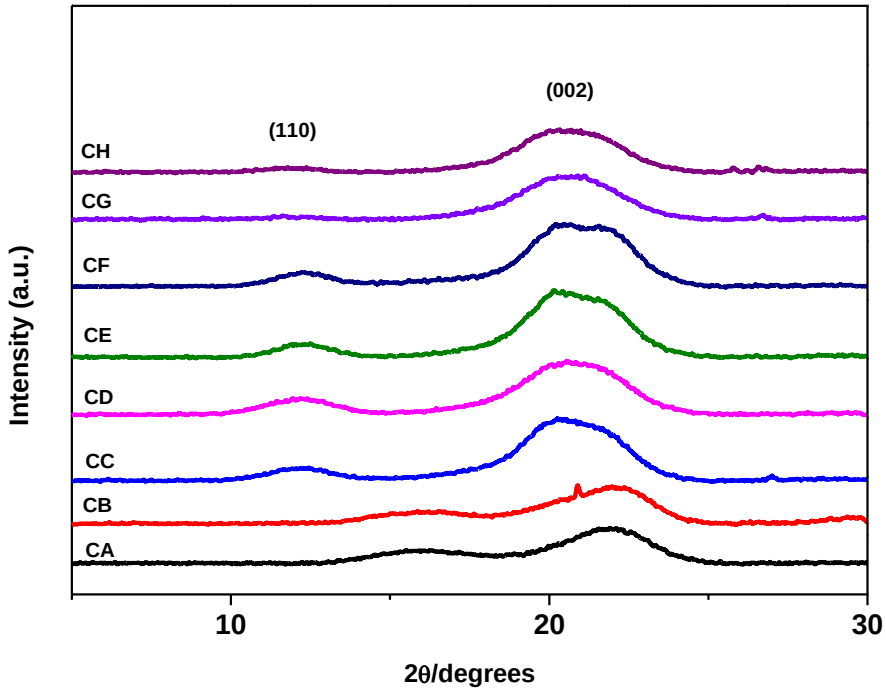

Figure 4.3: X-ray diffractograms of untreated cellulose (CA) and cellulose extracted at different NaOH concentrations (CB-CH).

Pre-treatment process increases the lignocellulosic crystallinity [4]. Changes in the crystallinity index are governed by two competing factors: lignin and hemicellulose removal, causes an increase in the crystallinity index, whereas swelling and dissolution of crystalline cellulose, causes a decrease in the crystallinity index. The crystallinity index of the maize tassel fibre increased with an increase in alkali concentration, samples CA-CG, however in sample CH, there was a slight reduction in crystallinity index, indicating a limitation in higher NaOH concentrations for the removal of protective materials and possible relaxation of stress in the cellulose chains [12]. The lignin and hemicellulose removal during pre-treatment are generally accepted [4]. The method used was designed for removing most substances, leaving only cellulose. The treatment is also a means of extracting cellulose II because of the alkali. From the XRD patterns in Figure 4.4 and the calculated crystallinity indices in Table 4.3, the crystallinity increases with increasing concentration of alkali treatment up to the 12 M mark. The (110) and (002) peaks indicate the difference between hemicellulose (amorphous material) and α-cellulose which is also an indication of the treatment method [10]. The (110) peak is a reference for hemicelluloses and the (002) peak indicates α-cellulose [10]. What can also be seen from the XRD data is the difference between cellulose I and cellulose II peaks. The (110)

peak is around 15° in cellulose I whereas cellulose II has the (110) peak is around 12°. The (002) peak shifts to a lower angle, again indicative of conversion from cellulose I to cellulose II [10]. Treatment with an alkali produces cellulose II [1, 3, 5], which is evident in samples CC-CH. CA and CB remain as cellulose I due to the position of the (001) and (002) peaks. Due to the structural complexity of the poly-carbohydrates, pretreatment of MT is required to disrupt the structure of lignocellulose material. Alkali treatment makes cellulose soluble due to the formation of sodium salt and separated it from other constituents. The acid neutralization regenerates the insoluble cellulose with a modified structure process of pure cellulose.

Table 4.3.: The crystallinity indices of untreated cellulose (CA) and cellulose extracted at different NaOH concentrations (CB-CH).

Sample	Crystallinity index (%)
CA	80.47
CB	80.12
CC	97.18
CD	97.68
CE	98.17
CF	98.24
CG	98.73
CH	95.61

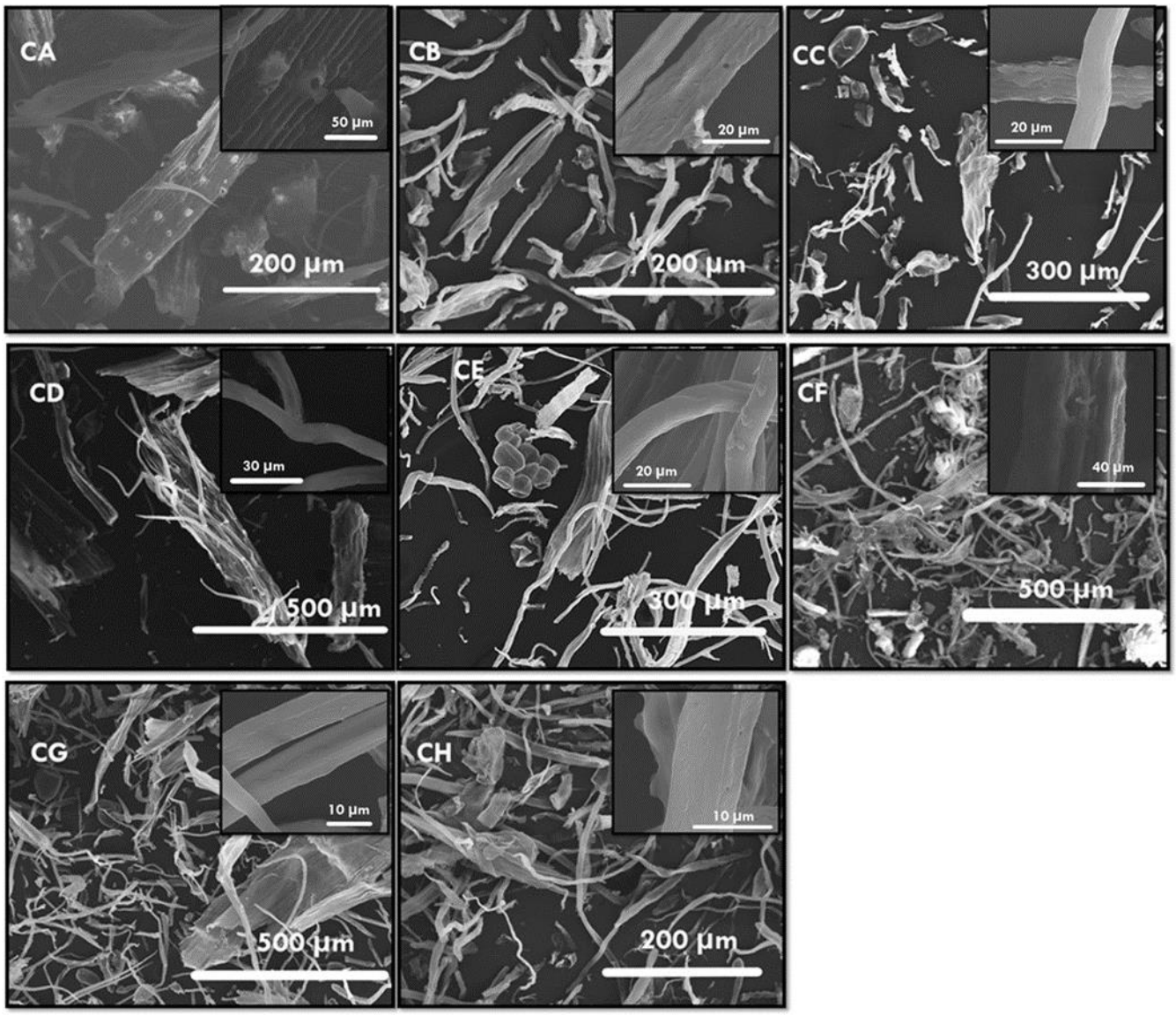

Figure 4.4: SEM micrographs showing the distribution of fibers of untreated cellulose (CA) and cellulose extracted at different NaOH concentrations (CB-CH) and their corresponding high-magnification SEM images as inserts.

The morphology of the cellulose (CA-CH) was examined by SEM. As shown in Figure 4.5, the fibers have a relatively smooth surface. The average diameter of a single fiber in each sample is about 13.7 µm. The untreated maize tassel fibers in Figure 4.5 denoted as CA, have a relatively smooth surface, owing to the wax layer, with linear ridges and furrows. The surface of the maize tassel is composed mainly of lignin, pectin, ash and hemicellulose that enclose the fiber. Image CA in Figure 4.5 shows a piece of the plant that has not fractured by the blending procedure and is an intact segment of the tassel and also shows hair like structures as well as stomata on the surface of the maize tassel. The remaining images CB-CH, even though there

are fragments of intact tassel, the surface is not as intact as in CA, the stomata are not clearly visible, and the plant is fractured into smaller fibers. CD shows a segment of the tassel that has partially separated, and the surface is not as smooth as in CA. From SEM analysis, it appears that the degree of fractionation increases from CA-CH. The plant material is broken into its minimalist form of microfibers. From sample CB-CH, fiber size is reduced, possibly due to hemicellulose removal. This reduction in size of the fiber may increase the bonding capacity, giving an advantage in the construction of composites. The tassel is reduced to macrofibrils and these are further broken into individual microfibrils or microfibers. Some internal transport vessels such as xylem and phloem are also seen in the images [13].

4.3.2. Effect of NaOH treatment time on the extraction of cellulose

The FTIR analysis of the effect of NaOH treatment time (48-110 hr) on the extraction of cellulose is shown in Figure 4.6. The spectra in Figure 4.6 show similar spectra compared to Figure 4.3. However, sample CL in the Figure 4.6 has a small hemicellulose peak at ~1700 cm^{-1} possibly exaggerated by the prominent H_2O peak at 1650 cm^{-1}. CI and CL appear to have similar spectra which could be explained by the higher content of H_2O in the samples. The CO_2 is from the instrument and not the sample. There are no other significant changes.

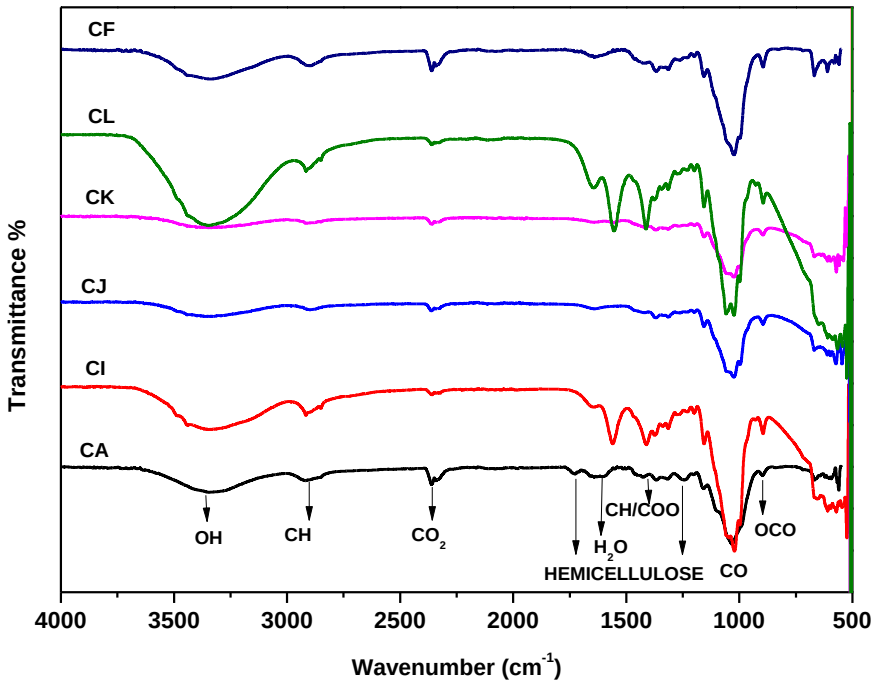

Figure 4.5: FTIR spectra of cellulose extracted using 10 M NaOH at different times 48-110 hours (CI-CL) as well as CA (untreated) and CF (10 M NaOH/24 hr).

The XRD patterns in Figure 4.7 shows that sample CL, a long treatment time has the effect of decreasing crystallinity due to the low intensity of the (110) peak. There are no other major differences in the patterns of sample CI-CL. However, compared to untreated tassel CA, the pattern indicates that cellulose I which is the natural cellulose is converted to cellulose II in samples CI, CJ, CK and CL. According to Motaung [3], Perel [14] and Ciolacu et. al [15], the doublet XRD peak at (002) is indicative of the cellulose II crystalline structure.

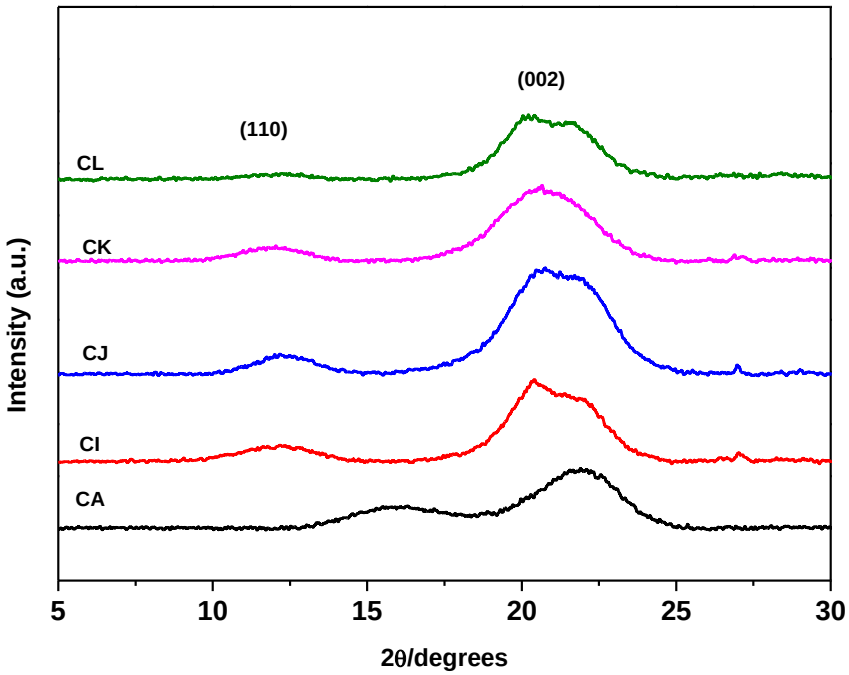

Figure 4.6: X-ray diffractograms of untreated cellulose (CA) and cellulose extracted using 10 M NaOH at different times 48-110 hours (CI-CL).

Table 4.4 shows the crystallinity indices of the extracted cellulose over time (48-110 hr) in 10 M NaOH. The crystallinity indices do not change by much. The samples remained highly crystalline however the CJ shows slightly better crystallinity hence confirming that 72-hours as the best extraction time.

Table 4.4: The crystallinity indices of cellulose extracted using 10 M NaOH at different times 48-110 hours (CI-CL)

Sample	NaOH treatment time (hr)	Crystallinity Index
CA	0	80.47
CI	48	98.66
CJ	72	98.65
CK	96	97.47
CL	110	98.31

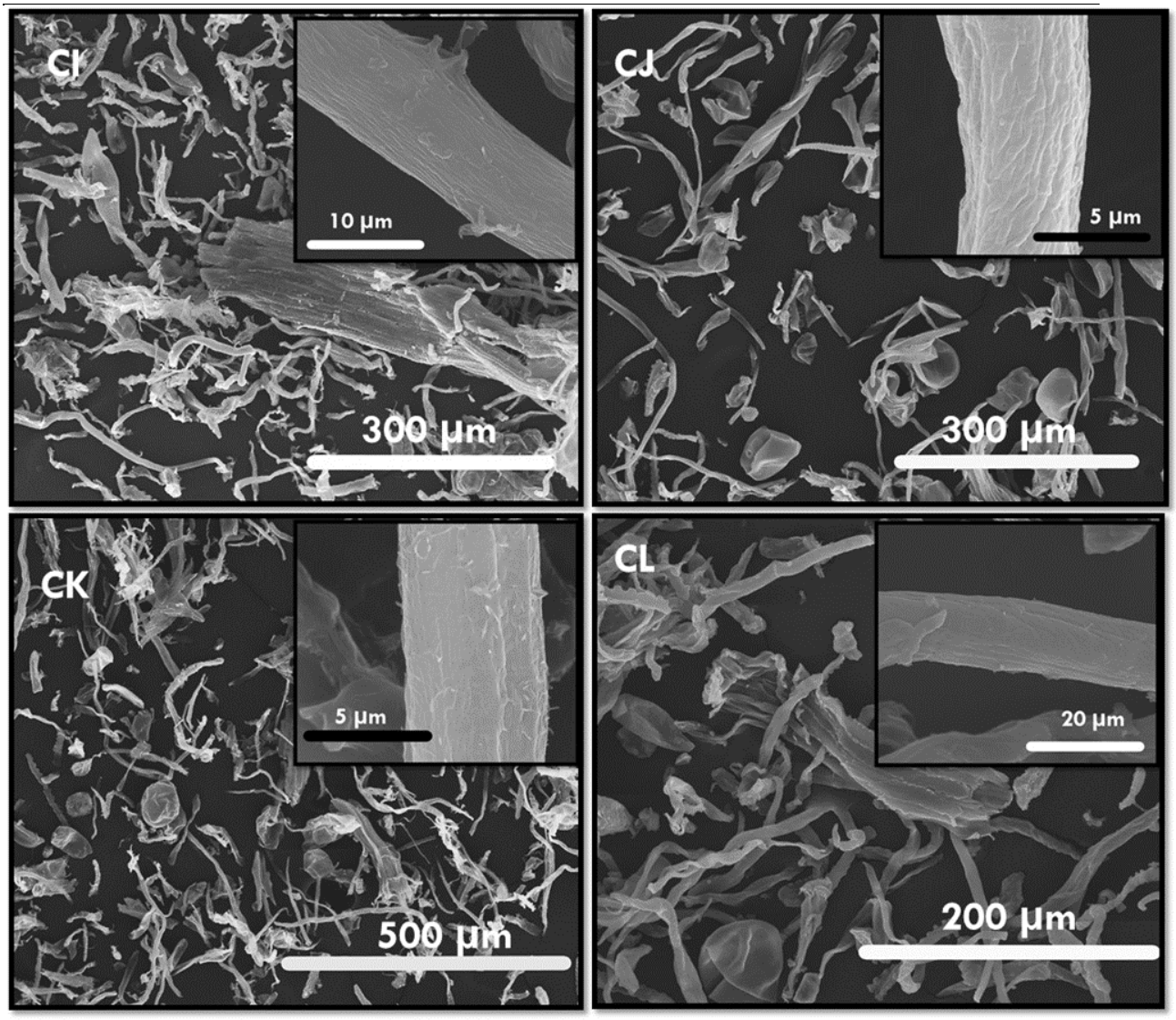

Figure 4.7: SEM images showing the distribution of fibers of cellulose extracted using various times 48-110 hours (CI-CL) in alkali 10 M NaOH and the insert focuses on individual fibers.

The SEM images of CI-CL in Figure 4.8 do not differ much, they are equally fractionated into the microfibrils and have very similar appearances physically. The untreated cellulose fractionated into smaller components and transport vessels. There are minor differences in the microfibrils of the untreated cellulose as compared to others, however all samples showed peeling and grooves. Figure 4.8 inserts shows that there are no significant differences of the cellulose extracted at different times as they all form smooth bundle fibers.

Zhao *et al.* [16] pretreated bagasse using peracetic acid which increased the crystallinity index due to the removal of lignin. This was consistent with Wang *et al.* [9] that found 2% NaOH treatment was more conductive than 4% NaOH treatment. They also found that the optimal condition for pretreatment was 2% NaOH solution at 80 °C for 2 hours followed by ozone treatment for 25 min with an initial pH 9. Under these optimum conditions, the relative content of cellulose in the treated sample was 62.46%, the removal rate of lignin was 84.35% and the relative content of hemicellulose was 13.74%, they also found a change in the surface structure of the fiber after treatment, showing more pores and exposed fiber bundles. These are consistent with our findings of alkali treatment to remove cellulose from maize tassel. Between the time study and the concentration study, time spent in 10 M NaOH had no significant effect on the degradation of the maize tassel physically.

4.4. Conclusion

Herein, we reported on the pre-treatment of maize tassel in order to disrupt the lignocellulose structure. The alkali treatment solubilizes the cellulose by the formation of sodium salt, which is separated from other constituents. Acid neutralization then regenerates the insoluble cellulose with a modified structure of cellulose. The results obtained show that cellulose was extracted from maize tassel successfully however the quality was dependent more so on the concentration of the NaOH rather than the time taken for extraction. The XRD results indicate an increase in crystallinity, degree of crystallization, and a peak shift of the (110) peak, confirmed the formation of cellulose II after alkali treatment. The FTIR results indicated the dissolution of hemicellulose and other compounds to form pure cellulose in all treatment methods. By comparison of concentration and time, it was found that both CC (4 M) and CF (10 M) NaOH treated samples showed better cellulose extraction however the time spent on extraction had no major effect on the formation of cellulose. As such, the 10 M NaOH treated sample (CF) was used in the composite formation with TiO_2.

4.5. References

1. Wan Ngah W. S, Hanafiah M. A. K. M., Bioresources Technol., 2008, 99, 3935-48.
2. Foo K. Y., Hameed B. H., Renew. Sust. Energ. Rev., 13, 2495-2504.
3. Motaung T. E., Mtibe A., Mater. Sci. Appl., 2015, 6, 1022-32.
4. Vaz Jr. S., Springer International Publishing, 2018, 1-9.
5. Klemm D., Heublin B., Fink H-P., Bohn A., Angew. Chem. Intl. Ed., 2005, 44, 3358-93.
6. Kim J., Yun S., Macromolecules, 2006, 39, 4202-06.
7. Bali G., Meng X., Deneff J. I., Sun Q., Ragauskas A. J., ChemSusChem, 2015, 5, 275-9.
8. Jayaramudu J., Guduri B. R., Varada Rajulu A., Int. J. Polym. Anal. Charact., 2009, 14, 115–125.
9. Wang W., Zhang C., Tong S., Cui Z., Liu P., Molecules, 2018, 23, 2-13.
10. Abas Z., Kim H. S., Kim J., Kim J-H., Front. Mater., 2014, 17, 1-4.
11. Sarko A., Muggli R., Macromolecules, 1974, 7, 486-94.
12. Maepa C. E., Jayaramudu J., Okonkwo J. O., Ray S. S., Sadiku E. R., Ramontja J., Int. J. Polymer Anal. Charact., 2015, 20, 99-109.
13. Beck B. B., Cambridge University Press, 2005, 59-64.
14. Perel J., J. Textile Inst., 1990, 81, 241-44.
15. Ciolacu D., Ciolacu F., Popa V. I., Cellulose Chem. Technol., 2011, 45, 13-21.
16. Zhao X. B.,Wang L., Liu D. H., J. Chem. Technol. Biotechnol., 2008, 83, 950-56.

CHAPTER 5

The synthesis of anatase TiO_2 nanoparticles by sol-gel

5.1. Introduction

Nanomaterials have been investigated because of their unique properties. Titania nanoparticles are very popular due to their chemical structure, physical, optical and electrical properties. Titania has been used in many applications including paints, sensors and photocatalysis. TiO_2 exists in three mineral forms, anatase, rutile and brookite. Each of these have their own crystal structure and properties. The basic structure consists of a Ti atom surrounded by six O atoms in octahedral configuration [1]. The anatase form is preferred since it has the highest photocatalytic activity [2]. Anatase also has a more negative conduction band edge potential, high specific area, is non-toxic, as well as inexpensive and photochemically stable [2]. The TiO_2 morphologies that have been studied, include nanotubes, nanowires, nanorods and mesoporous structures [2]. There are various methods of production and each produce different structures of TiO_2. These methods include carbon vapor deposition (CVD), sol-gel, solvothermal, hydrothermal and electrodeposition to name a few [2].

The common method of synthesis of TiO_2 nanoparticles is by sol-gel. The advantages of sol-gel method include low process temperature, versatility, homogeneity and stability [2-5]. With the sol-gel method, a larger water presence, requires a higher hydrolysis rate to condense into Ti-O-Ti chains. An excess of water will supress the Ti-O-Ti species formation due to the favourable formation of Ti-OH [2-4]. Calcination is important for the removal of organic molecules from the products to complete crystallisation. A higher calcination temperature causes agglomeration and phase transformation [2-4]. An important property of TiO_2 nanomaterial is the photocatalytic activity in applications that range from antibacterial surfaces to photocatalytic reactions. The electron hole-pair generation of TiO_2 is useful. The energy required may be supplied by photons in the near UV region. When TiO_2 is illuminated with light ($\lambda < 390$ nm), an electron is excited out of its energy level, leaving a hole in the valence band. The electrons are promoted from the valence band to the conduction band to give the electron-hole pair. The valence band (h^+) potential generates hydroxyl radicals OH at the surface on TiO_2 and the conduction band (e^-) is negative enough to reduce molecular oxygen. The hydroxyl radical is a powerful oxidising agent and may attack organic matter at the surface of TiO_2 [6]. Amorphous TiO_2 hardly gives photocatalytic activity because of nonbridging O

atoms in the bulk TiO_2 where Ti-O arrangement defects act as recombination centres of the photo-catalytically generated electron-hole pairs. The possible application of anatase TiO_2 as a photocatalyst is due to several factors [1]:

- room temperature photocatalytic reaction.
- photocatalytic reactions do not suffer drawbacks of photolysis reactions due to pollutants being completely mineralised to non-toxic products.
- the photocatalyst is cheap and may be supported on various substances.
- the photogenerated holes are oxidising while photogenerated electrons reduce sufficiently to produce superoxides from dioxygens.

The aim was to use the synthesised TiO_2 nanoparticles in the formation of a nanocomposite for use as a photodegradation complex. The objective was to synthesise anatase TiO_2 nanoparticles.

5.2. Synthesis of TiO_2 nanoparticles

About 10 mL of $Ti(OBu_4)$ was dissolved in 10 mL anhydrous ethanol, and ultrasonically dispersed to produce a mixture. 5 mL of water were slowly added dropwise into the mixture, which was stirred for 2 h at room temperature. The solution was aged for 24 h at ambient temperature, followed by filtration, washed several times with deionized water and ethanol, dried at 100 °C for 12 h to form a precursor powder. Calcination of the precursor at 450 °C for 2 h in air resulted in the formation of anatase TiO_2 nanoparticles. The product was then characterised by FTIR, Raman spectroscopy, XRD, TEM, UV-Vis, PL, TGA and SEM equipped with EDX. Figure 5.1 summarises the synthetic procedure. A detailed procedure with characterisation techniques is reported in Chapter 3.

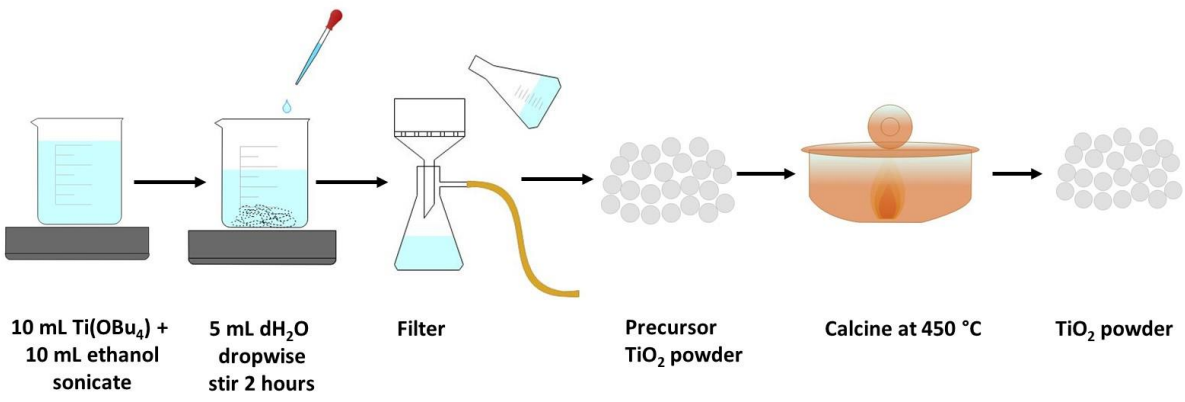

Figure 5.1: A brief summary of method used to synthesise TiO_2 nanoparticles.

5.3. Results and discussion

The thermogram of non-calcined TiO_2 is shown in Figure 5.2 (a). There is a weight loss around 150 °C, owing to surface water. The remaining reduction in weight is due to loss of organic compounds. After around 700 °C, the decomposition is complete, and no additional weight loss occurs, and the remaining product is TiO_2. From Figure 5.2 (b) the TGA of the calcined sample is shown. The first weight loss at 150 °C may correspond to adsorbed water on the surface of the TiO_2. The second weight loss 500-750 °C may be due to a phase change from anatase to rutile [7]. The third weight loss 750-900 °C may be due to residual organic groups in the synthesised TiO_2 [7]. The Titanium butoxide precursor has a higher reactivity compared to other precursors due to the variable oxidation capacity; titanium (IV) butoxide reacts with deionised water, which leads to hydrolysis and condensation. The titanium ion precursors vacant d orbitals can increase the coordination number from 4 to 6. Reaction kinetics may be thought of as [8]:

$$Ti(OCH_1H_9)_4 + 4H_2O = Ti(OH)_4 + 4C_4H_9OH \quad \text{Equation 5.1}$$

$$Ti(OH)_4 = TiO_2 \downarrow + 2H_2O \quad \text{Equation 5.2}$$

During the precipitation, primary particles nucleate initially and aggregate to form secondary particles which form spherical aggregates of nanosized anatase TiO_2, after calcination [5].

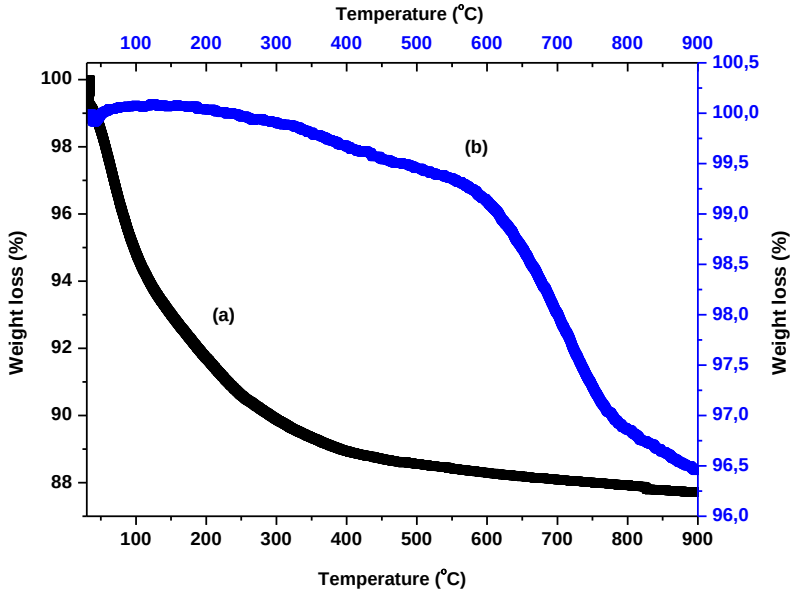

Figure 5.2: Thermograms of (a) non-calcined TiO_2 and (b) calcined TiO_2.

The FTIR analysis was done to ascertain the functional groups in the synthesized TiO_2. These functional groups will help to encore the TiO_2 onto the cellulose to form the composite. Figure 5.3 shows the FTIR spectrum of TiO_2 nanoparticles which has three peaks, distinctive of anatase TiO_2 nanoparticles. The first band is the broadest observed at 3250 cm^{-1}, this corresponds to the stretching vibration of the hydroxyl OH group. The second band around 2150 cm^{-1} corresponds to the bending mode of surface adsorbed water Ti-OH. The last prominent peak is at 1650 cm^{-1} which relates to Ti-O modes [9-11]. The CO_2 peak observed is due to the instrument and atmosphere.

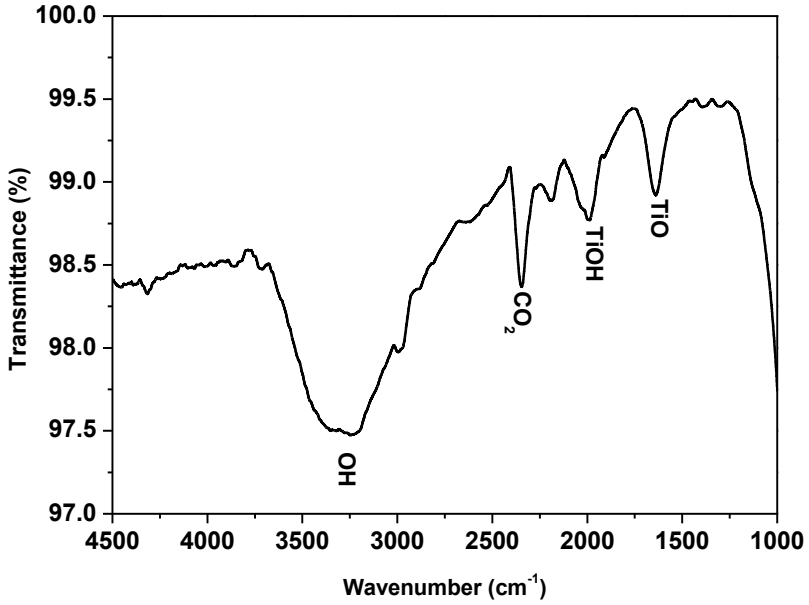

Figure 5.3: FTIR spectrum of the TiO_2 nanoparticles.

Raman spectroscopy is also a useful tool for structural analysis. Herein Raman spectroscopy was used to characterise the obtained powder. Three different spots were scanned. The spectrum in Figure 5.4 shows the Raman peak shifts for anatase TiO_2. A distinct Raman fingerprint of anatase TiO_2 is observed [12]. The anatase phase has six Raman active vibrations, three E_g modes, two B_{1g} modes and one A_{1g} mode. The six modes are A_{1g} (517 cm^{-1}), $2B_{1g}$ (397 and 517 cm^{-1}) and $3E_g$ (144, 197 and 640 cm^{-1}) are Raman active [12]. In Figure 5.4, there are five peaks at 144, 397, 517 and 644 cm^{-1}. A decrease in the particle size causes the Raman peaks to broaden with an increase in frequency [12]. The most intense E_{1g} mode shows a maximum blue shift with a decrease in crystallite size. A small blue shift for the E_{g2} mode and the B_{1g1} and combined B_{1g2} + A_{1g} modes show small blue and red shifts respectively. The

frequency shifts of the A_{1g} and B_{1g} modes are not pronounced. The E_{g3} mode has significant broadening as well as red shift as crystallite size is decreased [12].

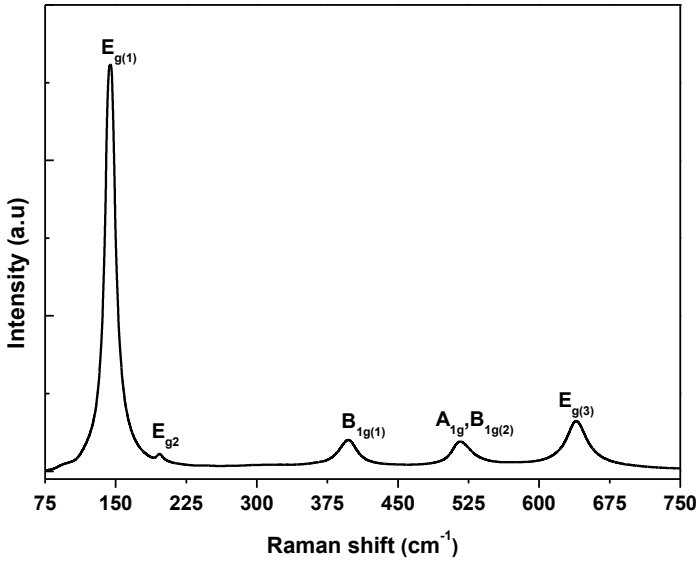

Figure 5.4: Raman spectrum of the TiO_2 synthesised by sol-gel method.

XRD was used to examine the crystallinity of the TiO_2 nanoparticles and confirm the phase. The XRD pattern in Figure 5.5 corresponds to the anatase phase of TiO_2, PDF 00-004-0477. The structure of anatase is tetragonal. The crystallographic unit of anatase TiO_2 is body centred with a space group D_{4h}. The cell is composed of two primitive ones, each with two TiO_2 units The anatase phase diffraction peaks at 2θ = 25°, 37°, 48°, 54°, 62° and 68°, 76° and 83° correspond to the (101), (103), (200), (105), (213) and (116), (107) and (303) planes [4]. The sharpness of the peaks indicates highly crystalline nanoparticles.

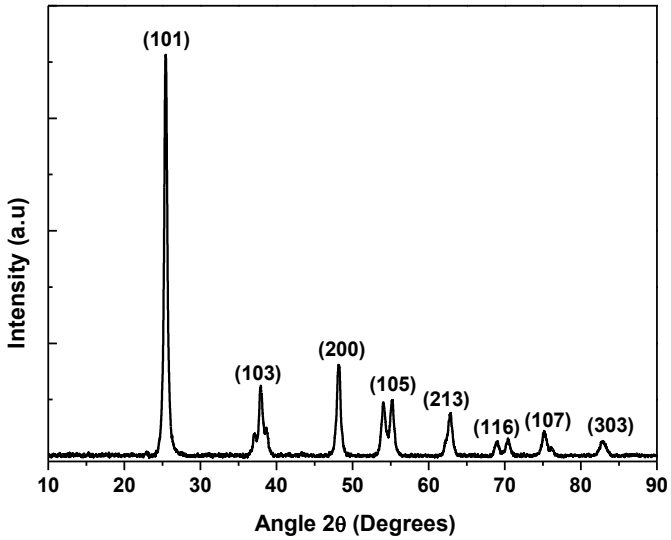

Figure 5.5: XRD pattern of the TiO_2 synthesised by sol-gel method.

The average crystallite size was calculated using the Scherrer equation (equation 5.3) where *B* is the *FWHM*, *K* is a Scherrer constant approximately 1 and *L* is the crystallite size. For the synthesised anatase TiO_2, it was found that the average crystallite size was ca. 10.8 nm.

$$B(2\theta) = \frac{K\lambda}{L\cos\theta} \qquad \text{Equation 5.3}$$

A FEI NOVA Nanolab 600 SEM was used to investigate the morphology of the particles by scanning the material's surface. The sample preparation required the material to be crushed and coated with gold and palladium. This layer inhibits charging, reduces thermal damage and enhances the secondary electron signal for topographic analysis. The SEM image in Figure 5.6 (a) shows high homogeneity of the sample. Nanoparticles smaller than 50 nm agglomerate to form colonies. The nanoparticles formed were spherical in shape and mostly uniform in size with an average diameter of 0.0016 nm. The agglomeration of particles into colonies was observed in SEM and TEM due to sintering of crystals in the calcination process [4, 13]. According to Ba-Abbad *et al.* [13], the calcination temperature determines the particle size and extent of agglomeration of nanoparticles. The anatase TiO_2 particles have self-assembly into close packed, dense, well-crystallised, unevenly sized and irregular sub-nanoaggregates, observed in the TEM Figure 5.6 (b). From analysis using image J software, the particle size distribution in Figure 5.6 (c) suggests the nanoparticles were mostly between 5 and 10 nm, which agrees with the size calculated from the XRD Scherrer equation.

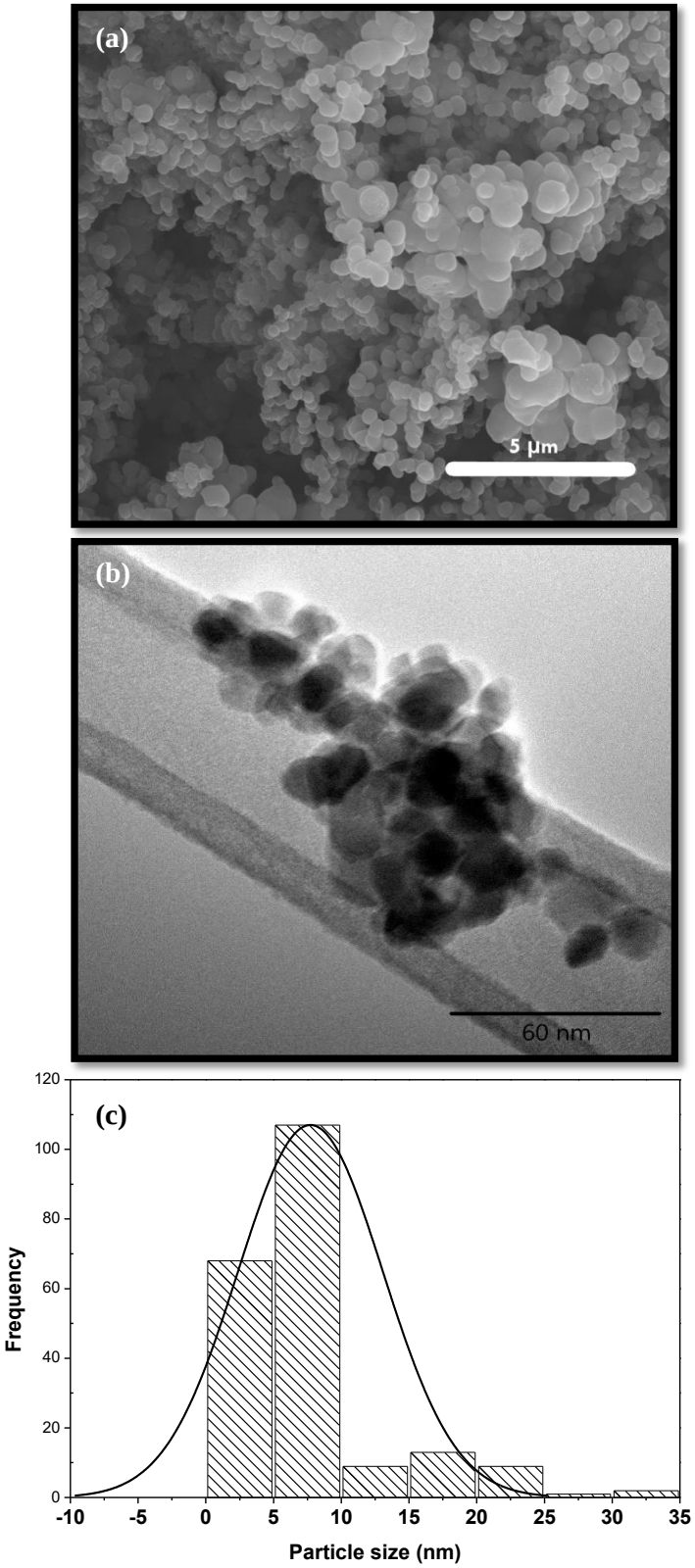

Figure 5.6: (a) SEM image and (b) TEM image showing anatase TiO_2, and (c) particle size distribution.

The elemental composition was determined by EDX analysis. The spectrum in Figure 5.7 has prominent peaks of Ti and O, confirming the anatase TiO_2 nanoparticles that were synthesised by the sol-gel method. Ti has electrons in the $K\alpha_{1,2}$ shells and gives an EDS count at 4.5 keV. The presence of gold and palladium is due to the coating that was done in order to prevent charging. The presence of carbon is from the tape used to hold the sample.

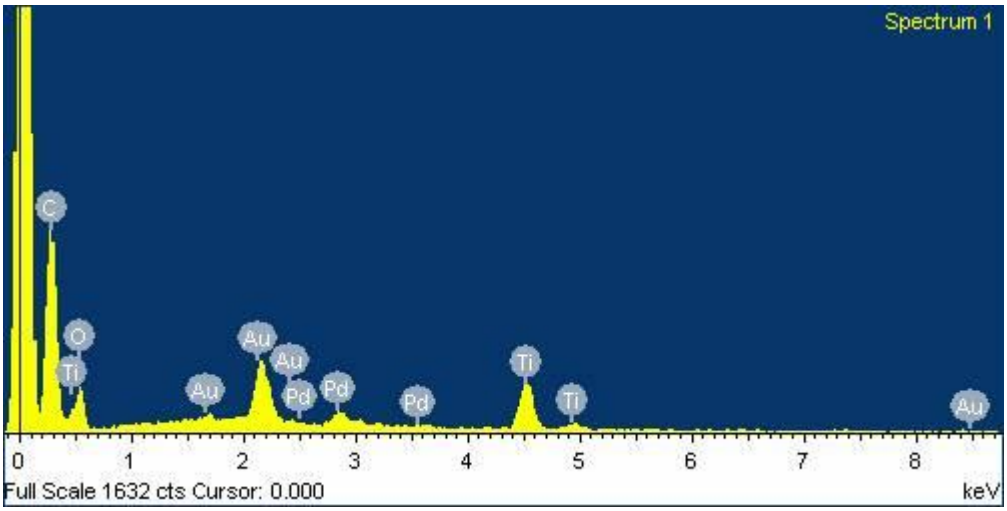

Figure 5.7: EDX spectrum of anatase TiO_2 prepared by sol-gel method.

From the UV-Vis absorption spectrum, Figure 5.8, the excitonic peak is around 324 nm, however the spectrum is tailing. The bulk band gap of anatase TiO_2 is 3.2 eV [14]. To estimate the bang gap, a Tauc plot was used and is shown in Figure 5.8. A Tauc plot is used to derive the band-gap energy of a semiconductor with an indirect or direct transition using the relationship below where *h* is the Planck's constant, *v* is the frequency of light, and E_g is the band-gap energy (equation 5.4) [15]. The value of the exponent *n* is related to the electronic nature of the bandgap, with values of 3, 2, 3/2, and 1/2 corresponding to indirect forbidden (IF), indirect allowed (IA), direct forbidden (DF), and direct allowed (DA) transitions, respectively [15].

$$\alpha h\nu \propto (h\nu - E_g)^n \qquad \text{Equation 5.4}$$

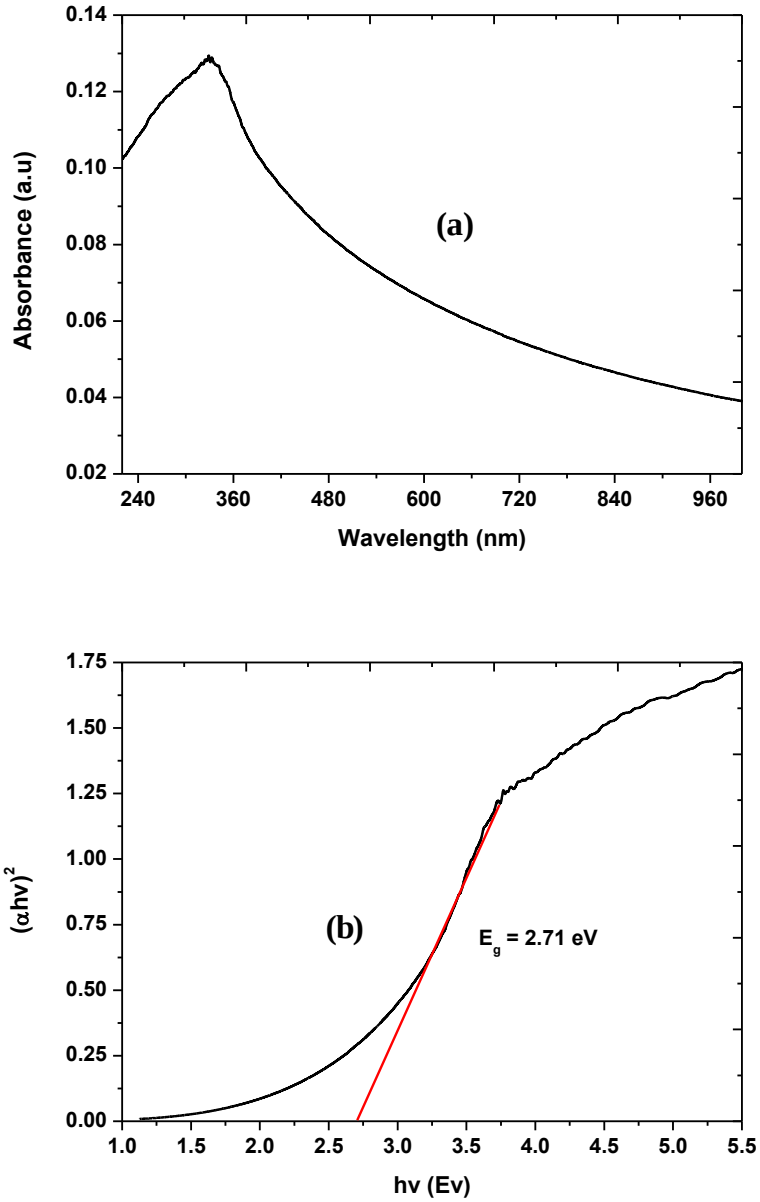

Figure 5.8: (a) UV-Vis absorption spectrum of the anatase TiO_2 and (b) its corresponding Tauc plot.

Anatase TiO_2 is an indirect band gap semiconductor with an *n* value of 2. The estimated band gap is 2.71 eV, indeed blue-shifted from the bulk band gap of 3.2 eV. The blue-shift is due to quantum confinement effects [15]. As the size of the nanoparticles become smaller, there is a discretization of the density of states which result in the increase in band gap energy as shown in Figure 5.9.

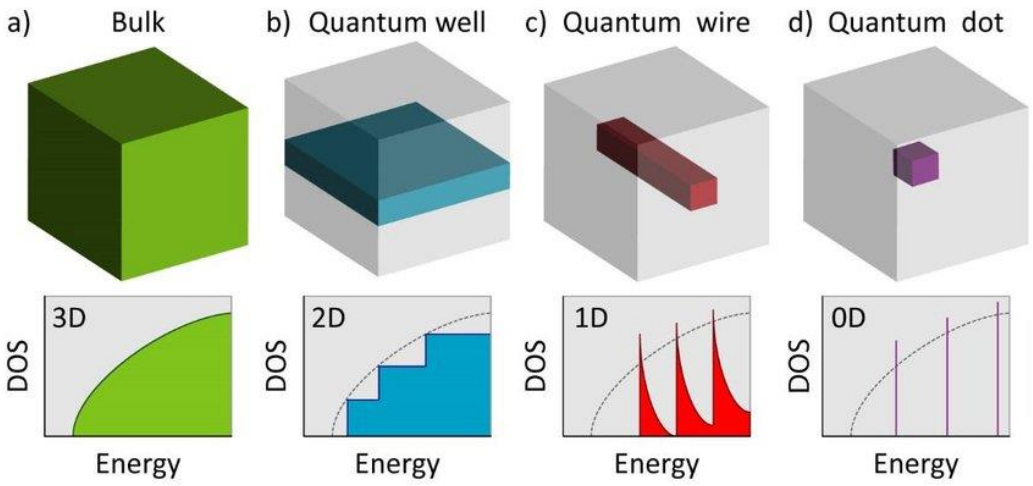

Figure 5.9: Schematic representation of dimensionality in bulk (3D), quantum well (2D), quantum wire (1D) and quantum dot (0D). Corresponding densities of states versus energy are given below each diagram [16].

The photoluminescence (PL) spectrum of the anatase TiO_2 is shown in Figure 5.10. The peak centred at about 398 nm in the PL spectra is related to the electron transition from the valence band and the conduction band of TiO_2 [17] while the peaks at 420, 454, 490 and 533 nm can be assigned to charge transitions from an oxygen vacancy trapped electron, recombination of self-trapped excitons and intrinsic states of TiO_2 [18]. In particular, the peak at 420 nm arising from the indirect band edge allowed transitions and self-trapped excitons localized in TiO_6 octahedra while the peak at around 454 nm is due to charge transfer transition from Ti^{3+} to the O_2^- in $(TiO_6)^{8-}$ [17, 18]. Furthermore, the peaks at around 454 nm, 490 nm and 533 nm originate from oxygen vacancies and surface defects of TiO_2. These charge carriers are generally trapped by oxygen vacancies and surface hydroxyl groups, which contribute in their visible luminescence [18].

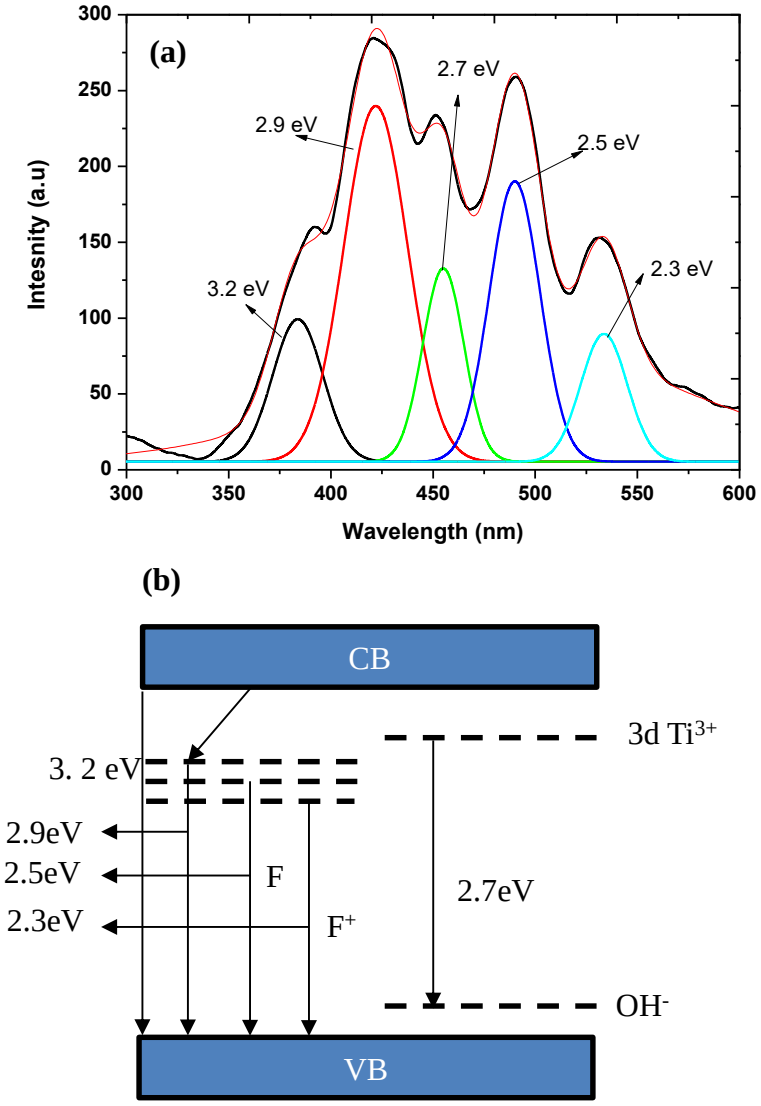

Figure 5.10: (a) Photoluminescence spectrum of anatase TiO_2 and the corresponding mechanism (b).

5.4. Conclusion

Anatase TiO_2 crystals were synthesised using the sol-gel method in absolute ethanol. The morphology of the samples contained spherical particles with an average particle size of between 5 and 10 nm. The formation of TiO_2 was confirmed by EDX, XRD and Raman spectroscopy. The shape and size of the particles were confirmed by TEM and SEM analysis. The optical properties were confirmed using UV-Vis and photoluminescence spectroscopy. These nanoparticles will now be used in the formation of composite with cellulose to further be used in the degradation of methyl orange dye.

5.5. References

1. Akpan U.G., Hameed B. H., J. Haz. Mater., 2009, 170, 520-29.
2. Byranvand M. M., Kharat A. N., Fatholahi L., Beiranvand Z. M., J. Nano. Sci., 2013, 3, 1-9.
3. Yang H., Zhang K., Shi R., Li X., Dong X., Yu Y., J. Alloy. Compd., 2006, 413, 302-6.
4. Phonkhokkong T., Thongtem T., Thongtem S., Phuruangrat A., Promnopas W., Dig. J. Nanomater. Bios., 2016, 1, 81-90.
5. Sugimoto T., Zhou X., Muramatsu A., J. Colloid Interface Sci., 2003, 259, 43-52.
6. Khataee A. R., Kasiri M. B., J. Mol. Catal., 2010, 328, 8-26.
7. Leon A., Reuquen P., Garin C., Segura R., M., Vargas P., Zapata P., Orihuela P. A., Appl. Sci., 2017, 49, 1-9.
8. Tauc J., Grigorovici R., Vancu A., Physica Status Solidi B, 1966, 15, 627-37.
9. Nadica D., Abazovic M., Comor M., Dramicanin D., Jovanovic S., Jovan M., J. Phys. Chem. B, 2006, 110, 25366-70.
10. Mugundan S., Rajamannan, G., Viruthagiri N., Shanmugam R., Gobi P., Appl. Nanosci., 2015, 5, 449-56.
11. Periyat P., Leyland N., McCormack D. E., Colreavy J., Corr D., Pillai S. C., J. Mater. Chem., 2010, 20, 3650-55.
12. Sharma A., Kara R. K., Pandiyan S. K., J. Basic Appl. Eng. Res., 2014, 9, 1-5.
13. Ba-Abbad M. M., Kadham A. A. H., Mohamad A. B., Takriff M. S., Sopian K., Int. J. Electrochem. Sci., 2012, 7, 4871-88.
14. Abazovic N. D., Comor I. M., Dramicanin D. D., Jovanovic D. J., Ahrenkiel S. P., Nedeljkovic J. M., J. Phys. Chem. B., 2006, 110, 25366-70.
15. Chang R., Physical chemistry for the biosciences, University Science books, 2005.
16. Chang Y. H., Liu C. M., Chen C., Cheng H. E., J. Electrochem. Soc., 2012, 159, 401-5.
17. Huang H. H., Huang C. C., Huang P. C., Yang C. F., Hsu C. Y., J. Nanosci. Nanotech., 2008, 8, 2659-66.
18. Chetibi L., Busko T., Kulish N. P., Hamana D., Chaieb S., J. Nanopart. Res., 2017, 19, 129-37.

CHAPTER 6

Titania/Cellulose composites: preparation and characterisation

6.1. Introduction

The current trend in the study of hybrid inorganic material suggests that there is a need to investigate potential sources of these materials. The cellulose obtained from maize tassel is an excellent option, giving the advantage of first discovery, since this source of cellulose has not been widely explored for the attachment of nanoparticles to form a composite. Composite materials have shown improvements in optical, thermal and mechanical properties because of the synergistic effects that arise from the physical and chemical interaction between the organic and inorganic materials [1]. There is little information on the preparation of hybrid nanocomposites that are based on natural cellulose and mineral nanoparticles [1-5]. Natural cellulose, especially nanocrystalline or nanofibrillated cellulose has unique properties such as a high Youngs modulus, dimensional stability, low thermal expansion coefficient, reinforcing potential and transparency [6-8]. The use of hybrid cellulose nanocomposites with enhanced material properties have been studied for biosensors, disposable chemical sensors, energy conversion and various other applications [6, 9-13]. The addition of metal oxides to the cellulose matrix, can improve the chemical stability, mechanical properties, conductivity and photosensitivity [6].

TiO_2 has been used in many composites as well as with cellulose and paper for use in sensors [1]. The performance of TiO_2 depends on the polymorph used, the morphology and its particle size [1, 14-17]. Nanocrystalline TiO_2 is used due to its size related properties such as surface area, band gap tuning and light scattering coefficient [1]. According to Marques *et al.* [1] and references [14, 15], nanosized TiO_2 is poorly retained and requires agglomeration promotion by polyelectrolytes or other means of retention, which decrease the optical activity and efficiency. Marques *et al*. [1] attached cellulose fibres to TiO_2 by controlled hydrolysis to create paper sheets. These could then be used in light-barrier materials. Titania supported on multiwalled carbon nanotubes (TiO_2/MWCNTs), TiO_2/N-doped MWCNTs, TiO_2/cellulose and MWCNTs-TiO_2-cellulose composites have been synthesised by methods such as mechanical mixing, sol-gel, electro-spinning and chemical vapour deposition [18-19]. These nanocomposites have been used in water purification, hydrogen evolution, CO_2 photoreduction, dye sensitized solar cells and sensors [18, 20]. The requirement for each

application has been reported to be a strong interaction between Ti, O and C from the TiO_2 and the support material which can be verified by photoluminescence which confirmed the flow of electrons from Ti to C by reducing the emission peak, which is known to reflect the reduction of charge recombination [18, 21-23]. The photocatalytic efficiency is improved with a strong interaction between TiO_2 and support material:

- Photodegradation occurs on the surface of TiO_2, which has a poor affinity for organic pollutants, hence the catalyst support gives an adsorption synergistic effect to reduce the mass transfer limitations.
- The support (cellulose) has large electron storage capacity, (one e^- for every 32 C atoms) and may accept photon-excited electrons in mixtures or nanocomposites with TiO_2, hindering the excitons recombination [24].
- The large surface area of the support allows for uniform TiO_2 dispersion and prevents the TiO_2 aggregation that limits the incidence of light on the TiO_2 active centres.
- The immobilisation on a support is essential for limited light scattering in the (nano-TiO_2 particles) and allows for recovery of TiO_2 better than TiO_2 by itself.

Since cellulose can be obtained from waste organic products, this is advantageous in that it is a highly abundant and renewable resource. The material properties such as chemical stability, conductivity, photosensitivity, mechanical and thermal properties are enhanced with the addition of metal oxides on the surface of the cellulose matrix [6, 25-30]. Various methods have been effective for the formation of hybrid nanocomposites including impregnation, sonication, hydrolysis, and blending [6]. This Chapter deals with the synthesis of TiO_2/cellulose (CT) composite. The objective was to synthesise a hybrid nanocomposite from the as synthesised cellulose from maize tassel and anatase TiO_2 reported in Chapters 4 and 5 respectively.

6.2. Preparation of TiO_2/cellulose composites (CTs)

Various ratios of TiO_2/cellulose were used as shown in Table 6.1 for the preparation of the TiO_2/cellulose composites to give a total mass of 1 gr (100 %). Cellulose was vigorously stirred in 25 mL deionised H_2O under reflux at 80 °C for two hours in a round bottom flask. The TiO_2 was sonicated in 25 mL deionised H_2O and then added to the cellulose solution. This new 50 mL solution was then stirred vigorously under reflux for 24 h at 80 °C. The solution was then allowed to boil off the excess water and was then left in open air until a dry product was obtained. The composites denoted as CT(A) through CT(F). Figure 6.1 below is a diagrammatic representation of the experimental procedure. Detailed experimental is reported in Chapter 3.

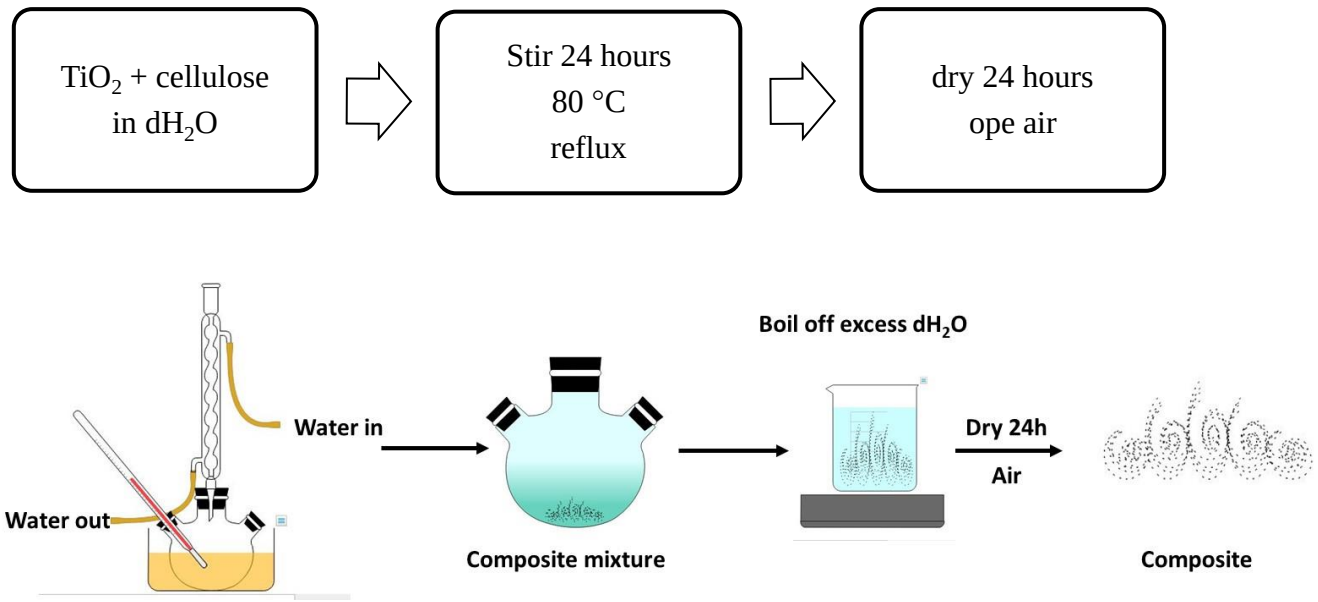

Figure 6.1: Graphic representation of the methodology of the composite's synthesis.

Table 6.1: Reaction conditions of the synthesis of the composites.

Name	% cellulose	% TiO_2	% yield
CT(A)	90	10	97
CT(B)	80	20	98
CT(C)	60	40	99
CT(D)	40	60	96
CT(E)	20	80	97
CT(F)	5	95	98

The formula used for calculating the percentage yield is shown in eq. 6.1:

$$\frac{composite\ mass\ (g)}{mass\ of\ cellulose\ (g)+mass\ of\ TiO_2(g)} * 100 = \%\ yield \qquad \text{Equation 6.1}$$

6.3. Results and Discussion

Figure 6.2 shows the difference between the untreated cellulose (CA), TiO_2, cellulose (CF) and the composite (CT(F)). As previously shown, the untreated cellulose (pure extraction from the maize tassel) and NaOH treated cellulose have the same functional groups. The composite with the largest TiO_2 loading (CT(F)), has an FTIR spectrum intermediate between that of the cellulose and anatase TiO_2. Figure 6.3 shows the FTIR spectra of the composites with different TiO_2 loadings.

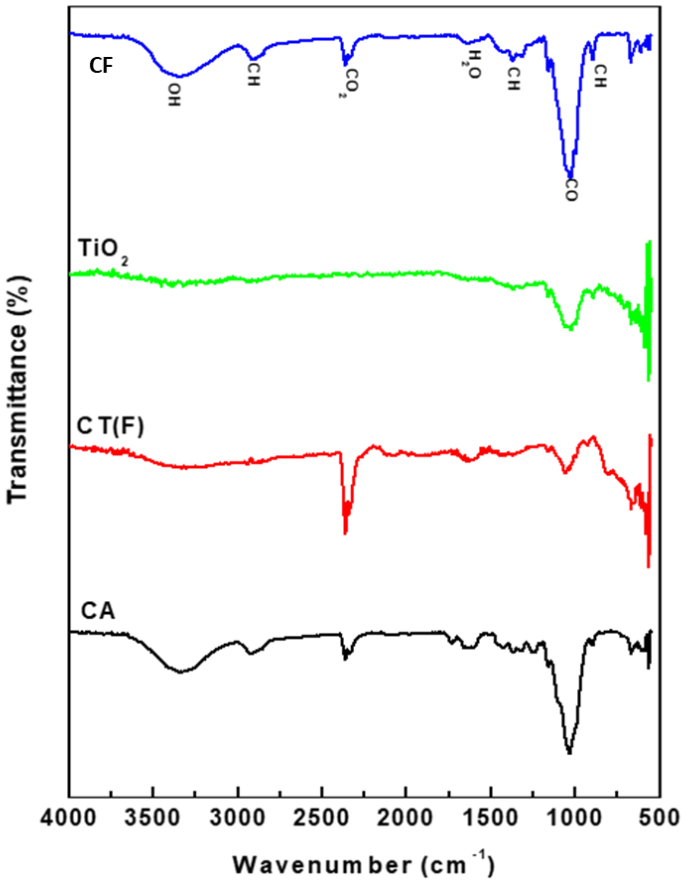

Figure 6.2: FTIR spectra of TiO_2, cellulose (CF), untreated cellulose (CA) and composite CT(F).

From the FTIR spectra, the cellulose peaks diminish with an increase in TiO_2 nanoparticle loading. The intensity of the bands decreases with an increase in TiO_2 concentration. The main

bands in the FTIR spectrum of cellulose (CF) are located at 3340 cm^{-1} (OH stretching), 2910 cm^{-1} (CH stretching), 1600 cm^{-1} (OH groups from adsorbed water), 1430 cm^{-1} (CH_2 bending), 1320 cm^{-1} (CH bending) and 1060 cm^{-1} with shoulder peaks associated with CO groups (1030 cm^{-1} CO stretching or 1160 cm^{-1} COC asymmetric stretch). The positions of these bands are influenced by the change in intra/inter molecular hydrogen bonds, which are related to changes in the chemical surface groups and crystallinity [30]. The peak at 898 cm^{-1} is the β-1-4-glycosidic link associated with COC stretching. The TiO_2, TiOH is masked by the CH_2 peak around 1396 cm^{-1} [31].

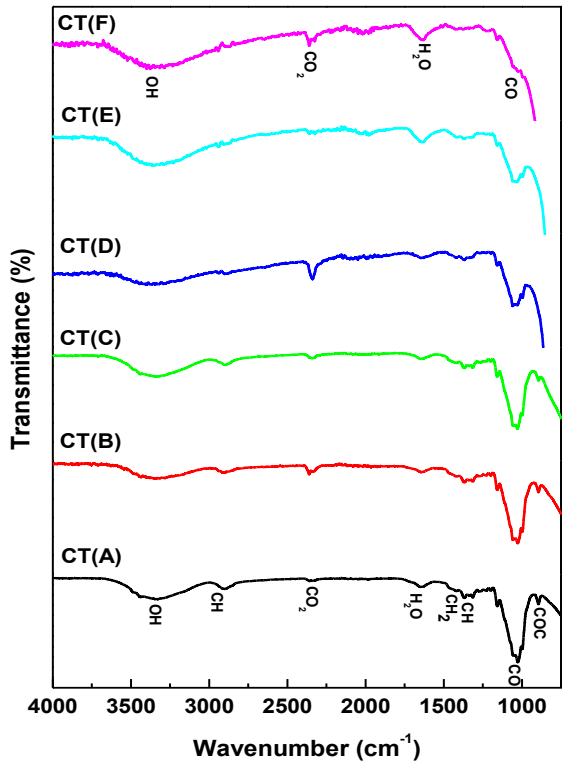

Figure 6.3: FTIR spectra of the composites with different TiO_2 loadings, CT(A) - CT(F) corresponding to 10% - 95% loadings.

Figure 6.4 shows the XRD patterns of the synthesised composites CT(A) - CT(F). The composite CT(A) and CT(B) have the cellulose (110) and (002) peaks denoted by (*) due to the low surface coverage of cellulose fibres byTiO_2. As the concentration of TiO_2 is increased, the cellulose peaks diminished, leaving only the anatase TiO_2 peaks due to larger coverage of the cellulose fibres by TiO_2 nanoparticles. The TiO_2 anatase (101), (103), (200), (105) and (213) peaks are visible in all of the composite patterns.

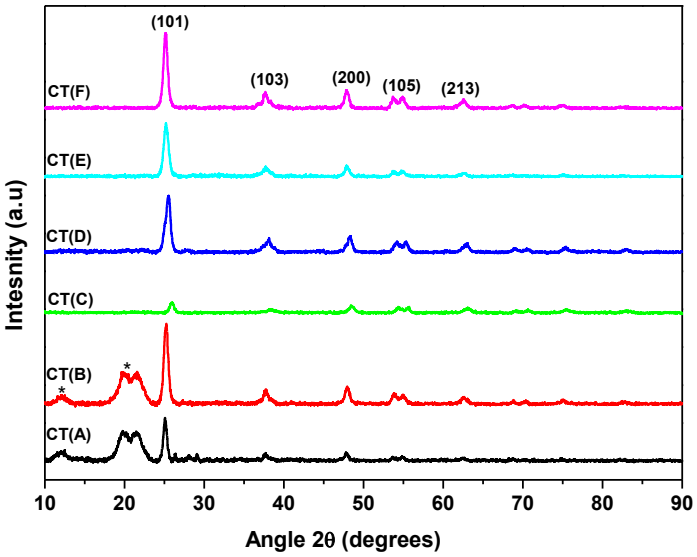

Figure 6.4: X-ray diffractograms of the composites CT(A-F).

The EDX spectra of CT(A), CT(B), CT(E) and CT(F) are shown in Figure 6.5. The elements of Ti, O and C are confirmation of the presence of TiO_2 attached to the cellulose fibres. The elements Au and Pd are due to the pre-coating required to prevent charging under the electron microscope. Some of the carbon presence can also be attributed to the carbon tape used to load the sample before SEM analysis.

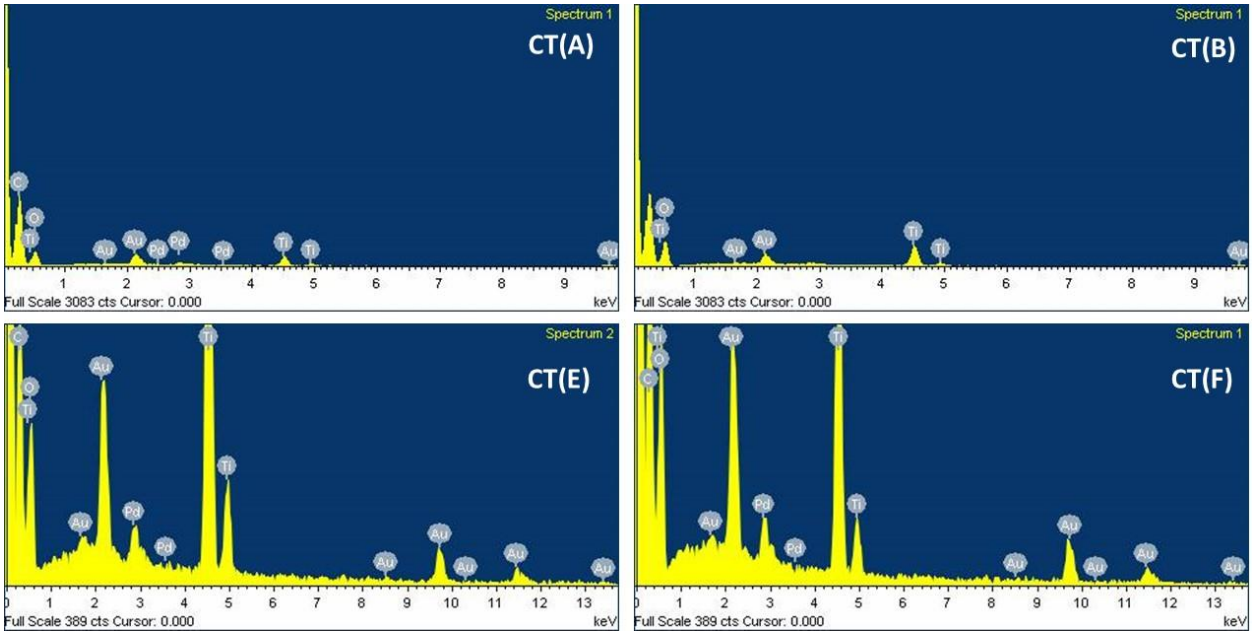

Figure 6.5: EDX spectra of TiO_2/cellulose composites CT(A), CT(B), CT(E) and CT(F).

Figure 6.6 shows the SEM images of composites CT(A) - CT(F) and reveals that a larger area of the cellulose fibres is covered with TiO_2 nanoparticles as the concentration of TiO_2 increased. The agglomeration of TiO_2 at higher concentration loading of TiO_2 on cellulose is expected.

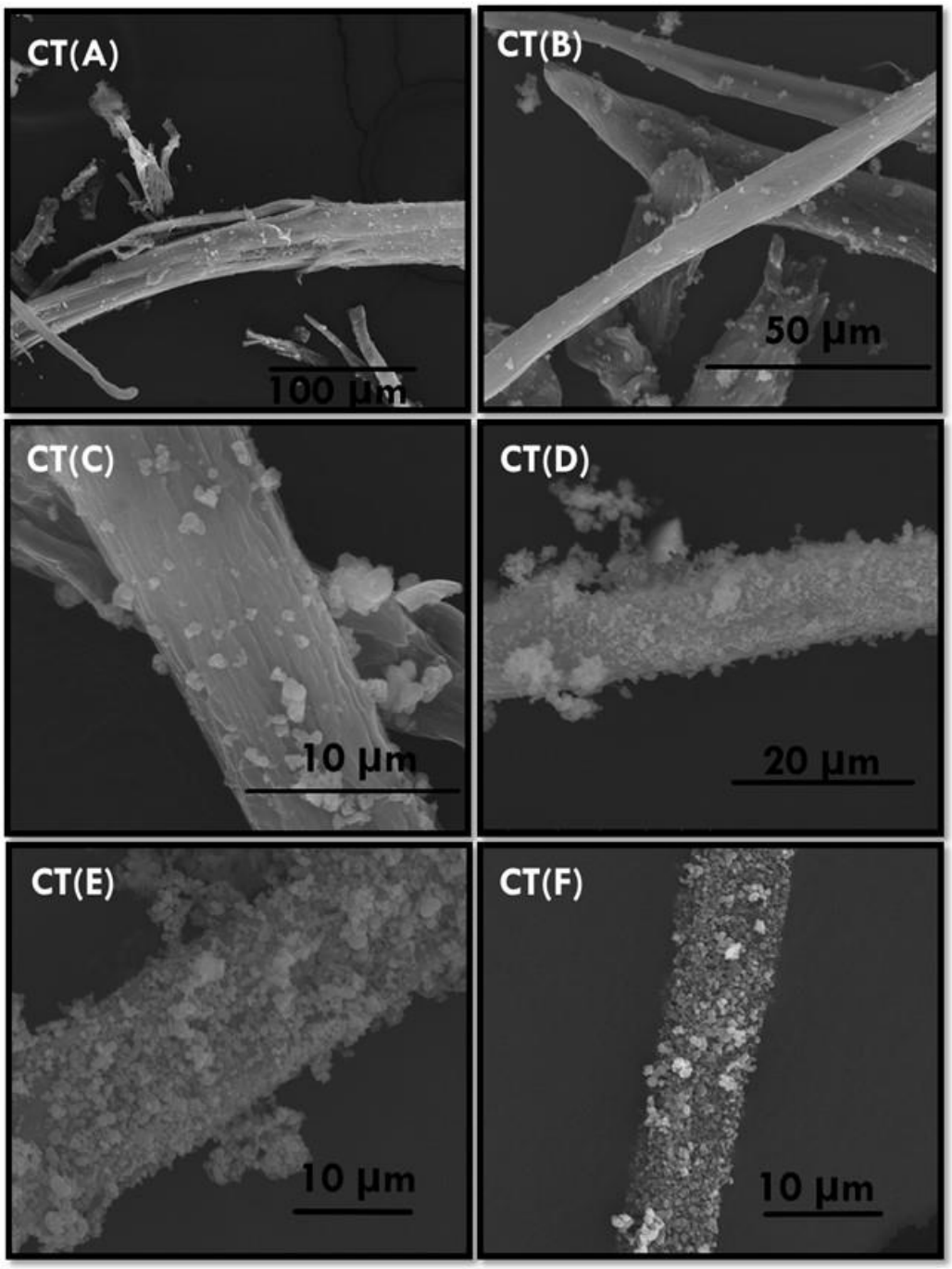

Figure 6.6: SEM images of TiO_2/cellulose composites CT(A) - CT(F).

Figure 6.7 shows the TEM images of composites CT(A) - CT(F) and confirmed that TiO_2 was supported on the cellulose fibres. This agrees with the SEM data presented in Figure 6.6. The higher the concentration of TiO_2 loading, the more coverage on the cellulose fibres. The agglomeration of TiO_2 at higher concentration loading of TiO_2 on cellulose is expected due to the nature of TiO_2.

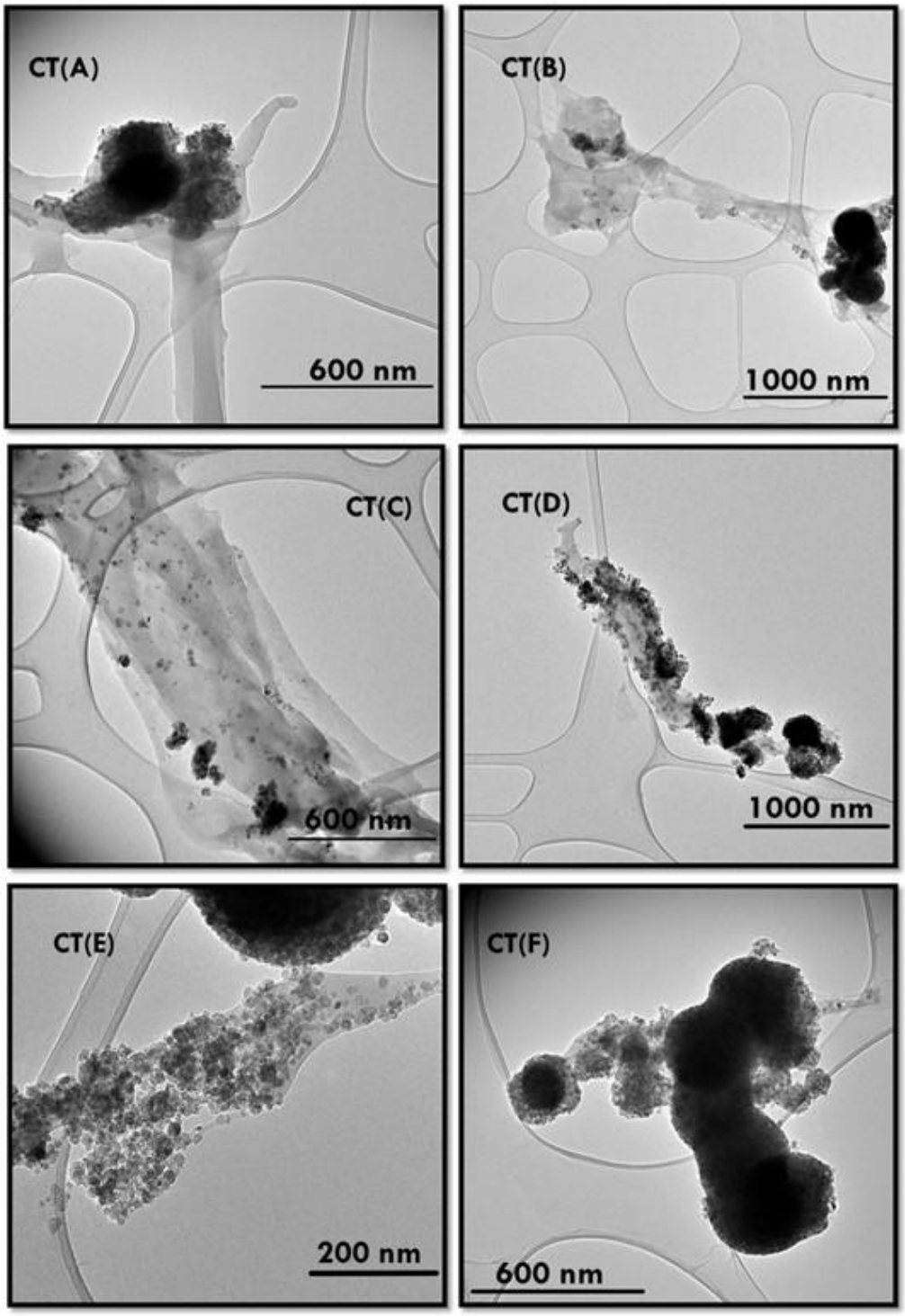

Figure 6.7: TEM images of TiO_2/cellulose composites CT(A) - CT(F).

Figures 6.8 shows the TGA and derivative TGA curves of the composites CT(A) - CT(F). The thermal decomposition of cellulose occurred in three stages, rather similar to CT(A). The first stage, the peak at 75 °C, below 100 °C is the loss of adsorbed water molecules on the material. The second stage is the peak around 350 °C, the decomposition of cellulose chains in the composite to give carbonised material and the third stage is the peak ~ 490 °C, attributed to the combustion of cellulose. A trend can be seen with an increase in TiO_2 loading. The TGA profile of the composite materials show less weight loss with an increase in TiO_2 loading on the cellulose. This is because only moisture and the cellulose mass is lost during the decomposition process, while the TiO_2 mass residue remains after the process is complete. The weight loss below 230 °C is the dehydroxylation of TiO_2 with organics from cellulose. The lower thermal stability of cellulose in the composite might be due to the catalytic character of TiO_2 as well as intermolecular interactions of the cellulose polymer chain with hydroxyl groups in TiO_2. The mass loss decreased with a decrease in cellulose content. From the derivative curves of the TGA plot, the highest weight loss between 300 - 400 °C is attributed to the charring of polysaccharides in cellulose [32]. The decomposition curves indicate that with a higher percentage of TiO_2 attached to the cellulose, the more stable are the composites. This is because there are less organics to be lost with a higher TiO_2 loading on the cellulose substrate. Hence CT (E) and CT (F) decompose at higher temperature due to the higher TiO_2 loading of the composite.

The total mass loss at temperatures up to 490 °C reveals that the percentage of cellulose in the respective composites and the residual percentage weight gives an approximate amount of TiO_2 present in the composite. From the TGA results, the content of TiO_2 nanoparticles in the composite was obtained to be ~10, ~19.8, ~37, ~58, ~79 and ~94 weight % of the composites CT(A), CT(B), CT(C), CT(D), CT(E) and CT(F) respectively. This suggests that the TGA results are in close agreement with the cellulose and TiO_2 ratios used during the synthesis of the composites.

.

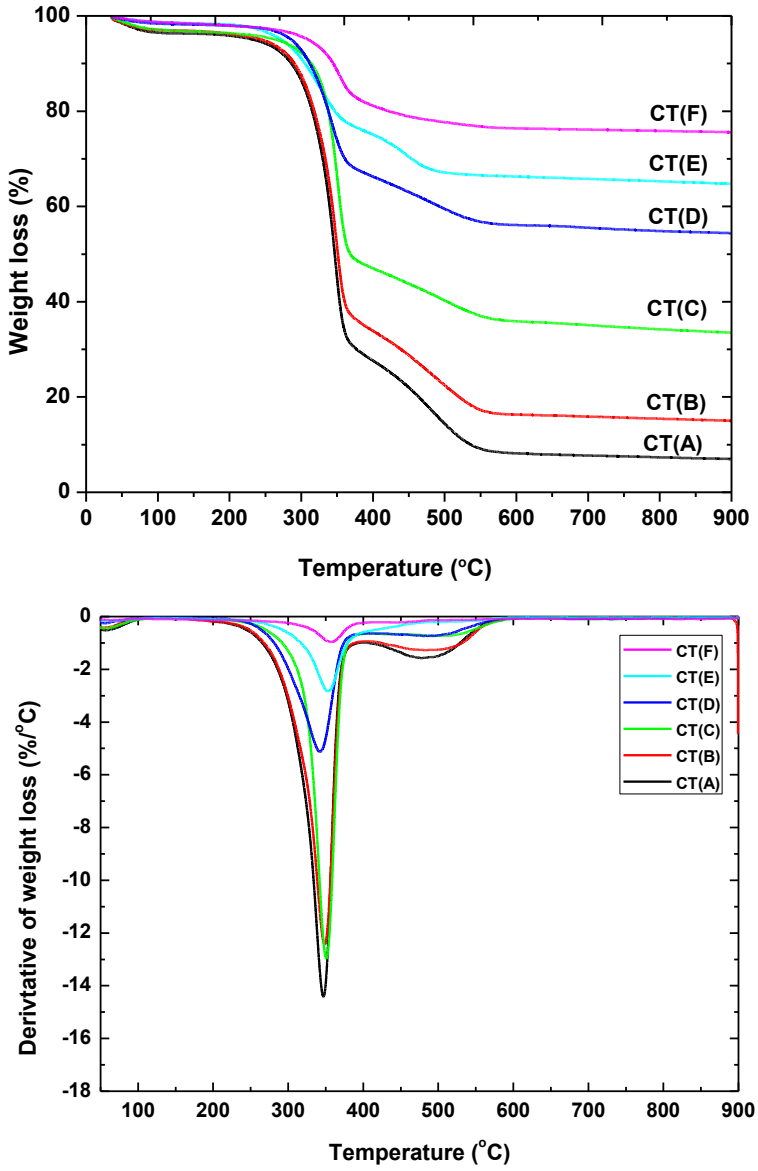

Figure 6.8: TGA and DTGA thermograms of the TiO_2/cellulose composites CT(A) - CT(F).

The interaction mechanism of TiO_2 on cellulose is not fully understood but may be a physical interaction, by adsorption to the fibre surface or mechanical entrapment in the cell wall structure or possibly chemisorption through the surface functional groups of the cellulose. Physisorption may be unlikely since mechanical agitation does not dislodge the TiO_2 particles from the cellulose [1]. Since the TiO_2 particles are retained in extensions of the fibre, there may be electrostatic or a chemical interaction between the polysaccharide cellulose and glucuronoxylan of the fibre and TiO_2 particle surfaces. Other explanations include adjacent hydroxyl groups in the anhydroglucose or anhydroxylose units, from the carboxyls in uronic

acid moieties, as Lewis basic sites for the complexation of cationic Ti (IV) species, to act as nucleation initiators [1]. The method of formation of the composite does suggest the interaction between the cellulose and TiO_2 to be a polar interaction. The synthesis involved mild heating conditions under reflux and mechanical agitation.

6.4. Conclusion

Maize tassel extracted cellulose fibres were successfully used to form composites with the anatase phase TiO_2. The composites were prepared using a controlled hydrolysis method. The thermal stability of the composite was improved with an increase in the TiO_2 content and a decrease in cellulose content. The XRD, SEM and TEM images confirmed the presence of an increased percentage of TiO_2 attached to the cellulose fibres with increasing TiO_2 loading. In the XRD, the distinct peaks of cellulose diminished due to the higher TiO_2 content. FTIR analysis confirmed the decrease in cellulose peak intensity with an increase in TiO_2 concentration. The attachment of TiO_2 to cellulose would allow for the easy collection of the catalyst after water treatment. These composites will then be used in the photodegradation of methyl orange dye.

6.5. References

1. Marques P. A. A. P., Trindade T., Neto C. P., Compos. Sci. Technol., 2006, 66, 1038-44.
2. Goutailler G., Guillard C., Daniele S., Hubert-Pfalzgraf L. G., J. Mater. Chem., 2003, 13, 342-6.
3. Kongdee A., Bechtold T., 2004, 60, 137-42.
4. Suber L., Foglia S., Ingo G. M., Boukos N. M., Appl. Organomet. Chem., 2001, 15, 414-20.
5. He J., Kunitake T., Nakao A., Chem. Mater., 2003, 15, 4401-6.
6. Khan A., Abas Z., Kim H. S., Kim J., Sensors, 2016, 16, 8-12.
7. Yun G. Y., Yun K. J., Kim J. H., Kim J., J. Nanosci. Nanotechnol., 2011, 11, 570-73.
8. Kalia S., Boufi S., Celli A., Kango S., Colloid. Polym. Sci., 2014, 292, 5-31.
9. Gindl W., Keckes J., Polymer, 2005, 46, 10221-25.
10. Mahadeva S. K., Kim J., Sci. Technol. Adv. Mater., 2011, 12, 055006.
11. Siro I., Plackett D., 2010, 17, 459-94.
12. Kumar A., Gullapalli H., Balakrishnan K., Botello-Mendez A., Vajtai R., Terrones M., Ajayan P. M., Small, 2011, 7, 2173-78.
13. Zakirov A.S., Yuldashev S.U., Cho H. D., Lee J. C., Kang T. W., Khamdamov J. J., Mamadalimov A. T., J. Korean Phys. Soc., 2012, 60, 1526-30
14. Neimo L., Papermaking science technology, Papermaking chemistry, Helsinki, Finland: Fapet Oy, 1999, 4.
15. Roberts J. C., Paper chemistry, Glasgow, UK: Back Academic & Professional, 1996, 2.
16. Chu R., Yan J., Lian S., Wang Y., Yan F., Chen D., Solid State Commun., 2004, 130, 789-92.
17. Dong W., Pang G., Shi Z., Xu Y., Jin H., Shi R., Mater. Res. Bull., 2004, 39, 433-8.
18. Mathebula X., Photocatalytic degradation of methyl violet in water using TiO_2/cellulose-N-MWCNTs, Dissertation, The University of the Witwatersrand, 2018, 100-11.
19. Papo C., Tetana Z. N., Franklyn P., Mhlanga S. D, Mater. Res., 2012, 28, 440-48.
20. Jiménez Reinosa J., Leret P., Álvarez-Docio L. M., Del Campo A., Fernández J. F., Boletin de la Sociedad Espanola de Ceramica y Vidrio, 2016, 55, 55-62.
21. Su R., Dimitratos N., Liu J., Carter E., Althahban S., Wang X., Shen Y., Wendt S., Wen X., Niemantsverdriet J. W., Iversen B., Kiely C. J., Hutchings G. J., Besenbacher F., ACS Catal., 2016, 6, 4239-47.
22. Ramoraswi N. O., Ndungu P. G., Nanoscale Res. Lett., 2015, 10, 427-33.

23. Yao Y., Li G., Ciston S., Lueptow R. M., Gray K. A., Environ. Sci. Technol., 2008, 42, 4952–57.
24. Dong H., Zeng G., Tang L., Fan C., Zhang C., He X., He Y., Water Res., 2015, 79, 128-46.
25. Kim J. H., Mun S., Ko H. U., Yun G. Y., Kim J., Nanotechnology, 2014, 25, 1-9.
26. Chen Y., Jang S. D., Kim J., Sens. Lett., 2012, 10, 748-53.
27. Kim G. H., Ramesh S., Kim J. H., Jung D., Kim H. S., J. Nanosci. Nanotechnol., 2014, 14, 7495-501.
28. Orts W. J., Shey J., Imam S. H., Glenn G. M., Guttman M. E., Revol J. F., J. Polym. Environ., 2005, 13, 301-6.
29. Halamus T., Wojciechowski P., Bobowska I., Polym. Adv. Technol., 2008, 19, 807-11.
30. Gutierrez J., Tercjak A., Algar I., Retegi A., Mondragon I., J. Colloid Interface Sci., 2012, 377, 88-93.
31. Oliveira A. C. de M., dos Santos M. S., Brandao L. M. S., de Resende I. T., Leo I. M., Morillo E. S., Verga R. M. N., Fierro J. L. G., Egues S. M.da S., Figueiredo R. T., Int. J. Hydrogen Energ., 2017, 9, 1-8.
32. Virkutyte J., Jegatheesan V., Varma R. S., Bioresour. Technol., 2012, 113, 288-93.
33. Hamad H., Bailon-Garcia E., Morales-Torres S., Carrasco-Marin F., Perez-Cadenas A. F., Maldonado-Hodar J., J. Enviro. Chem. Eng., 2018, 4, 5032-41.

CHAPTER 7

The use of the TiO_2/cellulose composites in photocatalytic degradation of methyl orange

7.1. Introduction

Wastewater from industry is a problem for the environment. The discharged water usually contains dyes that are toxic. Chemicals such as azo dyes, herbicides and pesticides are present in rivers and lakes and are suspected of disrupting endocrine systems [1]. The release of dye in wastewater is a source of non-aesthetic pollution and eutrophication and can release dangerous by-products due to oxidation, hydrolysis, or other chemical reactions. The dyes in wastewater can reduce the amount of light penetration in contaminated water [1, 2]. Water treatment processes such as sedimentation, filtration, chemical and membrane technologies have high operational costs and create secondary pollutants [3]. Some treatment methods include physical techniques such as adsorption, ultrafiltration, reverse osmosis, flocculation, coagulation by chemical agents and ion exchange. These methods transfer the organic compounds from water to another phase, which create secondary pollution that requires other methods of treatment. These methods then add to the cost of the clean-up process. Some other treatment methods include microbiological or enzymatic decomposition [4], ozonation [5], biodegradation [6] and advanced oxidation such as Fenton and photo-Fenton catalysis [7, 8] and H_2O_2/UV processes [1, 9, 10]. The use of photocatalysis has been of interest in the removal of dye from wastewater because of the complete mineralisation of target pollutants [1].

TiO_2 is the most studied photocatalyst to date. It is non-toxic, cheap, photoreactive, biologically and photochemically inert, photostable with a strong redox ability. TiO_2 is effective in the UV region of the spectrum with a band gap of 3.0 - 3.2 eV. In an attempt to lower the band gap, doping of TiO_2 has been considered, however the products are very unstable. The photocatalytic reaction of TiO_2 requires UV radiation. This process relies on the excitation of electrons by UV radiation, caused by light absorption. UV light influences the loss or gain of electrons and promotes degradation of organic pollutants to form harmless by-products such as CO_2, H_2O and other mineral acids, as well as reduce heavy metal ions into less toxic metal ions [11]. The hydroxyl radicals that form on illuminated TiO_2 surfaces are strong oxidants which

degrade organic pollutants [11]. The degradation reaction of organic compounds that are catalysed by TiO_2 can be written as [11]:

$$TiO_2 + h\nu \rightarrow TiO_2\ (e^- + h^+) \qquad \text{Equation 7.1}$$

h^+ or hole will react with a water molecule to form hydroxyl radical:

$$h^+ + H_2O \rightarrow \cdot OH + H^+ \qquad \text{Equation7.2}$$

This hydroxyl radical is a non-selective oxidizing agent and initiates reactions of organic compounds to convert them to simpler and smaller compounds. Hence, for TiO_2 with organic compounds

$$C_cH_hO_o + [\frac{(h-2_o)}{4} + n]O_2 \rightarrow TiO_2, h\nu \rightarrow cCO_2 + \frac{h}{2H_2O} \qquad \text{Equation 7.3}$$

Some e^- may recombine with holes reducing the extent of the photodegradation process, hence, to prevent this, an electron capturing agent is usually added to the system to delay recombination [11]. The performance of TiO_2 photo-catalytically depends on the bulk energy band structure and its surface properties. A larger surface area per mass has better photocatalytic activity [12]. The synthesis process affects the type and density of states of TiO_2. The calcination temperature and atmosphere used in the synthesis of TiO_2 also affect TiO_2 activity [12]. Powdered TiO_2 may reduce the efficacy of photocatalysis since the powder may be difficult to recover after dispersion. Also, the dispersed TiO_2 may increase turbidity of the solution, hampering UV radiation from activating the dispersed photocatalyst particles. A method of avoiding this is by combining the chosen photocatalyst (TiO_2) with a support such as chitosan, cellulose or carbon structures [11]. In the photocatalytic degradation of dyes, the following operating parameters should be considered: pH of the degradation solution, pH of precursor solution (solution during preparation of catalyst), oxidising agent, catalyst calcination temperature, dopant content and the catalyst loading [1]. Wastewater may contain a mixture of pollutants which may compete for the active sites on TiO_2 and deactivate the photocatalyst, or they may act as light screens to reduce the efficacy of the photocatalyst [3].
Methyl orange (MO) is an azo (-N=N-) group compound with a diethylamine group in one of the aromatic rings [11]. Azo dyes can be divided into monazo, diazo or triazo depending on the number of azo bonds [12]. Azo dyes are found in categories such as acid, basic, direct disperse,

azoic and pigments [12]. Methyl orange is ionised in water and produces a negatively charged chromophore. This makes MO an anionic or acidic dye. The structure of MO is shown in Figure 7.1 along with xylene cyanol [18] which is the dye solution that was used in this study. The site near the chromophore (N=N and aryl groups) is the area of attack in photocatalytic degradation which leads to fading of the dye [12]. Both UV light and photocatalyst are required for the effective destruction of organic dyes [12]. The chemical structure of the organic dye has an impact on the reactivity of TiO_2 [12-16]. Adsorption of the target molecule on TiO_2 should be considered as an important step in photocatalysis [12]. Methyl orange has favourable geometry and dimensions for adsorption; the SO^{3-} attaches to the surface of the TiO_2; Ti (IV) centres and assumes bidentate coordination via the two sulfonic O atoms [12]. This process is then followed by substitution of a surface coordinated hydroxyl moiety. The overlap of 3d orbitals from the Ti (IV) and the 2p orbitals of oxygen allow for strong covalent bonds in Ti-O formation. Due to MO complexation, many surface sites are passivated, causing catalyst deactivation and depleting terminal hydroxyls that are grouped on the surface. This mechanism can remain in operation over a long period since the primary by-products of MO have sulfonic groups [12]. Trabelsi *et al.* [3] studied the photodegradation products and identified them, according to their molecular ion and mass spectrum fragmentation. The mineralisation of MO produced CO_2, H_2O, SO_2^{2-}, NH^{4+} and NO^{3-} [3, 17].

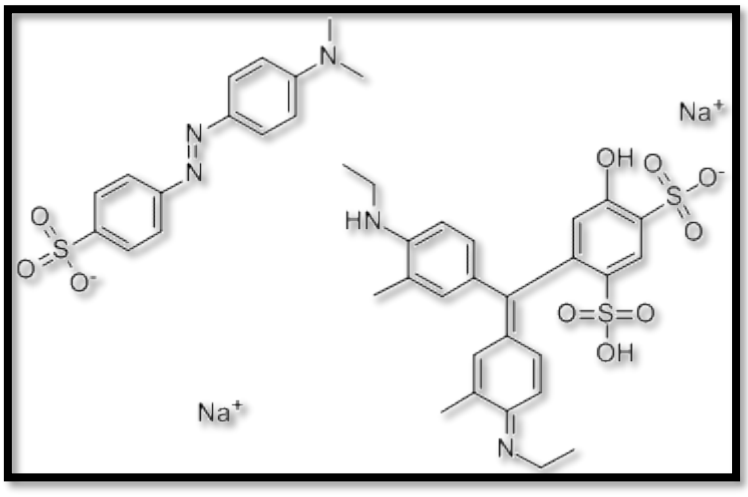

Figure 7.1: The molecular structures of methyl orange in xylene cyanol solution [18].

Hybrid inorganic and organic materials such as TiO_2/cellulose make up a new class of nanocomposites that display enhanced optical, thermal and mechanical properties because of synergistic effects from their physical and chemical properties [19, 20]. Cellulose can act as

both a support for TiO_2 and a source of different chemical products from the decomposition of cellulose in the presence of TiO_2 under UV-Vis radiation [20, 21]. Cellulose has a super fine network which can disperse the TiO_2 and improve particle stability as well as control the growth of TiO_2 on the surface [20, 22]. Fajriati *et al.* [11] used TiO_2-chitosan nanocomposite as a photocatalyst and found that photodegradation of dye molecules catalysed by the nanocomposite showed higher activity than bulk TiO_2. Dye molecules that are easily adsorbed on the surface of the catalyst are degraded more. Because of the positive charge of the photocatalyst, the anionic MO was adsorbed and degraded easier than cationic methyl blue [11]. The aim of this study was to use some of the TiO_2/cellulose composites from Chapter 6 for the photocatalytic degradation of methyl orange in xylene cyanol.

7.2. Photocatalytic activity tests

Adsorption and photocatalytic parameters are summarised in table 7.1. Aliquots (3 mL) of both adsorption and photocatalytic samples were taken every 15 minutes and examined using Uv-Vis spectroscopy. The detailed method can be found in chapter 3. The dye concentration was measured using a UV-Vis spectrometer. The efficiency of the photodegradation was determined using Eq. 7.4:

$$\eta = \frac{C_o - C_t}{C_o} * 100\ \% \qquad \text{Equation 7.4}$$

Where η is the photocatalytic efficiency, C_t is the concentration after time t and C_o is the initial concentration of the dye. Modified or screened methyl orange used here is an indicator that contains xylene cyanol solution and methyl orange solution which changes from grey-violet to green, depending on the basicity of the solution. Xylene cyanol is also used as a tracking dye. The pH of each solution (2-14) was controlled using NaOH or H_2SO_4 before placing under the solar simulator.

Table 7.1: Parameters of TiO_2/cellulose composites adapted from Chapter 6.

Name	% cellulose	% TiO_2
CT(A)	90	10
CT(B)	80	20
CT(C)	60	40
CT(D)	40	60
CT(E)	20	80
CT(F)	5	95

7.3. Results and Discussion

The UV-Vis spectra (all Figures that follow) of methyl orange show peaks at 273 nm associated with the benzene ring and 465 nm due to the azo link. The peak at 625 nm is due to the xylene cyanol [3].

7.3.1. Adsorption of methyl orange on composite photocatalyst

According to Kumar and Pandey [10], photocatalysis depends on the adsorption of dye on to the surface of the photocatalyst. The amount of dye adsorbed on the catalyst contributes to photocatalysis and not the one that is in the bulk solution. The adsorption will then depend on the initial concentration of the dye [10]. Figure 7.2 shows the colour of the adsorbed solution aliquots using CT(C) and CT(F) catalysts only after 90 minutes of stirring the solution in the dark. This can be evidenced by the UV-Vis spectra corresponding to the adsorption of methyl orange using CT(C) and CT(F) catalyst. The same experiments were also done on CT(A), CT(B), CT(D) and CT(E). All photocatalysts exhibited similar behaviours to CT(C) catalyst, i.e. negligible adsorption.

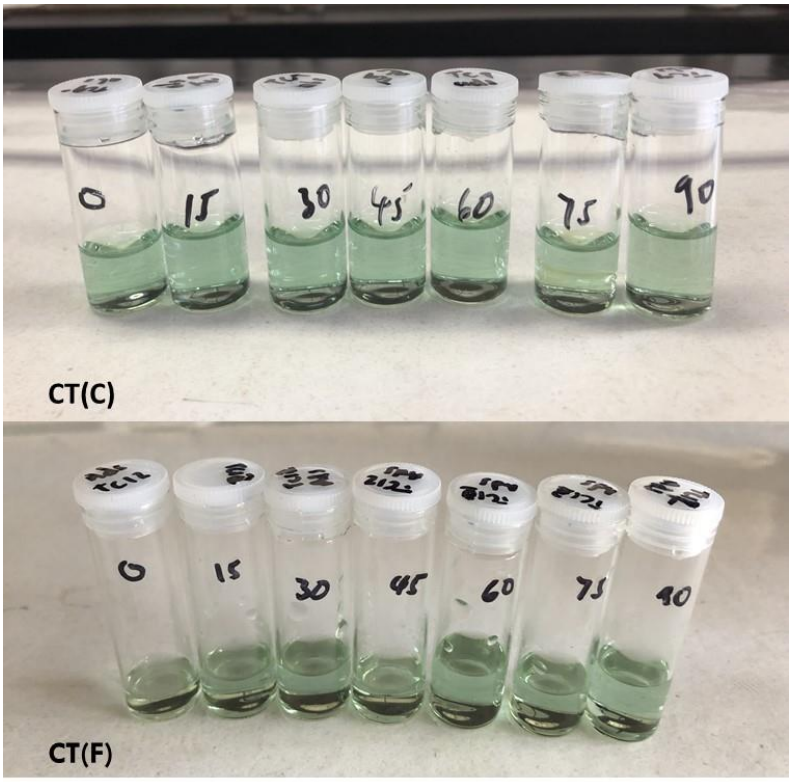

Figure 7.2: Images showing the colour of 5 ppm methyl orange with composites CT(C) and CT(F) during adsorption studies in aliquots taken over 0 - 90 minutes.

Figure 7.3 shows the UV-Vis spectra of the adsorption studies for composites CT(A) - CT(F) using 5 ppm MO in xylene cyanol and 10 mg of each composite. Kumar and Pandey [10] also reported that the extent of dye adsorption depends on the initial concentration of the dye, the nature of the dye, the surface area of the photocatalyst and the pH of the solution which determines the surface charge of the photocatalyst. The adsorption occurs when the pH of the solution is at the isoelectric point (point of zero charge). This makes the surface of the photocatalyst positively charged below the isoelectric point and negatively charged above it [10]. The amount of dye adsorbed to the surface of each of the composites were negligible. With the increase in time, there were no acceptable changes to the dye concentration, hence adsorption was minimal.

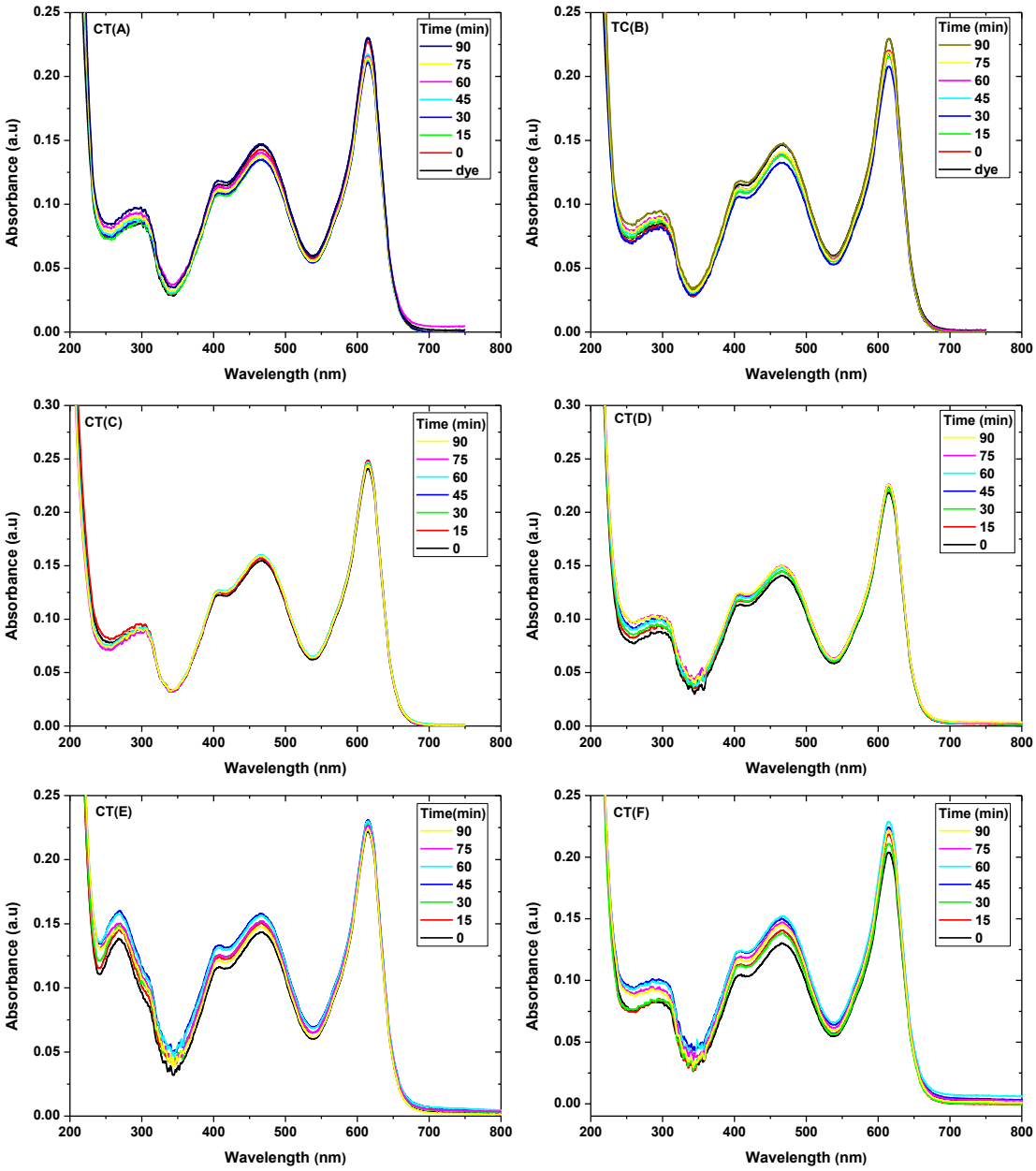

Figure 7.3: The UV-Vis spectra of CT(A) - CT(F) in 5 ppm MO during the adsorption study for aliquots taken over 0 - 90 minutes.

7.3.2. Effect of the nanocomposites on the degradation of MO

Decolourisation of an aqueous solution containing an azo dye MO was achieved by using radiation and TiO_2/cellulose photocatalysis. The disappearance of colour and concentration changes were observed. The codes of the composites and composition used can be found in Table 7.1 for reference. The trend observed in Figure 7.5 is that with an increase in the TiO_2 catalyst concentration, the degradation and decolourisation of MO is achieved faster. Cellulose acts as a scaffold for the attachment of the TiO_2 catalyst to provide a large surface area for the

catalyst. This large surface area allows for more exposure and interaction with the dye, giving a faster rate of degradation and also slows the rate of electron hole recombination. The composite with the highest concentration of TiO_2 catalyst CT(F) showed the best performance during the degradation of MO after 90 minutes when compared to the other composites, Figure 7.5. When compared to pure (100%) TiO_2 catalyst, the composite CT(F) also degraded the MO to a greater extent. This can be explained in that dye molecules may be adsorbing on to the surface of the cellulose or, cellulose may also act as a catalyst to degrade the MO. The TiO_2 catalyst surface in CT(F) was also exposed to a greater degree in the presence of cellulose. This is evident in the composite CT(F) which has the greatest ability to degrade MO in the presence of light. The colour changes can be seen in Figure 7.4 where the green MO due to the basic xylene cyanol changes to clear after 45 minutes.

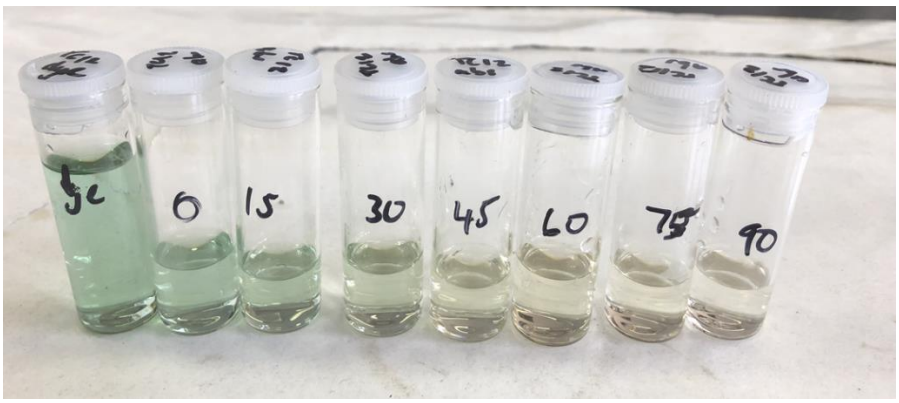

Figure 7.4: The colour degradation of 5 ppm MO from 0 - 90 minutes irradiation using CT(F).

After the 5 minutes of stirring to achieve adsorption equilibrium, the difference between the dye and initial concentrations are shown in Figure 7.5 and the % efficiency vs. time plot in Figure 7.6, tabulated in Table 7.2. This can be explained by adsorption of the dye onto the cellulose. Also, the composite had a greater degradation efficiency compared to the TiO_2 alone. This shows that the composite catalyst CT(E) and CT(F) was better at degrading the methyl orange than TiO_2 on its own and that the largest TiO_2 loading on cellulose CT(F) was best at degradation. This may be due to a larger area being exposed to the dye by the composite compared to the TiO_2. The lower TiO_2 loading on cellulose in CT(A) and CT(B) did not have the ability to degrade the methyl orange, understandable since 10 mg in 50 mL of 5 ppm methyl orange with small % TiO_2 loading is not enough to degrade the solution. Both CT(E) and CT(F) displayed higher photodegradation efficiencies of 100 % after 60 minutes.

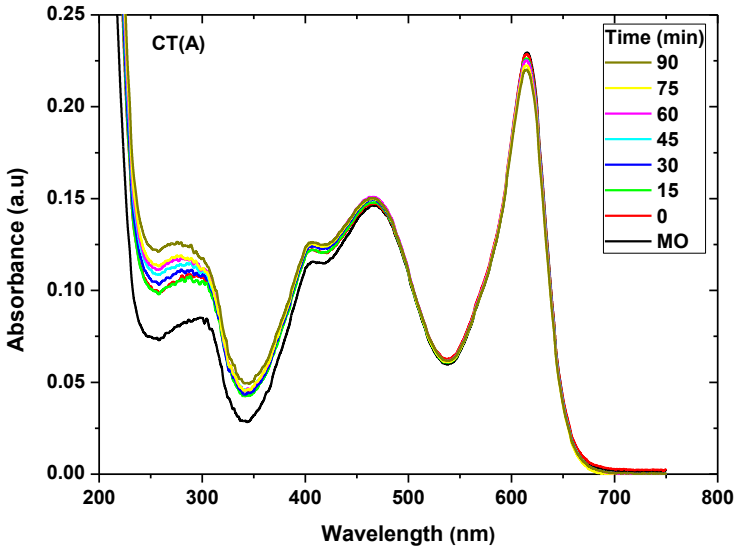
CT(A)
Time (min)
90
75
60
45
30
15
0
MO
Absorbance (a.u)
Wavelength (nm)
0.25
0.20
0.15
0.10
0.05
0.00
200
300
400
500
600
700
800

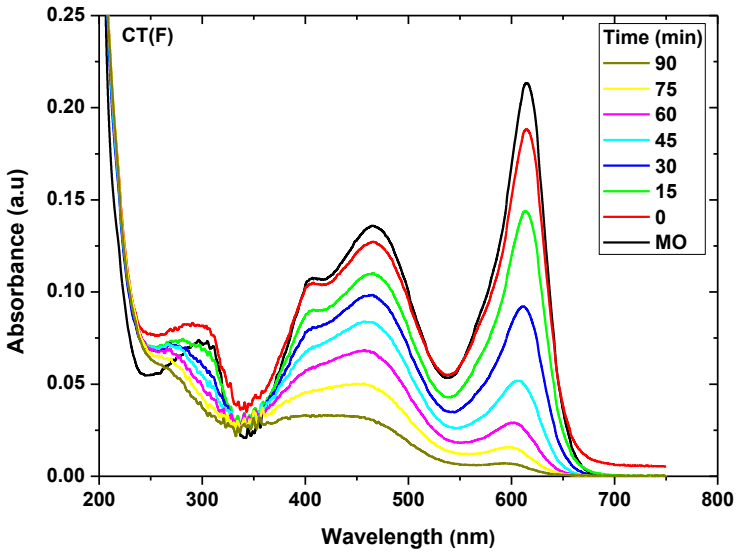
CT(F)
Time (min)
90
75
60
45
30
15
0
MO
Absorbance (a.u)
Wavelength (nm)
0.25
0.20
0.15
0.10
0.05
0.00
200
300
400
500
600
700
800

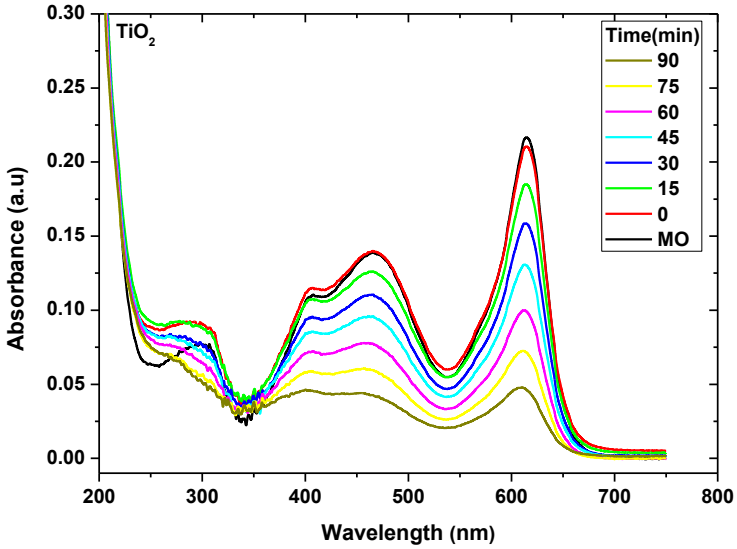
TiO2
Time(min)
90
75
60
45
30
15
0
MO
Absorbance (a.u)
Wavelength (nm)
0.30
0.25
0.20
0.15
0.10
0.05
0.00
200
300
400
500
600
700
800

Figure 7.5: The UV-Vis spectra of CT(A), CT(F) and TiO_2 in 5 ppm MO for 0 - 90 minutes irradiation.

Konstantinou and Albanis [7] found that the rate of photodegradation of azo dye was directly proportional to catalyst concentration. They also found that there is a catalyst concentration limit, above which, decreases the rate of photocatalysis. An increase in the amount of photocatalyst increases the number of active suites on the photocatalyst surface, this increases the hydroxide and superoxide radicals produced. If the concentration of catalyst increases above the optimum value, photodegradation decreases due to the interception of light by the suspension [1, 23]. Also, an increase in photocatalyst results in agglomeration of the catalyst particles, voiding a part of the photocatalyst surface for photodegradation [1, 24]. The amount of TiO_2 in the composite affects the photodegradation. The photodegradation increased with an increased amount of TiO_2, a feature of heterogenous photocatalysis. As the TiO_2 content in the composite increased, the photoactivity was low until 20 % TiO_2 loading, then reactivity increased sharply from 60-95 wt. % TiO_2, CT(D)- CT(F). However, the efficiency of TiO_2 was higher than CT(A), CT(B), CT(C) and CT(D) due to the trapping of more light by the anatase phase of pure TiO_2. The increase in methyl orange degradation with the increase in TiO_2 loading could be due to the increase in the number of active sites, by way of increased surface area, which resulted in more effective interactions and created more hydroxyl radicals for participation in MO discolouration. However, above a certain threshold limit and higher agglomeration of TiO_2 particles, the solution can become turbid and block UV radiation, hindering the photocatalytic process [10, 25].

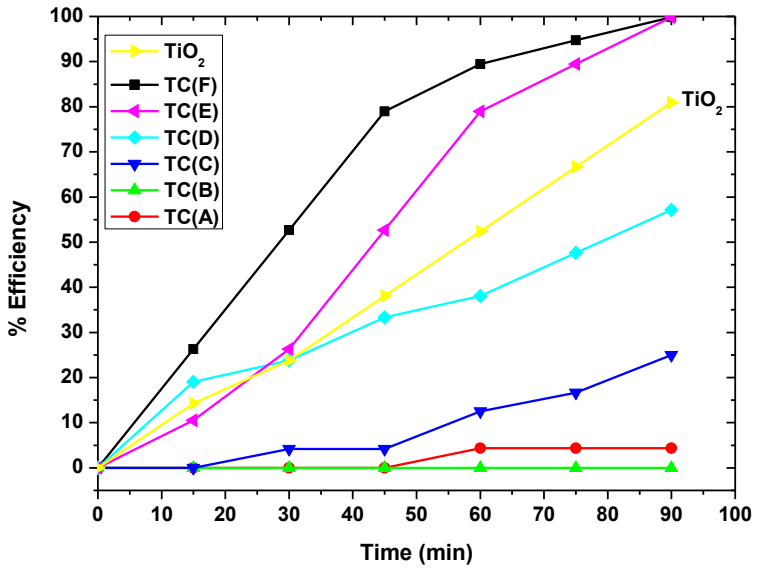

Figure 7.6: The % efficiency of CT(A) - CT(F) and TiO_2 in 5 ppm MO for 0 - 90 minutes irradiation.

Table 7.2: The efficiency of CT(A) - CT(F) and TiO_2 in degrading 5 ppm MO.

Sample	% Efficiency
CT(A)	4
CT(B)	0
CT(C)	25
CT(D)	57
CT(E)	100
CT(F)	100
TiO_2	81

7.3.3. Variation of dye concentration

Investigation in the range (5-20 ppm) on the decolourisation of MO shows the influence of initial dye concentration when using 10 mg of CT(F) which is 95:5 of TiO_2/cellulose (Figure 7.7). CT(F) was still efficient up to 10 ppm MO for complete MO degradation after 90 minutes. The composite would still degrade the MO to completion if allowed more time since the trend is going towards a 0% concentration even up to 20 ppm of MO. The percentage efficiency presented in Figure 7.8 shows a decrease in efficacy of the catalyst with an increase in dye concentration. A decrease in the intensity of the colour was also observed with an increase in the initial dye concentration. After 90 minutes, 100% degradation was achieved for 5 ppm MO. When 10 ppm was used, 90% degradation was achieved. Upon increasing the MO to 15 ppm, 83% degradation was achieved. An increased adsorption of dye molecules may suppress the formation of active $OH^{\cdot}$ radicals. Also, the screening effect of UV light may be responsible. This effect is increased with a larger dye concentration (colour intensity). The increased dye concentration absorbs a fraction of the UV light, creating less $OH^{\cdot}$ Radicals. Also, the intermediate compounds that form during the degradation process are increased and may consume some active radicals that are meant to react with the dye [6].

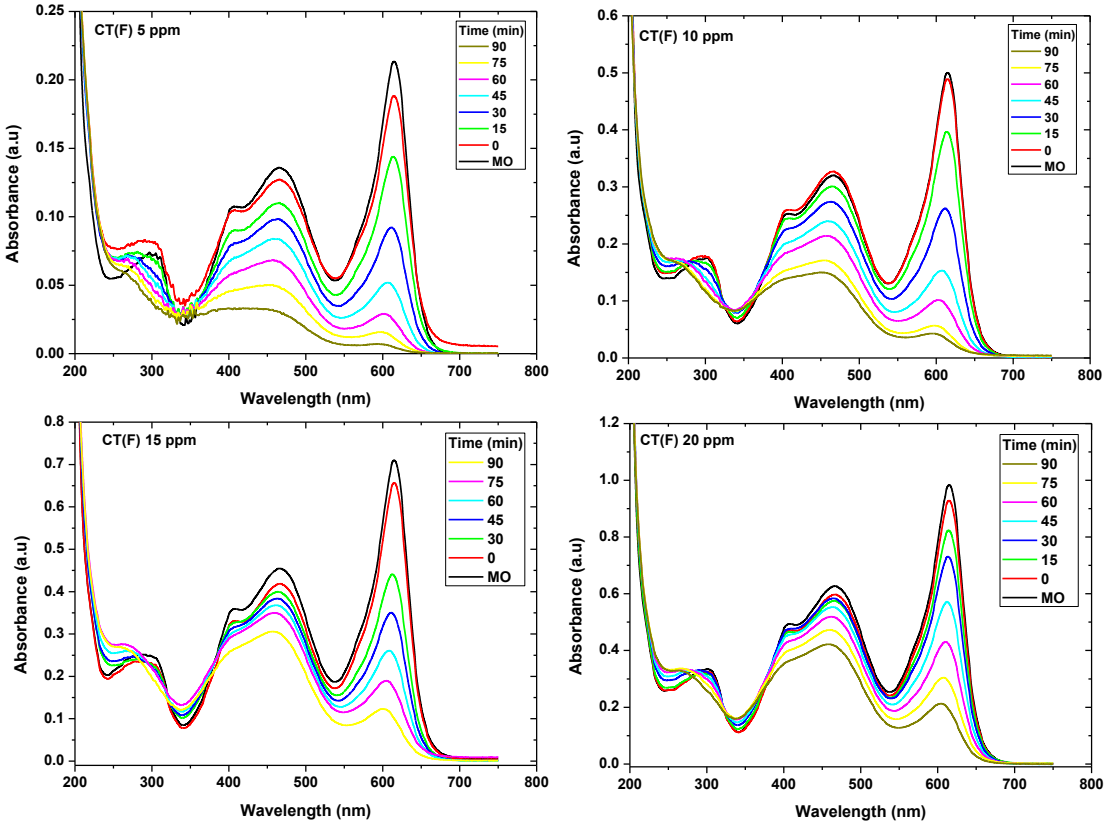

Figure 7.7: The UV-Vis spectra of CT(F) in 5 ppm - 20 ppm MO for 0 - 90 minutes irradiation.

A further decrease in degradation was observed when 20 ppm MO was used, achieving up to 78% degradation. Of course, a longer reaction time would eventually result in 100% degradation. The percentage of degradation decreases with an increasing dye concentration with a fixed amount of catalyst [10, 26]. As the dye concentration increased, there were more organics adsorbed on the surface of the TiO_2, reducing the number of photons available for the catalyst, reducing the hydroxyl radicals formed, hence decreasing the percent degradation [10]. Figure 7.9 shows the colour differences in the varying concentrations of MO irradiated for 90 minutes.

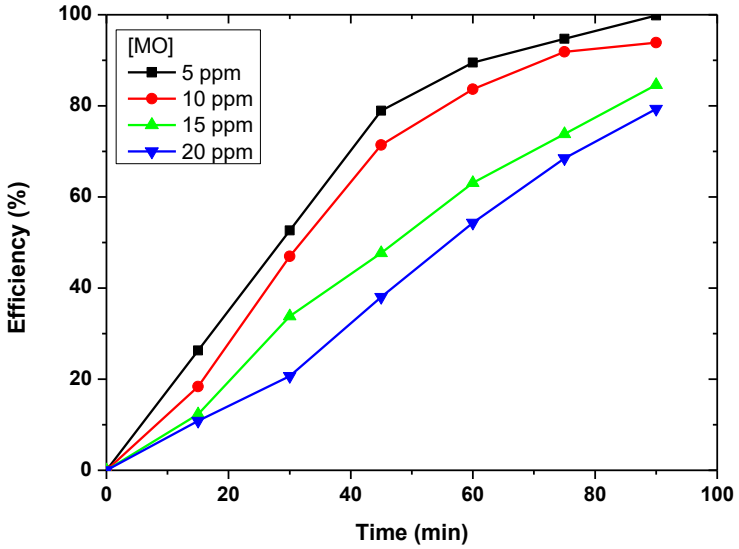

Figure 7.8: The % Efficiency of the CT(F) in 5 - 20 ppm MO for 90 minutes irradiation.

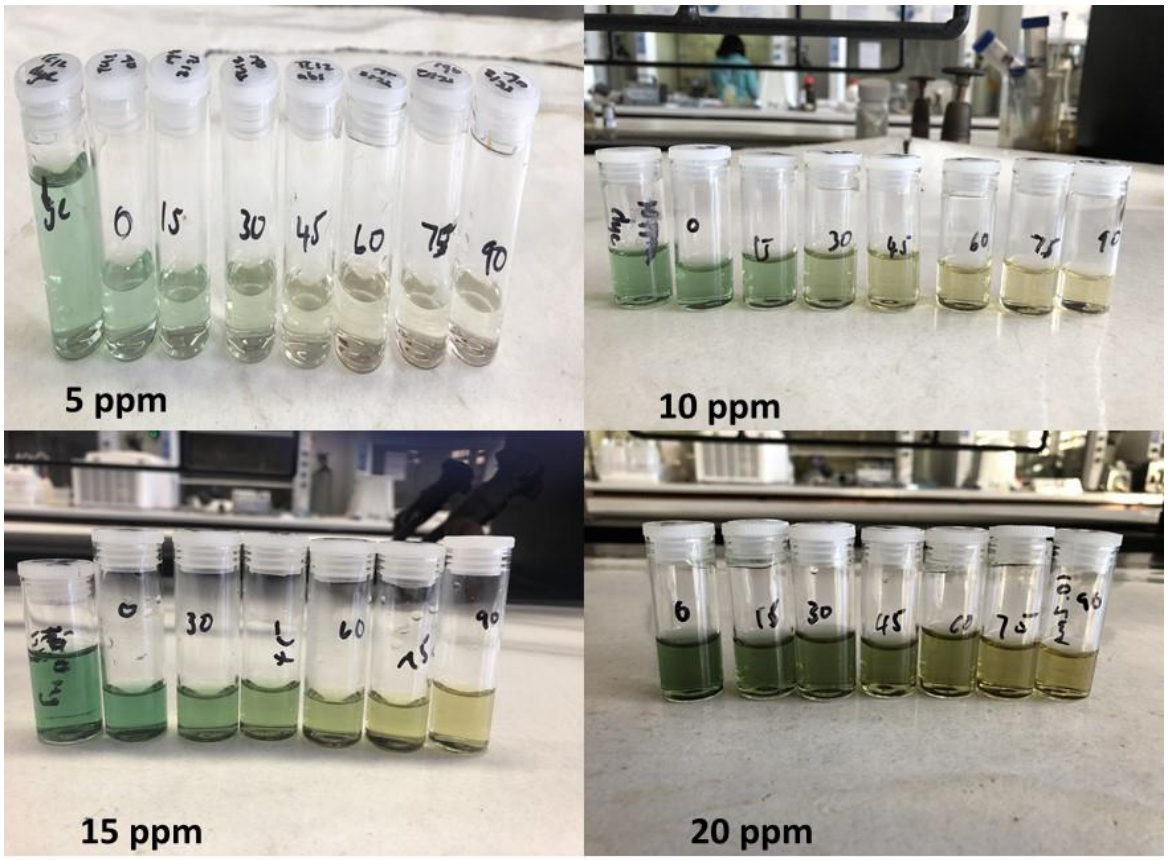

Figure 7.9: The associated colour change with degradation under irradiation for 0 - 90 minutes in 5 - 20 ppm MO along with associated dye before study.

7.3.4. Recyclability study

The reusability of a catalyst is of great importance in industrial processes, especially from an economics point of view. The catalyst CT(F) was placed through four cycles of degrading MO in 5 ppm concentration, shown in Figures 7.10. The recyclability study indicates that the composite does not perform as well with repeated catalytic reactions. The efficiency is reduced and is seen by a longer time to degrade the colour of the MO dye and the concentration. However, given the trend, if allowed sufficient time, the composite would degrade the MO to 100%. The attempts A, B and C do not differ much in their observed degradation efficiency potential. The third attempt at photocatalysis, Figure 7.10 recyclability B, had no effect until after 30 minutes; the concentration of the dye was reduced to the same level as attempts A and C. This may be explained by MO adhering to the surface of the catalyst and therefore reducing its catalytic efficiency. The degradation efficiency, Figure 7.11, shows the trend in degradation of MO. The first cycle achieved 100% degradation after 60 minutes, whereas cycles A, B, and C, after 90 minutes achieved 42%, 53% and 49% degradation, respectively. Figure 7.12 shows the colour degradation of the recyclability experiments.

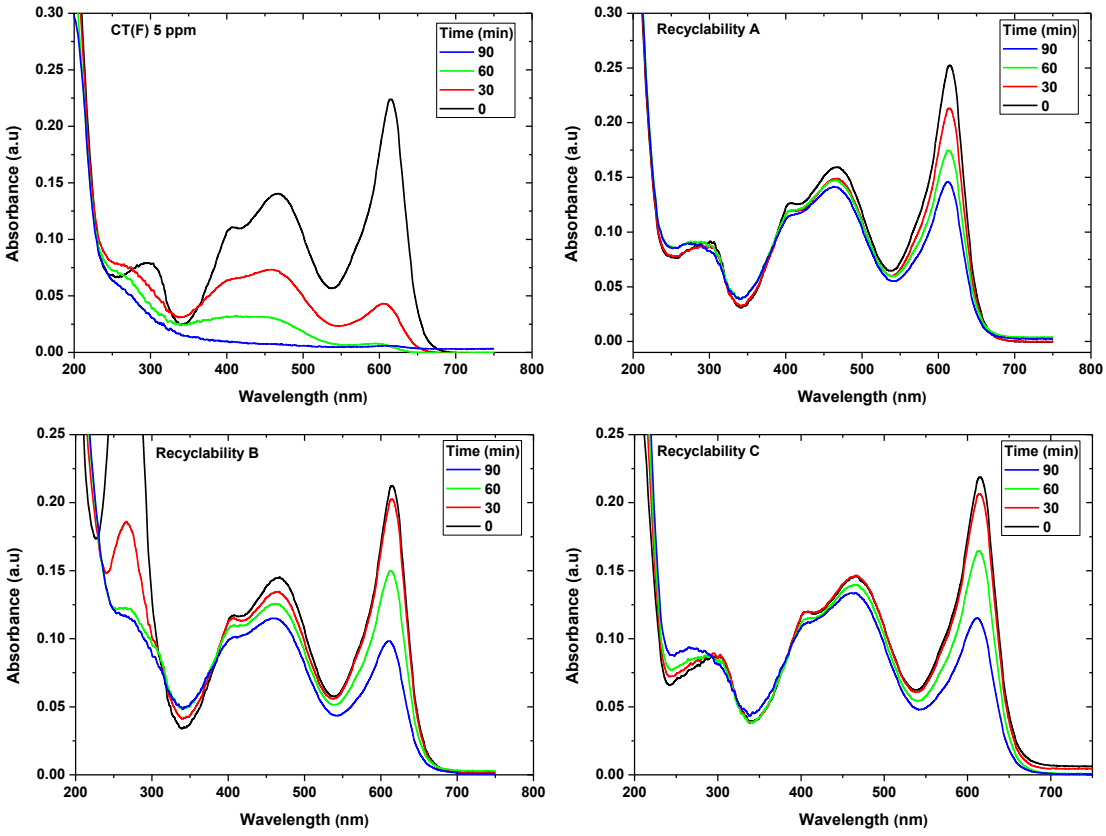

Figure 7.10: The UV-Vis of CT(F) and recycled CT(F) in 5 ppm MO for 0 - 90 minutes irradiation.

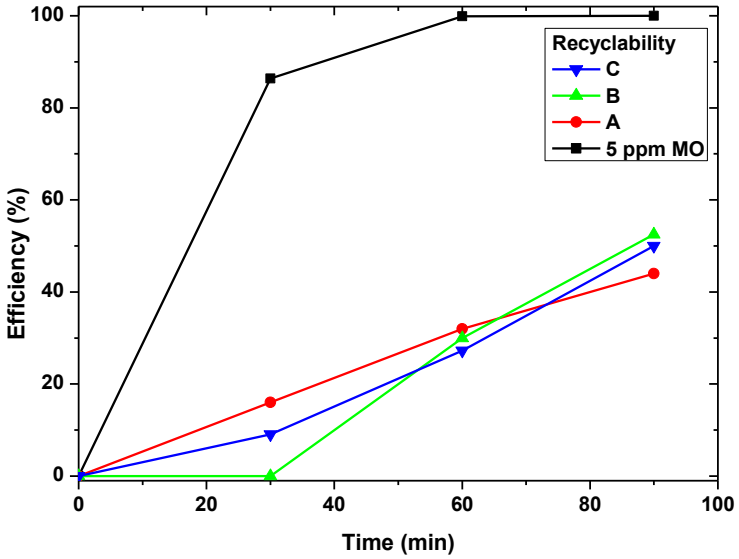

Figure 7.11: The efficiency of the recyclability of CT(F) in 5 ppm MO for 0 - 90 minutes irradiation.

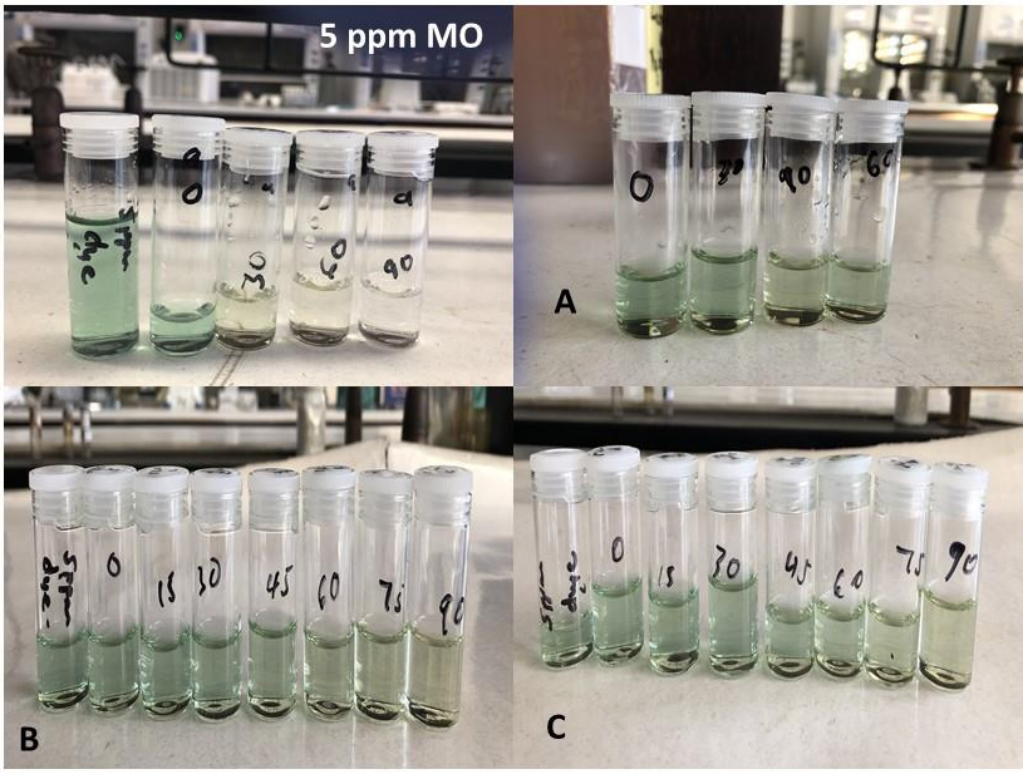

Figure 7.12: The colour of unexposed dye and aliquots of 5 ppm MO degraded over 0 - 90 minutes irradiation using CT(F) and recycled CT(F) in A-C.

7.3.5. Effect of pH on degradation of methyl orange

The effect of pH has multiple roles in photodegradation. The first is related to the ionisation:

$$TiOH + H^+ \rightarrow \mathrm{TiO}H^+ \qquad \text{Equation 7.5}$$

$$TiOH + OH^- \rightarrow TiO^- + H_2O \qquad \text{Equation 7.6}$$

as well as the reactant dye and its products. The pH can influence the adsorbance of dye molecules onto TiO_2 [1, 27]. Secondly, hydroxyl radicals form between hydroxide ions and positive holes, considered to be the major oxidation species at low pH while hydroxyl radicals are the predominant species at high or neutral pH [1]. In alkaline solutions, hydroxyl radicals are generated easily by oxidising more hydroxide ions that are available on the TiO_2 surface, enhancing efficiency [1, 28]. There is also coulombic repulsion in alkali solution between negative charged surfaces of TiO_2 and OH^+ ions, which might prevent ·OH radical formation and decrease photooxidation [1]. Thirdly, TiO_2 particles agglomerate in acidic conditions and the surface area for adsorption of dye is reduced. According to [1, 29], the azo dye degradation rate is increased with a decrease in pH as is the case here, shown in Figure 7.13. The decrease in pH increased the catalytic efficiency at pH 2 and pH 4 which degraded faster than higher pH values, pH 12 was the least efficient.

The mechanism of photocatalysis depends on the ability of the degraded compound to be adsorbed onto the surface of the catalyst, which is factor dependent. One of these factors is the charge of the degradation compound. The adsorption level of unmodified TiO_2 is higher for positively charged dyes than anionic negatively charged dyes [1, 30]. Because the charge depends on the pH of the solution, the nature of the dye and pH influence the degree of degradation or photocatalytic activity [1, 31-35]. From the results obtained, it seems that low pH is best for degradation of MO, where pH of 4 followed by pH 2 were the fastest to reach 100% efficiency in degrading MO (Figure 7.14). pH 4 reached 100% in 45 minutes whereas pH 2 reached total efficiency after 60 minutes. The only pH solution that did not reach complete efficiency after 90 minutes was pH 12. This could be due to too many hydroxyl groups present. Figure 7.15 shows the colour degradation of the different pH solutions, where pH 2 is pink due to the colour being affected by the acidic pH and the remaining solutions are green that degrade to colourless.

Varying the solution pH can affect the charge on the surface of the TiO_2 particles and shift the potential of the catalytic reaction. This alters the adsorption of the dye on the surface of the TiO_2 and changes the rate of reaction. TiO_2 is positively charged in acidic conditions and negatively charged in basic conditions [10]. TiO_2 has a higher oxidising activity at lower pH, but excess H^+ decreases the rate of reaction. The TiO_2 will behave as a strong Lewis acid because of the positive surface charge. The anionic dye acts as a strong Lewis base and adsorbs onto the catalyst surface, favouring the adsorption of dye in acidic conditions, whereas in basic conditions, this process is not favoured due to competitive adsorption by the hydroxyl groups and the dye molecule [10]. Also, Coulombic repulsion due to the negatively charged catalyst will hinder the adsorption [10, 36]. The extent of dye adsorption will depend on the initial concentration of the dye, the nature of the dye, the surface area of the photocatalyst and the pH of the solution which determines the surface charge of the photocatalyst. Adsorption is minimal when the pH of the solution is at the isoelectric point (point of zero charge). The surface of the photocatalyst is positively charged below the isoelectric point and negatively charged above it [10].

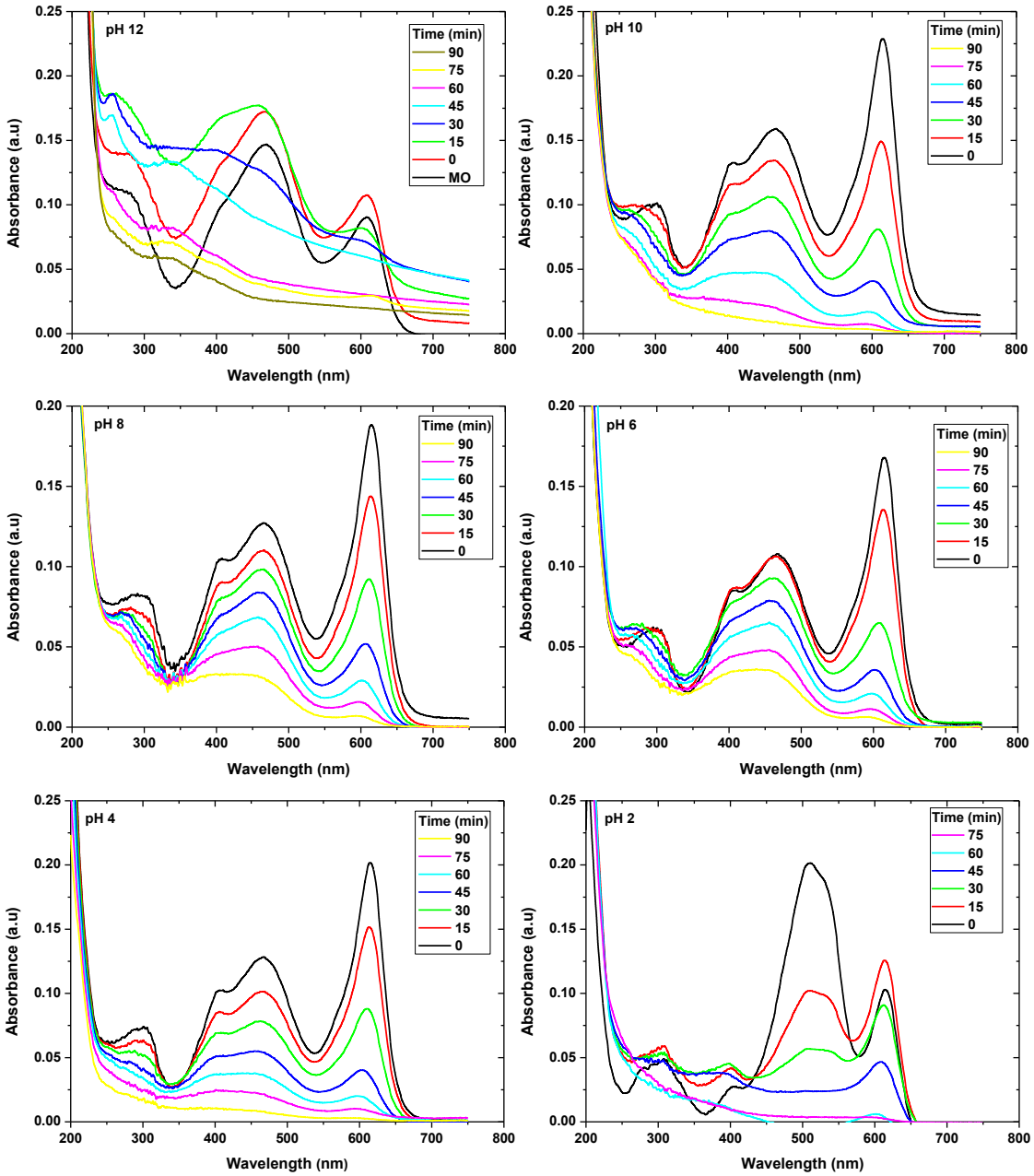

Figure 7.13: The UV-Vis spectra of CT(F) in 5 ppm MO at various pH values for 0 - 90 minutes irradiation.

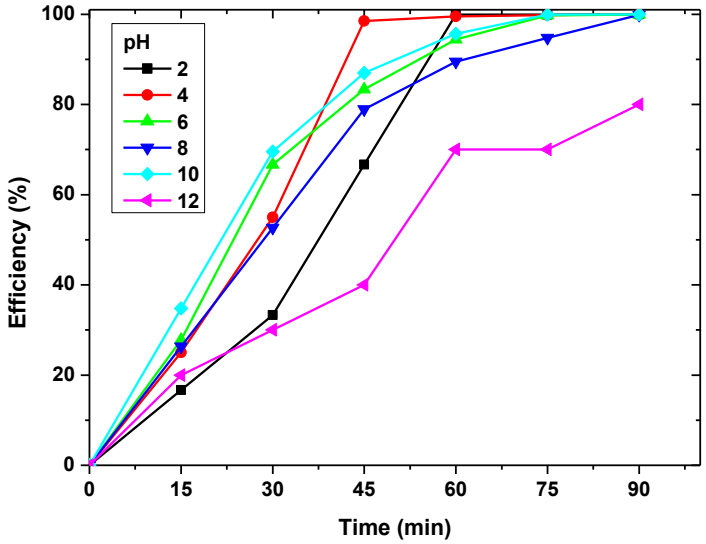

Figure 7.14: The catalytic efficiency of CT(F) in 5 ppm MO at different pH values for 0 - 90 minutes irradiation.

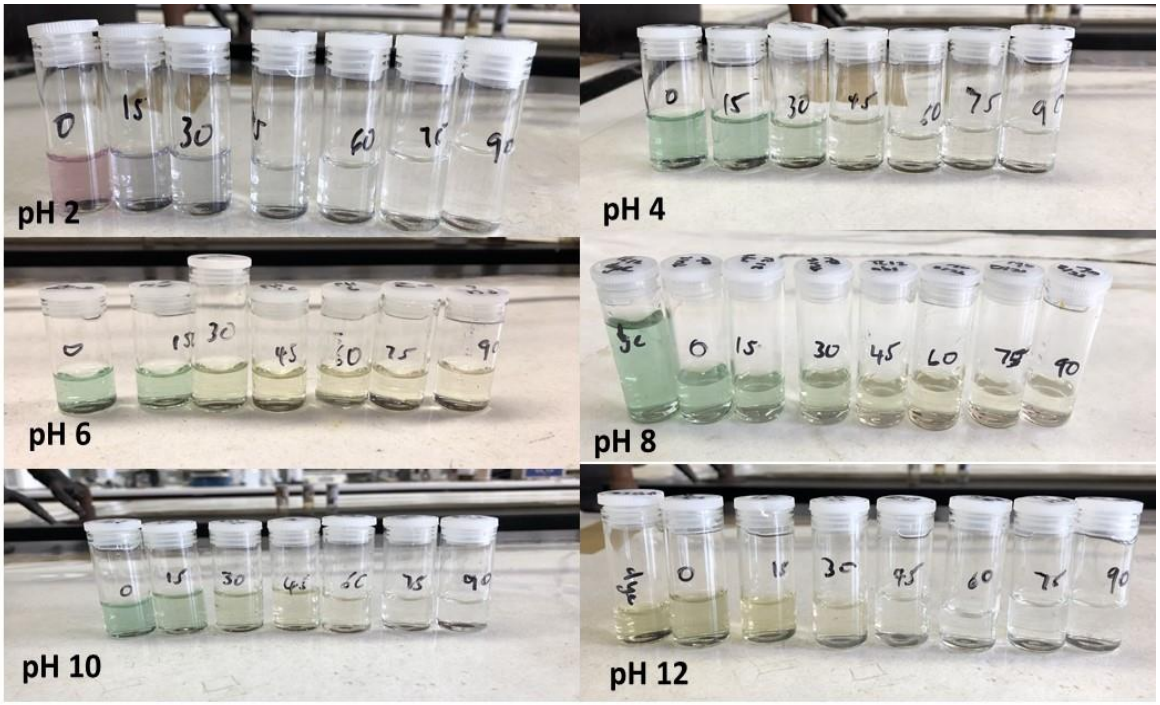

Figure 7.15: The colour of MO in different pH and photodegradation of MO for 0 - 90 minutes irradiation.

The catalysed photodegradation occurs by initiation reaction at a hydroxyl radical (˙OH). The radical source is either dissociation of water by light or photolysis, or oxidation of holes in the photocatalyst by water molecules or organic molecules [11]. The hole that originates from

bands with higher E_g are more effective on reacting with substrate molecules to produce OH radicals [11, 37]. The OH radicals then initiate the degradation of organic dye molecules.

$$H_2O + hv \rightarrow H^+ + OH^{\cdot} + \text{é} \qquad \text{Equation 7.7}$$

$$\frac{TiO_2}{Ti} + hv \rightarrow \frac{TiO_2}{Ti} + \text{é} + h^+ \qquad \text{equation 7.8}$$

$$h^+ + OH^- \rightarrow OH^{\cdot} \qquad \text{Equation 7.9}$$

This hydroxyl group then attacks the dye molecule to produce smaller organic compounds and mineral acids.

$$R + OH^{\cdot} \rightarrow R^{\cdot} + H_2O \qquad \text{Equation 7.10}$$

By following the reaction to photocatalytic degradation of the dye molecule,

$$OH^{\cdot} + dye \rightarrow products^* \qquad \text{Equation 7.11}$$

$$\frac{TiO_2}{Ti} + h^+ + dye \rightarrow \frac{TiO_2}{Ti} + \mathrm{CO_2} + \mathrm{H_2O} \qquad \text{Equation 7.12}$$

The products being CO_2, H_2O, mineral acid and non-toxic organic compounds [11]. The structure of the transient intermediates formed by photocatalysis are consistent with the degradation route, based on demethylation, methylation and hydroxylation [3]. Demethylation supersedes hydroxylation; however, hydroxylation creates the most intermediates in the system. Further oxidation opens the aromatic ring and completely mineralising the dye. The photocatalytic reaction also destroys the toxicity of the MO mother molecule [3]. The size and structure of the photocatalyst is important as well. Surface morphology will include the particle size and agglomerate size, since there is a direct relationship between organic compounds and surface coverage of the photocatalyst [10, 38]. The number of photons that strike the photocatalyst controls the rate of reaction which implies that the reaction only occurs on the absorbed phase of the photocatalyst. Surface area is another important factor to consider, although measurements were not performed in this study. The enlargement of surface area can be done by using very fine and small particles, which are either suspended in the solvent or made into a porous film [10]. Nanostructured materials with a crystallite grain size of < 20 nm are used because their properties are different compared to the larger particles. The larger surface area will contain more active sites compared to a low surface area.

The reaction temperature is also another important factor. An increase in reaction temperature increases the photocatalytic activity, but if the reaction temperature exceeds 80 °C, this promotes the recombination of charge carriers and does not favour the adsorption of dye on the surface of TiO_2 [10, 39]. Below 80 °C, adsorption is favoured, but at 0 °C increases the apparent activation energy [10, 40]. A temperature range between 20-80 °C is the ideal range for effective photo mineralisation of organic compounds [10, 41], which is in line with the room temperature that the experiments were conducted under. The rate of photodegradation also depends on the nature and concentration of the pollutant. A high concentration of dye will saturate the TiO_2 surface and reduce the efficacy of the catalyst as well as deactivate it. The chemical structure of the target compound will also influence the degradation rate [10]. Inorganic ions that may be in the wastewater, such as magnesium, iron, zinc, copper, phosphate, nitrate, sulphate and chloride can influence the photocatalytic rate of degradation since they can be adsorbed onto the surface of the TiO_2 [10, 42]. The inorganic anions such as nitrate, chlorides, carbonates and sulphates also inhibit the surface activity of the photocatalyst. The salt reduces the colloidal stability, increases mass transfer and reduces the surface contact between the pollutant and photocatalyst [10, 43]. These anions cause fouling as well as scavenge the hole and hydroxyl radicals [10, 44].

This fouling may be reduced by pre-treating the water with ion exchange resins. The light intensity and irradiation time also affect the degradation rate [10, 45]. Dye decolourisation increases initially as light intensity is increases. Photodegradation increases with irradiation time and is ideally highest at 3 hours for methyl orange [10]. Dissolved oxygen is an electron acceptor in photocatalysis and ensures that there are enough electron scavengers to trap the excited conduction band electrons from recombination [10, 46]. The oxygen does not affect the adsorption on the surface of the TiO_2 as reduction occurs at different location to oxidation. Dissolved oxygen is involved in the stabilisation of radical intermediates, mineralisation and direct photocatalytic reactions. Dissolved oxygen is also used in the cleavage of aromatic rings in organic pollutants present in water matrices [10, 47]. Photodegradation of organic dye increases with dissolved oxygen due to the formation of oxygen free radicals [10]. Because TiO_2 recombines electrons and holes very fast, and is also inactive in visible light, many techniques have been used to seal this gap and allow TiO_2 to absorb photons at lower energy levels. These methods include surface modification and semiconductor coupling and band gap modification. Dopants have also been used to improve response and reduce recombination. The dopant creates overlap of the conduction band in Ti (3d) with d levels of the transition metal,

this causes a red shift of the band edge of TiO_2, that allows light to be absorbed in the visible region [10].

7.4. Conclusion

The interaction between composite of maize tassel extracted cellulose and TiO_2 with pollutant dye during adsorption seems to be minimal, however on the addition of light, the photocatalytic reaction occurs. This reaction then degrades not only the colour of the dye but also the concentration and also performs better than plain TiO_2. The photocatalytic process depends on many parameters including the type and surface of TiO_2, pH, concentration of catalyst and dye and the chemical nature and structure of the dye. The best ratio of cellulose to TiO_2 was 5:95, giving the best degradation result of 100% in 90 minutes. This may be due to an interaction with the cellulose or due to a larger surface area for dye interaction. Also, from recyclability, dye concentration and pH studies, the composite was shown to be reusable with a slight reduction in catalytic activity. The best results came from the 5-ppm dye degradation process with CT(F) in pH 4 solution, due to the low concentration of dye which made for a quick loss in dye colour and concentration. The photocatalytic degradation of MO was favourable at low MO concentration (5 ppm) as the % removal decreased with an increase in dye concentration. The use of green organic/inorganic hybrids is progress in the production of green photocatalysts and green chemistry. The advantage here may be the easier removal of the photocatalyst form the treated solution, reducing treatment costs.

7.5. References

1. Akpan U. G., Hameed B. H., J Hazard. Mater., 2009, 170, 520-29.
2. Prado A. G. S., Bolzon L. B., Pedroso C. P., Moura A.O., Costa L. L., Appl. Catal. B: Environ., 2008, 82, 219-24.
3. Trabelsi H., Khadhraoui M., Hentati O., Ksibi M., Toxicol. Environ. Chem., 2013, 543-8.
4. Hao O. J., Kim H., Chiang P. C., Environ. Sci. Technol., 2000, 30, 449-502.
5. Slokar Y. M., Marechal A. M. L., Dyes Pigm., 1998, 37, 335-56.
6. Sleiman M., Vildozo D., Ferronato C., Chovelon J. M., Appl. Catal. B: Environ., 2007, 77, 1-11.
7. Konstantinou I. K., Albanis T. A., Appl. Catal. B: Environ., 2004, 49, 1-14.
8. Kuo W. G., Water Res., 1992, 26, 881-86.
9. Ince N. H., Gonenc D. T., Environ. Technol., 1997, 18, 179-83.
10. Kumar A., Pandey G., MSEIJ, 2017, 1, 3-7.
11. Fajriati I., Mudasir, Wahyuni E. T., IJACEBS, 2014, 1, 21-4.
12. Khatae A. R., Kasiri M. B., , J. Mol. Catal. A: chemical, 2010, 328, 8-26.
13. Daneshva N. R., Hejazi M. J., Rangarangy B., Khataee A. R., J. Environ. Sci. Health B, 2004, 39, 285-96.
14. Daneshvar N., Rasoulifard M. H., Hosseinzadeh F., Khataee A. R., J. Hazard. Mater. 2007, 143, 95-101.
15. Daneshvar N., Salari D., Khataee A. R., J. Photochem. Photobiol. A, 2003, 157, 111-16.
16. Daneshvar N., Salari D., Khataee A.R., J. Photochem. Photobiol. A, 2004, 162, 317-22.
17. Lachheb H., Puzenat E., Houas A., Ksibi M., Elaloui E., Guillard C., Herrmann J. M., Appl. Catal. B: Environmental, 2002, 39, 75-90.
18. https://www.chemicalbook.com/ChemicalProductProperty_EN_cb9687222.htm, 2019/07/05, 15:21.
19. Rahmawati F., Fadillah I., Mudjijono M., JMES, 2017, 8, 389-97.
20. Oliveira A. C. de M., dos Santos M. S., Brandao L. M. S., de Resende I. T., Leo I. M., Morillo E. S., Verga R. M. N., Fierro J. L. G., Egues S. M.da S., Figueiredo R. T., Int. J. Hydrogen Energ., 2017, 42, 28747-54.
21. Morawski A. W., Kusiak-Nejman, Przepiorski J., Kordala R., Pernak J., Cellulose, 2013, 20, 1293-300.
22. Mohamed M. A., Salleh W. N. W, Jaafar J., Ismail A. F., Mutalib M. A., Sani N. A. A., Asric S. E. A. M.., Ong C. S., Chem. Eng. J., 2016, 284, 202-15.
23. Chakrabarti S., Dutta B. K., J. Hazard. Mater. B, 2004,112, 269-78.

24. Huang M., Xu C., Wu Z., Huang Y., Lin J., Wu J., Dyes Pigm., 2008, 77, 327-34.
25. Yan M., Chen F., Zhang J., Anpo M., J. Phys. Chem. B, 2005, 109. 8673-78.
26. Diebold U., Surf. Sci. Rep. 2003, 48, 53-229.
27. Fox M. A., Dulay M. T., Heterogeneous photocatalysis, Chem. Rev. 1993, 93, 341-57.
28. Concalves M. S. T., Oliveira-Campos A. M. F., Pinto M. M. S., Plasencia P. M. S., Queiroz M.J.R.P., Chemosphere, 1991, 39, 781-6.
29. Sakthivel S., Neppolian B., Shankar M. V., Arabindoo B., Palanichamy M., Murugesan V., Sol. Energy Mater. Sol. Cells, 2003, 77, 65-82.
30. Baran W., Makowski A., Wardas W., Chemosphere, 2003, 53, 87-95.
31. Tang W. Z., An H., 1995, 31, 4158–70.
32. Tang W. Z., An H., Chemosphere, 1995, 31, 4171-83.
33. Alaton I. A., Balcioglu I. A., J. Photochem. Photobiol. A: Chem., 2001, 141, 247-54.
34. Poulios I., Aetopoulou I., Environ. Technol., 1999, 20, 479-87.
35. Poulios I., Avrans A., Rekliti E., Zouboulis A., J. Chem. Biotechnol., 2000, 75, 205-12.
36. Mansoori G. A., Bastami T. R., Ahmadpour A., Eshaghi Z., Annu. Rev. Nano Res., 2008, 2, 439-94
37. Valencia S., Marin J. M., dan Gloria Restrepo, Open Mater. Sci. J., 2010, 4, 9-14.
38. Cheng X.F., Leng W.H., Liu D.P., Zhang J.Q., Cao C.N., Chemosphere, 2007, 68 ,1976-84.
39. Zhai Y., Zhang S., Pang H., Mater. Lett., 2007, 61, 1863-66
40. Kanade K. G., Jin-Ook B., Mulik U. P., Amalnerkar D. P., Kale B. B., Mater. Res. Bull., 2006, 41, 2219-25.
41. Torres-Martinez C. L., Kho R., Mian O. I., Mehra R. K., J. Colloid Interface Sci., 2001, 240, 525-32.
42. Jung S., Kim S., Imaishi N., Cho Y., Appl. Catal. B, 2005, 55, 253-257.
43. Wang X., Yu J. C., Liu P., Wang X., Sua W., Fua X., J. Photochem. Photobiol. A, 2006, 179, 339–47.
44. Zheng M., Gu M., Jin Y., Jin G., Mater. Sci. Eng. B, 2000, 77, 55-9.
45. Brown M. A., De Vito S. C., Crit. Rev. Environ. Sci. Technol., 1993, 23, 249-324.
46. Jin H., Wu Q., Panga W., J. Hazard. Mater., 2007, 141, 123-28.
47. Hu C., Yu J. C., Hao Z., Wong P.K., Appl. Catal. B, 2003, 42, 47-55.

CHAPTER 8

Conclusions and recommendations

8.1. Conclusions

The research carried out in this dissertation concluded that cellulose extracted from maize tassel can be used as a support for the photocatalyst anatase TiO_2 in the degradation of methyl orange. The extraction of cellulose from maize tassel was carried out using 8 M NaOH with a pre-treatment of HNO_3 and NaOH. The time study did not have much effect on the extraction of cellulose, and it was concluded that prolonged alkali NaOH treatment destroyed the crystallinity and purity of cellulose. The production of TiO_2 by the sol-gel method gave pure anatase phase with spherical morphology and particle sizes of < 10 nm. The spherical nanoparticles were used in the formation of a nanocomposite with the maize tassel extracted cellulose. The composite showed agglomeration of TiO_2 on the fiber surface with improved thermal stability when compared to bare cellulose. The TiO_2 interaction with the cellulose fibers could be due to electrostatic interaction and covalent bonding. In the photocatalytic degradation of methyl orange, it was found that the best conditions for degradation are a pH 4 solution with 10 mg composite consisting of 5% cellulose and 95% TiO_2 in a methyl orange concentration of 5 ppm. The cellulose provides a scaffold on which the TiO_2 has more interaction with the dye due to greater exposure.

8.2. Recommendations

The research presented a method of using the left-over maize tassel, considered waste from maize plants. The cellulose from the maize tassel proved to be useful in the production of a nanocomposite with anatase TiO_2 nanoparticles. The interaction between the cellulose fibres and the photocatalyst TiO_2 should further be investigated in order to promote the use of the composite as well as maximise the TiO_2-cellulose interaction for the best MO degradation performance. The various methods of attachment and the control of particle size and catalyst agglomeration should also be studied further. The final degradation products could be characterised using high pressure liquid chromatography and mass spectrometry as decolorization doesn't always mean degradation to CO_2 and water.